

## Abstract

WASHINGTON, JOSEPH ST. PAUL. The Local Structure and Kinetics of Ge-Sb-Te Phase Change Materials for use in Solid State Applications. (Under the direction of Michael A. Paesler and Gerald Lucovsky.)

Recent interest in phase change materials (PCMs) for non-volatile memory applications has been fueled by the promise of scalability beyond the limit of conventional DRAM and NAND flash memory. Typical PCMs such as  $\text{Ge}_2\text{Sb}_2\text{Te}_5$  (GST) require significant nitrogen doping to shift their crystallization temperature ( $T_x$ ) sufficiently above standard CMOS device operation ranges ( $\sim 80^\circ\text{C}$ ) but also well below the melting point for thermal stability. Reactive ion etching (RIE) in an  $\text{Ar}/\text{Cl}_2/\text{CHF}_3$  plasma chemistry is another crucial step en-route to fabricating energy efficient, high density, nano-scaled PCM memory devices, yet it can lead to unfavorable, irreversible modification of the GST material. Chalcogens such as Te in GST can easily diffuse and interact unfavorably with the adjacent materials in the device structure thus negatively impacting the lifetime of a PCM device cell. In light of these implications for the final solid state device, it is necessary to understand and articulate the nature and structural implications of doping/alloying GST, the local structural changes that occur post etch processing, and the nature of the Ge-Sb binary and the Ge-Sb-Te ternary alloys.

Fourier Transform Infrared Spectroscopy (FTIR), X-ray photoelectron spectroscopy (XPS), X-ray absorption fine spectroscopy (XAFS), and *in-situ*, time resolved, X-ray diffraction (XRD) is used to understand the local structure of nitrogen in GST, and results

point to the formation of preferential Ge-N bonding in a chemically ordered germanium nitride local bonding environment in as-deposited and annealed films.

XAFS of various GeSb and Ge-Sb-Te glasses in the binary and ternary systems, in conjunction with time resolved XRD, show that Te in thin films of GeSb with gradually increasing Te atomic concentration prevents phase segregation, promotes stability, and induces nucleation. A multi-edge refinement of as-deposited thin films of  $\text{Ge}_2\text{Sb}_2\text{Te}_x$  ( $x=4, 5, 6, 7$ ), shows that Ge-Sb bonds are present in  $\text{Ge}_2\text{Sb}_2\text{Te}_4$  and  $\text{Ge}_2\text{Sb}_2\text{Te}_5$  from EXAFS fits, and these Ge-Sb bonds can also be isolated in the Ge near edge spectra in light of inelastic losses, i.e. shake-up / shake-off effects.

The chemical and structural effects of RIE on the crystallization of N-GST is examined via XPS, XAFS, time resolved laser reflectivity and XRD. Time resolved laser reflectivity and XRD show that exposure to various etch and ash chemistries significantly reduces the crystallization speed, while the transition temperature from the rocksalt to the hexagonal phase is increased. XPS and XAFS attribute this to the selective removal and oxidization of N, Ge, Sb, and Te, thus altering the local bonding environment to the detriment of device performance.

The Local Structure and Kinetics of Ge-Sb-Te Phase Change Materials  
for use in Solid State Applications

by  
Joseph St. Paul Washington

A dissertation submitted to the Graduate Faculty of  
North Carolina State University  
in partial fulfillment of the  
requirements for the Degree of  
Doctor of Philosophy

Physics

Raleigh, North Carolina

2010

APPROVED BY:

---

Eric A. Joseph

---

John E. Rowe

---

Nicholas C.M. Fuller

---

David E. Aspnes

---

Gerald Lucovsky  
Co-Chair of Advisory Committee

---

Michael A. Paesler  
Chair of Advisory Committee

## Dedication

I dedicate this work to my parents, Winston and Vivienne, and my older brothers, Sean, Jumbo, and Mark. My deepest desire is that we should experience true love, peace, joy, happiness, and fulfillment, which only comes from intimate relationship with God through belief in the redemption put in effect by His Son, Jesus Christ.

This milestone is testimony to the faithfulness of Our Father. In His love, He has never given me what I deserved, and so I hope to glorify Him with the rest of my life:

~ *Be still, know that I am God.* – Psalm 46: 11

~ *Not to us, O Lord, not to us, but to your name be the glory, for the sake of your love and faithfulness.* – Psalm 115: 1

~ *What have you, that you have not received? And if you received it, why are you proud, as if you did not receive it?* – 1 Corinthians 4: 7

~ *By the grace of God, you have been saved through faith. This has not come from you: it is God's gift. This was not a result of your works, so you are not to feel proud. What we are is God's work. He has created us in Christ Jesus for the good work he has prepared that we should devote ourselves to them.* – Ephesians 2: 8-10

## Biography

Joseph St. Paul Washington was born in St. Andrew, Jamaica on November 21<sup>st</sup>, 1983, to Winston and Vivienne Washington. After obtaining his high school diploma from St. George's College (Kingston, Jamaica), he accepted a full scholarship to attend Bethune-Cookman College (Daytona Beach, FL), where he enrolled in August 2001. Over the next 4 years, he grew, matured, and excelled, and finally celebrated graduation with Bachelor of Science (B.Sc.) degrees in Computer Science and Physics in May 2005. His imagination and fascination with computer hardware and solid state devices, and the attractive notion of being paid to go to school, led him enroll in the Physics graduate program at North Carolina State University (Raleigh, NC). Soon after passing the Doctor of Philosophy (Ph.D.) departmental qualifying exam, he was pursuing X-ray absorption spectroscopy studies of phase change materials and chalcogenides under the guidance of Michael Paesler. His early years under Michael's supervision were characterized by significant learning and appreciation of EXAFS and chalcogenides, made possible by numerous synchrotron based studies, and group meetings and classes with Gerald Lucovsky, Satish Agarwal, and Dave Baker. His later years built upon these foundations laid at NCSU, which saw Joseph grow exponentially as a spectroscopist and a materials scientist during two consecutive summer internships at IBM T.J. Watson Research labs (Yorktown Heights, NY), under the direct supervision of Eric Joseph, and the mentorship of Nicholas Fuller. These years of learning and growth at both NCSU and IBM culminated in Joseph becoming a true research scientist and obtaining a Ph.D. in Physics. His past experiences up to this point, stands as constant reminder of *God's*

*undeniable faithfulness*, and so the future although unknown, is actually already a cause for celebration in the present.

## Acknowledgements

I am thankful to the innumerable faculty, friends, and family who have supported, loved, cared for, prayed for, taught, mentored, coached, encouraged, nourished and sheltered me from the very beginning in Daytona Beach, FL, right up to this point, in Raleigh, NC. You have all positively influenced everything about me, from my acquired southern vernacular to my worldview and theology. I am positively indebted to you all!

I am very grateful to my advisor, Michael Paesler, for taking a gamble in recruiting a young, innocent, wide-eyed, naive Jamaican and subsequently advising, encouraging, and nurturing him into a Physicist. I will always be able to rely on Michael for support, and will forever treasure our true friendship. It was a tremendous honor to have worked with Gerald “Gerry” Lucovsky, who has constantly urged us to become “true spectroscopists”. I am forever grateful to both Gerry and Michael for their guidance and support as chair and co-chair of my committee, and I similarly acknowledge the remaining NCSU based advisory committee for their helpful advice and corrections: Dave Aspnes and Jack Rowe. Dave is a wonderful professor whose E&M class I truly enjoyed, and a brilliant optical spectroscopist: he has taught me so much about Ellipsometry and optical methods of characterization. Jack has always been my advocate and is a big source of support (matched by his big heart). My committee members based at IBM T.J. Watson Research Labs, Nicholas Fuller, and Eric Joseph, have both been true incarnations of mentorship. They have typified kindness, encouragement, honesty, and wise counsel. During the course of this dissertation, they were always available to talk: we literally shared hundreds of meaningful phone calls, text

messages, and emails. We also shared great meals and great memories from my internships and research projects at IBM, including summer corporate league football, and fun times exploring Long Island, NY. My manager during my internship at IBM, Ying Zhang, and a host of other ‘IBMer’s who have befriended me and collaborated with me, notably Simone Raoux and Jean Jordan-Sweet, cannot be thanked enough for their help in making this dissertation possible.

Without the kind assistance of the beamline scientists at MRCAT (APS) and X23A2 (NSLS), such as Bruce Ravel and Carlo Segre, this dissertation would have a lot less data and very little quality measurements. The many long hours at the MRCAT beamline, at the Advanced Photon Source, would not have been possible without the hands on collaboration of Dave Baker and Leonardo Miotti. The many joyful days researching at NCSU would not have been joyful at all, without the kind love and gracious support of Rebecca Savage; I am convinced she has all the character traits of that woman in Proverbs 31. And, I cannot ever repay the kindness of Chastity Buehring or Ina Lunney, who have never failed to deliver a kind word, delicious snacks, and gracious assistance to anyone who came knocking.

# Table of Contents

<b>List of Tables</b> .....	<b>x</b>
<b>List of Figures</b> .....	<b>xii</b>
<b>Chapter 1 Introduction</b> .....	<b>1</b>
1.1 The Structural Implications of Nitrogen doping in GST .....	3
1.2 The Structural Implications of Reactive Ion Etching N-GST.....	5
1.3 The local structure of GeSb & the role of Te in the Ternary System .....	6
1.4 Outline of the rest of this Dissertation .....	8
<b>Chapter 2 The Structural Implications of Nitrogen doping in GST</b> .....	<b>10</b>
2.1 Amorphous N-GST ATR-FTIR Measurements.....	11
2.2 Amorphous N-GST ATR-FTIR Results and Analysis .....	13
2.3 Amorphous N-GST Depth Profile XPS.....	15
2.4 The EXAFS Equation .....	17
2.5 Amorphous N-GST XAFS Analysis.....	21
2.5.1 Near Edge Analysis.....	23
2.5.2 EXAFS Analysis.....	28
2.5.3 EXAFS Models and Fitting .....	33
2.6 <i>In-situ</i> Time Resolved XRD of N-GST .....	40
2.7 XAFS of 5%N-GST versus Anneal Condition .....	43
2.8 Crystallization of 5%N-GST in XRD vs EXAFS.....	47

2.8.1	EXAFS Data Analysis and Fitting.....	49
2.8.2	The Nature of Crystalline N-GST.....	55
<b>Chapter 3</b>	<b>Phase Segregation in binary <math>\text{Ge}_x\text{Sb}_{(1-x)}</math>.....</b>	<b>59</b>
3.1	$\text{Ge}_x\text{Sb}_{(1-x)}$ EXAFS studies.....	60
3.1.1	$\text{Ge}_x\text{Sb}_{(1-x)}$ EXAFS Fits and Modeling.....	65
3.1.2	EXAFS vs XRD in annealed 15:85 .....	71
3.2	EXAFS of as-deposited $(\text{Ge}_{15}\text{Sb}_{85})_x\text{Te}_{(1-x)}$ & $(\text{Ge}_{50}\text{Sb}_{50})_x\text{Te}_{(1-x)}$ .....	75
3.2.1	EXAFS of the amorphous 15:85+Te & 50:50+Te.....	76
3.3	EXAFS vs XRD of annealed $(\text{Ge}_{15}\text{Sb}_{85})_x\text{Te}_{(1-x)}$ & $(\text{Ge}_{50}\text{Sb}_{50})_x\text{Te}_{(1-x)}$ .....	83
3.3.1	EXAFS vs XRD of annealed 15:85+Te.....	83
3.3.2	EXAFS vs XRD of annealed 50:50+Te.....	89
3.4	EXAFS of as-deposited $\text{Ge}_2\text{Sb}_2\text{Te}_x$ .....	93
3.4.1	EXAFS analysis of as-deposited $\text{Ge}_2\text{Sb}_2\text{Te}_x$ ( $x=4,5,6,7$ ) .....	95
<b>Chapter 4</b>	<b>Conclusions.....</b>	<b>103</b>
	<b>References.....</b>	<b>107</b>
	<b>Appendices.....</b>	<b>120</b>
	Appendix 1 - An Introduction to EXAFS Theory .....	121
	Appendix 2 - Experimental Details.....	126
	Appendix 3 – (JAP in preparation) Characterizing the Effects of Etch-Induced Material Modification on the Crystallization Properties of Nitrogen Doped $\text{Ge}_2\text{Sb}_2\text{Te}_5$ .....	130

Appendix 4: (JNCS Submitted) Analysis of the forgotten parts of the Ge K edge spectra: life beyond the EXAFS oscillations! .....	138
Appendix 5: Ge and Sb K edge EXAFS Fit Results calculated for the 400°C annealed Ge <sub>x</sub> Sb <sub>(1-x)</sub> samples. ....	146
Appendix 6: The Optical Dielectric Function for as-deposited N-GST alloys.....	149

## List of Tables

Table 2-1: Calculated penetration depth ( $d_p$ ), and the estimated final depth after passing through a 100nm and 1000nm thick sample, for the spectral range observed.....	12
Table 2-2. Summary of Programs used for XAFS Analysis.....	22
Table 2-3: Final fitting statistical parameters for N-GST samples showing the Fourier transform ranges ( $\Delta k$ ), fitting ranges ( $\Delta R$ ), the R factor for each data set ( $R$ ). The MDS results shown: the number of independent parameters used in the fits ( $N_{ind}$ ), the number of variables ( $N_{var}$ ), the chi-squared ( $\chi^2$ ), the reduced chi-squared ( $\chi^2_v$ ), the R factor, and the measurement uncertainty in R ( $\epsilon$ ). .....	37
Table 2-4: A summary of the fitting parameters calculated from the fits to the amorphous N-GST samples and their percent errors (the fitting results of undoped GST is shown and discussed in chapter 4). In total, 16 parameters are determined from the three data sets. $S_0^2$ was 0.8 for all data sets.....	37
Table 2-5: Background removal quantities used in AUTOBK for Ge K edge N-GST crystallized samples. The $E_0$ values is not shown since all samples were aligned to a common $E_0$ of $\sim 11097\text{eV}$ . .....	43
Table 2-6: Final fitting statistical parameters for 250C_RAMP and 250C_10MIN showing the Fourier transform ranges ( $\Delta k$ ), fitting ranges ( $\Delta R$ ), the R factor for each data set ( $R$ ). The MDS results shown: the number of independent parameters used in the fits ( $N_{ind}$ ), the number of variables ( $N_{var}$ ), the chi-squared ( $\chi^2$ ), the reduced chi-squared ( $\chi^2_v$ ), the R factor, and the measurement uncertainty in R ( $\epsilon$ ). .....	50
Table 2-7: A summary of the fitting parameters calculated from the fits to the 250C_RAMP and 250C_10MIN samples and their percent errors. In total, 22 parameters are determined from the two data sets. $S_0^2$ was 0.8 for all data sets. ....	52
Table 2-8: Background removal quantities used in AUTOBK for Ge K edge N-GST crystallized samples. The $E_0$ values are not shown since all samples were aligned to a common $E_0$ of $\sim 11103\text{eV}$ . The FCC_0.0% sample was capped with a thin layer of Nb to prevent surface oxidation, so we increased Rbkg to remove to low R background signal. We were unable to collect similar range of data for FCC_6.1% due to beamline power outage.....	55
Table 3-1: Final fitting statistical parameters for Ge and Sb K edges for amorphous 15:85 and 50:50 showing the Fourier transform ranges ( $\Delta k$ ), fitting ranges ( $\Delta R$ ), the R factor for each data set ( $R$ ), the number of independent parameters used in the fits ( $N_{ind}$ ), the number of variables ( $N_{var}$ ), the chi-squared ( $\chi^2$ ), the reduced chi-squared ( $\chi^2_v$ ), the R factor, and the measurement uncertainty in R ( $\epsilon$ ). .....	66
Table 3-2: A summary of the fitting parameters calculated from the fits to the amorphous $\text{Ge}_x\text{Sb}_{(1-x)}$ samples and their percent errors. Each alloy shows both the parameters from the Ge edge as well as the Sb edge. In total, 71 parameters are determined from the 10 data sets (5 samples, 2 edges). $S_0^2$ was 0.8 for all Ge edge data and 0.9 for all Sb edge data. ....	69

Table 3-3: Final fitting statistical parameters for Ge and Sb K edges for a-15:85+Te and 50:50+Te showing the Fourier transform ranges ( $\Delta k$ ), fitting ranges ( $\Delta R$ ), the R factor for each data set (R), the number of independent parameters used in the fits ( $N_{ind}$ ), the number of variables ( $N_{var}$ ), the chi-squared ( $\chi^2$ ), the reduced chi-squared ( $\chi^2_v$ ), the R factor, and the measurement uncertainty in R ( $\epsilon$ ). 15:85+Te samples were fit together in a MDS, as were 50:50+Te, and shared parameters are shown in parentheses () and brackets [].....	79
Table 3-4: A summary of the fitting parameters calculated from the fits to the amorphous 15:85+Te and 50:50+Te samples and their uncertainties. In 15:85+Te, 16 parameters are determined from the 2 data sets while in 50:50+Te, 20 parameters were calculated from 3 data sets. $S_0^2$ was 0.8 for all data sets. ....	79
Table 3-5: Background removal quantities used in AUTOBK for Ge, Sb, and Te K edges in $Ge_2Sb_2Te_x$ samples. ....	95
Table 3-6: Final fitting statistical parameters for Ge, Sb and Te K edges for amorphous 225 showing the Fourier transform ranges ( $\Delta k$ ), fitting ranges ( $\Delta R$ ), the R factor for each data set (R), the number of independent parameters used in the fits ( $N_{ind}$ ), the number of variables ( $N_{var}$ ), the chi-squared ( $\chi^2$ ), the reduced chi-squared ( $\chi^2_v$ ), the R factor, and the measurement uncertainty in R ( $\epsilon$ ). ....	96
Table 3-7: A summary of the fitting parameters calculated from the fits to the amorphous $Ge_2Sb_2Te_x$ samples and their uncertainties. $S_0^2$ was 0.85 for all Sb and Te edge data, and 0.7 for Ge edges. ....	98
TAB. 8: Fitting results for partially etched amorphous GST.....	135

## List of Figures

- Figure 2-1: FTIR spectra showing % Absorbance vs wavenumber for N-GST samples and a bare Si wafer. The titles in B, C, and D refer to the film thickness (nm) and N flow rate (sccm.) used for deposition. The fine dashed lines are fits to the spectra, with the fitting range indicated by vertical dashed lines. .... 14
- Figure 2-2: Comparison of depth profiled XPS Ge 2p<sub>3/2</sub> binding energy spectra for A) 5%N-GST and B) GST. The 5%N-GST spectra represents a depth of ~34nm versus ~17nm for the GST sample. The dashed line in both spectra shows the binding energy of the final depth profile..... 16
- Figure 2-3: A comparison of the un-normalized and normalized Ge K edge absorption data for 5%N-GST. The solid black line was 1000nm thick film on glass substrate, measured at the APS, MRCAT beamline ID-10, using Ar / N mixture in the ionization chamber. The gray dashed line was 100nm film on a bare Si wafer, measured at the NSLS, NIST X23A2 beamline. On either occasion, fill gases of different ratios of Ar / N were used in the ionization chamber..... 24
- Figure 2-4 : Normalized Ge near edge comparison of as deposited 6.1%N-GST (black dotted line), 5%N-GST (black dashed line), 2.5%N-GST (gray solid line), and GST (black solid line). The feature that is scaling with nitrogen concentration is indicated just past the white line..... 25
- Figure 2-5: (A) Near Edge Spectra of beta-Ge<sub>3</sub>N<sub>4</sub> (arrow indicates the main identifying feature for these) and (B) Fourier transformed EXAFS spectra for beta-Ge<sub>3</sub>N<sub>4</sub> (Republished from [62]). .... 26
- Figure 2-6: (A) Near Edge Spectra of a-GeN and (B) Magnitude of Fourier transformed EXAFS spectra of a-GeN. The  $\chi(k)$  data used for the Fourier transform, used a data range,  $\Delta k = 3 - 13 \text{ \AA}^{-1}$ , and followed our typical background removal procedures..... 27
- Figure 2-7: Athena screen shot showing background removal parameters (used in AUTOBK) for N-GST samples. The k range is the range over which a spline using  $N_{\text{knots}}$  knots was optimized to approximate the background function. E0 is typically set to the maximum of first derivative of  $\mu(E)$  and can be used to align multiple data sets. K-wieght also us to further tune to frequencies to be minimized below Rbkg. Pre-edge and normalization range specifies the range used to define the pre-edge and post-edge lines. Spline range defines the range over with AUTOBK minimizes the background. .... 29
- Figure 2-8:  $x(k)$  extracted from the  $\mu(E)$  of as-deposited 6.1%N-GST (black dotted line), 5%N-GST (black dashed line), 2.5%N-GST (gray solid line), and GST (black solid line), using the AUTOBK program. Each spectrum is the average of at least four florescence measurements. Each  $x(k)$  function is multiplied by  $k^2$  to emphasize the high-energy oscillations, as shown on the y-axis..... 29
- Figure 2-9: Magnitude of Fourier transformed EXAFS spectra of 6.1%N-GST (black dotted line), 5%N-GST (black dashed line), 2.5%N-GST (gray solid line), and GST (black

solid line), using a window range of $\Delta k = 3-13.5 \text{ \AA}^{-1}$ . The gray line shows the background feature.....	30
Figure 2-10: (A-D): Fits to the Ge K edge as-deposited N-GST data for A) GST, B) 2.5%N-GST, C) 5%N-GST, and D) 6.1%N-GST. Magnitude of the complex Fourier transformed of EXAFS spectra is shown. The solid black line is the data, and gray dash line is the fits.....	38
Figure 2-11: Intensity of diffracted x-ray peaks is plotted vs diffraction angle ( $2\theta$ ) over a range of $15^\circ$ (vertical axis) vs temperature (horizontal axis) for blanket films of GST and 5%N-GST heated at a rate of $1^\circ\text{C/s}$ . This is shown alongside the Intensity vs ( $2\theta$ ) which was taken at $450^\circ\text{C}$ . Transitions to the crystalline rocksalt phase are marked by vertical solid gray lines, corresponding to $175^\circ\text{C}$ , $215^\circ\text{C}$ , $250^\circ\text{C}$ , and $250^\circ\text{C}$ for 0%, 2.5%, 5%, and 6.1%N-GST, respectively. The cubic peak indices are shown.....	42
Figure 2-12: Normalized Ge near edge comparison of AS_DEP (black dotted line), 250C_RAMP (black dashed line), 250C_10MIN (gray solid line), and 300C_30MIN (black solid line). Arrows indicate the appearance of sharp features relating the long range order in GST.....	44
Figure 2-13: $x(k)$ extracted from the $\mu(E)$ of AS_DEP (black dotted line), 250C_RAMP (black dashed line), 250C_10MIN (gray solid line), and 300C_30MIN (black solid line), using the AUTOBK program. Each spectrum is the average of at least four fluorescence measurements.....	44
Figure 2-14: Magnitude of Fourier transformed EXAFS spectra AS_DEP (black dotted line), 250C_RAMP (black dashed line), 250C_10MIN (gray solid line), and 300C_30MIN (black solid line), using $\Delta k = 3-15\text{ \AA}$ .....	45
Figure 2-15: The steady state nucleation rate [97] of GST as a function of time, reaches a maximum at about $250^\circ\text{C}$ . The dashed line corresponds to the amorphous to FCC crystalline transition temperature for GST sample as observed in <i>in-situ</i> XRD in figure 2-11. (Republished from [98] © JAP 2004).....	48
Figure 2-16: Fits to the Ge K edge for (A) 250C_RAMP and (B) 250C_10MIN. Magnitude of the complex Fourier transformed of EXAFS spectra is shown. Solid black line = data, gray dashed line = fit.....	51
Figure 2-17: Normalized Ge near edge comparison of FCC_0.0% (solid black line), FCC_2.5% (gray dashed line), FCC_5.0% (black dashed line), FCC_6.1% (black dotted line). The solid black arrow indicates sharp features relating the long range order in GST, while dashed arrow at the near edge indicates the region increasing with N at %.	56
Figure 2-18: Magnitude of the complex Fourier transformed EXAFS spectra of FCC_0.0% (solid black line), FCC_2.5% (gray dashed line), FCC_5.0% (black dashed line), FCC_6.1% (black dotted line) their respective using $\Delta k$ values shown in table 2-5. The Ge-N $1^{\text{st}}$ shell is clearly distinguishable between $1 - 2\text{ \AA}$ . The box between $2 - 3.5 \text{ \AA}$ is crystalline GST first shell, where there is variation between the samples. The box between $5 - 7.5 \text{ \AA}$ is the location of FCC GST multiple scattering contributions. The only variation between samples in this region is a drop in amplitude as N at % increase.....	57

Figure 3-1: Comparison of the magnitude of the complex FT of the Ge K edge EXAFS for as deposited (top) and the 400°C annealed (bottom) 75:25 (solid black line), 50:50 (dash gray line), 25:75 (solid gray line), 15:85 (black dashed line), 7:93 (black dotted line), and Ge metal foil (gray dotted line). Background removal quantities used in AUTOBK for both amorphous and annealed $\text{Ge}_x\text{Sb}_{(1-x)}$ samples are shown in the inset. The $E_0$ values are not shown since all samples were aligned to a common $E_0$ of ~11102eV for Ge analysis. ....	61
Figure 3-2: Comparison of the magnitude of the complex FT of the Sb K edge EXAFS for as deposited (top) and the 400°C annealed (bottom) 50:50 (dash gray line), 25:75 (solid gray line), 15:85 (black dashed line), 7:93 (black dotted line), and Sb metal foil (gray dotted line). Background removal quantities used in AUTOBK for both amorphous and annealed $\text{Ge}_x\text{Sb}_{(1-x)}$ Sb edges are shown in the inset. The $E_0$ values are not shown since all samples were aligned to a common $E_0$ of ~30491eV for Sb analysis. ....	62
Figure 3-3: Basic structural models for tetrahedrally bonded Ge and trigonal pyramidal coordinated Sb. ....	65
Figure 3-4: Fits to the Ge and Sb K edge for 15:85 (top) and 50:50 (bottom). Magnitude of the complex Fourier transformed of EXAFS spectra is shown. Solid black line = data, gray dashed line = fit. These fits are representative of the typically good fit to data obtained in all amorphous and annealed $\text{Ge}_x\text{Sb}_{(1-x)}$ . ....	68
Figure 3-5: Ge-Sb bonding fraction calculated from the Ge edge (black line), versus the Sb-Ge bond fraction calculated at the Sb edge (gray line) of the $\text{Ge}_x\text{Sb}_{(1-x)}$ . We can compare the fraction of Ge atoms bonded to Sb (as opposed to Ge-Ge bonds) and the fraction of Sb environment bonded to Ge (as opposed to Sb-Sb). ....	70
Figure 3-6: <i>In situ</i> XRD of 15:85 film during a 1°C/min ramp anneal in He. At crystallization, Bragg peaks of Sb with Ge in solid solution are seen. Ge (111) peak appears at 375°C (from ref [114]). ....	71
Figure 3-7: Comparison of the magnitude of the complex Fourier transform of the EXAFS data at the Ge K edge 15:85 as deposited (black dash line), after a 300°C ramp/quench (gray solid line), and after a 400°C 30 minute anneal (solid black line). ....	72
Figure 3-8: Fits to the Ge K edge for 15:85 after a 300°C ramp/quench. Magnitude of the complex Fourier transformed of EXAFS spectra is shown. Solid black line = data, gray dashed line = fit. For convenience, we show the calculated fit variables and the statistical goodness- of- fit parameters in the figure. ....	74
Figure 3-9: Comparison of the magnitude of the complex Fourier transform of the Ge K edge EXAFS for the as deposited (A) 15:85+Te and (B) 50:50+Te, for samples with no Te (solid black line), 10% Te (solid gray line), 20% Te (black dashed line), and 33% Te (gray dashed line). ....	77
Figure 3-10: Fits to the Ge K edge for 15:85 +10 (20) and 50:50+10 (20, 33) samples. Magnitude of the complex Fourier transformed of EXAFS spectra is shown. Solid black line = data, gray dashed line = fit. ....	80

Figure 3-11: Change in bonding fraction of Ge-Ge (black dashed line), Ge-Sb (gray dashed line), and Ge-Te (gray solid line) at the Ge K edge in 15:85 and 50:50 with increasing Te content.....	82
Figure 3-12: Intensity of diffracted x-ray peaks is plotted vs diffraction angle ( $2\theta$ ) over a range of $15^\circ$ (vertical axis) vs temperature (horizontal axis) for blanket films of 15:85+10 and 15:85+20 heated at a rate of $1^\circ\text{C/s}$ . This is shown alongside the Intensity vs ( $2\theta$ ) which was taken at $450^\circ\text{C}$ . Transitions due to the crystalline Sb rhombohedral phase are marked by vertical solid gray lines. The black dotted arrows show un-indexed features. The Sb rhombohedral peak indices are indicated.....	84
Figure 3-13: Normalized Ge near edge comparison of $300^\circ\text{C}$ annealed 15:85 (solid black line), 15:58+10 (solid gray line), and 15:85+20 (black dashed line). The intensity of the white line, and the appearance of sharper near edge features coincide with Te addition.....	86
Figure 3-14: Comparison of the magnitude of the complex Fourier transform of the Ge K edge EXAFS for $300^\circ\text{C}$ annealed 15:85 (solid black line), 15:58+10 (solid gray line), and 15:85+20 (black dashed line). The arrows show the appearance of long range order in 15:85+20.....	86
Figure 3-15: Intensity of diffracted x-ray peaks is plotted vs diffraction angle ( $2\theta$ ) over a range of $15^\circ$ (vertical axis) vs temperature (horizontal axis) for blanket films of 50:50+10, 50:50+20, and 50:50+33, heated at a rate of $1^\circ\text{C/s}$ . This is shown alongside the intensity vs ( $2\theta$ ) which was taken at room temperature after a ramp to $450^\circ\text{C}$ . The Sb and Ge crystal peak indices are indicated, as well as the NaCl cubic phase indices in 50:50+33.....	88
Figure 3-16: Comparison of (A) the normalized Ge near edge and (B) the magnitude of the complex Fourier transform of $450^\circ\text{C}$ annealed 50:50 (solid black line), 50:50+10 (solid gray line), 50:50+20 (black dashed line), and Ge foil (black dotted line).....	90
Figure 3-17: Normalized Ge near edge comparison of $450^\circ\text{C}$ annealed 50:50+33 (solid black line) to $300^\circ\text{C}$ annealed GST (solid gray line). Apart from a change in the intensity of the white line, both share similar near edge features.....	91
Figure 3-18: Comparison of the magnitude of the complex Fourier transform of the Ge K edge EXAFS for $450^\circ\text{C}$ annealed 50:50+33 (solid black line) to $300^\circ\text{C}$ annealed GST (solid gray line).....	92
Figure 3-19: Comparison of the magnitude of the complex Fourier transform of the Ge, Sb, and Te K edge EXAFS for the as deposited 224 (solid black line), 225 (gray dashed line), 226 (solid gray line), and 224 (black dashed line). Only the range of interest ( $\sim 2 - 3\text{\AA}$ ) is shown for clarity.....	97
Figure 3-20: Fits to the Ge, Sb, and Te K edge for amorphous 225. Fit quality is representative of those obtained for 224, 226, and 227. Magnitude of the complex Fourier transformed of EXAFS spectra is shown. Solid black line = data, gray dashed line = fit.....	100
Figure 3-21: The Ge edge bond fractions for $\text{Ge}_2\text{Sb}_2\text{Te}_x$ samples.....	101



## Chapter 1 Introduction

S. R. Ovshinsky was first to propose and patent [1] the notion of a memory switch based on distinct material properties of the amorphous and crystalline phases of multi-component chalcogenides in the 1960's [2]. In the late 1980s, Matsushita / Panasonic developed chalcogenide based phase-change optical disc technology that remained stable over a million cycles [3], leading to widespread adoption of optical disk memory and resulting in the commercialization of the 4.7 GB digital versatile disc random access memory (DVD-RAM) in the 1990s. More recent interest focuses on the creation of a new solid state phase change memory (PCM) which would bypass the scalability concerns of the current technology (NAND, NOR, DRAM, FLASH) [4] while simultaneously improving latency and power consumption, as well as ensuring non-volatility and radiation hardness [5]. Of course, there are obstacles. Typical PCM materials such as  $\text{Ge}_2\text{Sb}_2\text{Te}_5$  (GST) require significant doping (or alloying) to shift their crystallization temperature ( $T_x$ ), sufficiently above standard CMOS device operation ranges ( $\sim 80^\circ\text{C}$ ) but also well below the melting point for thermal stability [6]. Etch processing is a crucial step en-route to fabricating energy efficient, high density, nano-scaled PCM memory devices, yet it can lead to unfavorable, irreversible modification of the GST material [7]. Chalcogens such as Te in GST can easily diffuse and interact unfavorably with the adjacent materials in the device structure thus negatively impacting the lifetime of a PCM device cell [8].

Fundamental studies of chalcogenide based phase change materials (PCMs) have several unanswered questions pertaining to the mechanism of the phase change. These

problems manifest themselves in the widespread difficulty of probing the local atomic environment of the PCM at the point of phase change. A direct consequence of this is the unclear structural role of the chalcogen in facilitating crystal nucleation and growth. This leads to ambiguity in the role of local structure in determining material properties. Many local structural studies have focused on mainstream PCMs utilized in optical disc technology, such as GST and AgInSbTe (AIST). These studies confirm X-ray Absorption Spectroscopy (XAS) as an ideal tool for probing the atomic environment of these PCMs, since sample crystallinity is not a precondition. XAS includes both the X-ray absorption near edge structure (XANES) and the extended X-ray absorption fine structure (EXAFS) spectroscopies, where XANES is useful for determination of the valence state and coordination geometry, while EXAFS can reveal the local molecular structure about the absorbing element in the sample. XAS is typically more conclusive when used in conjunction with X-Ray Diffraction (XRD), X-ray Photoelectron Spectroscopy (XPS), Fourier Transform Infrared Spectroscopy (FTIR), Transmission Electron Microscopy (TEM), or other techniques to illuminate the relationship between the structural configuration of the amorphous and crystalline phases and the observed thermal, optical, electrical, and mechanical properties of the system.

The research presented in this dissertation, “The Local Structure and Kinetics of Ge-Sb-Te Phase Change Materials for use in Solid State Applications”, originated in a multi-site collaboration driven by colleagues at Kirkland Air Force Research Laboratory. The work continued through a Joint Study Agreement established between our research group at North

Carolina State University in Raleigh, NC and the IBM/Macronix PCRAM Joint Project at the IBM T.J. Watson Research Center, in Yorktown Heights, NY. The experiments are all in timely response to urgent, pertinent questions on the correlation of the PCM's local structure to observed physical characteristics at various stages of material preparation for solid state memory device fabrication. While these experiments allow one to add to the already widespread discussion of the nature of the amorphous and crystalline phases of GST, they also address the nature and structural implications of doping/alloying GST, the local structural changes that occur post etch processing, and the nature of the Ge-Sb binary and the Ge-Sb-Te ternary alloys. The combination of XANES and EXAFS are complemented through the use of XRD, FTIR, and XPS in the belief that a complex structural system is often best understood in light of numerous experimental probes, with each providing correlative and unique data.

## **1.1 The Structural Implications of Nitrogen doping in GST**

In semiconductor nomenclature, doping refers to the introduction of donor (e.g. arsenic) or acceptor (e.g. boron) impurities into an intrinsic semiconductor in order to change the equilibrium carrier concentration. This results in either extrinsic n-type (donors) or p-type (acceptors) containing new dopant related energy levels in the band gap close to the conduction band or valence band, respectively [9]. In this formalism, GST can be characterized as a disordered p-type semiconductor in the amorphous phase (Fermi level pinned in the middle of band gap) [10], a narrow-gap p-type semiconductor in the fcc

structure (Fermi level located close to valence band) [11; 12], and a degenerate p-type semiconductor (metallic character, i.e Fermi level in valence band) in the hcp structure [12]. The term “doping” as it relates to GST, however, is a misnomer. Experimentally, GST has been tested with various dopants including nitrogen [13; 14; 15], tin [16], silicon [17], and oxygen [18], where typical dopant atomic concentrations are between 2% and 10%, which is 3-4 orders of magnitude higher than typically 0.001% atomic concentration of Ar in intrinsic Ge. Unlike an electrical response to impurity doping in Si and Ge semiconductors, doping in GST is meant to *modify the material properties* of the PCM. In previous studies of the optical and structural properties of nitrogen-doped GST (N-GST), the addition of nitrogen lead to grain refinement [19], crystal lattice distortions that induced strain in the films, increased resistivity of the amorphous state, and increased temperature for the transition from amorphous to the metastable, distorted rocksalt phase ( $T_x$ ) [20]. Tailoring  $T_x$  is critical since GST must be thermally stable over the typical range of temperatures for its solid state operating environment. Previous studies show that thermal cycling (annealing and cooling) of undoped GST films with temperatures from 30 to 80 °C (far less than ~140°C for  $T_x$  shown before [21]), leads to an irreversible increase in the refractive index and a growth of nano-crystals within the amorphous matrix [22]. XPS, FTIR, and XAFS demonstrate that nitrogen also plays an important chemical and structural role in N-GST, both in as-deposited and crystalline (fcc and hcp) GST thin films. These techniques reveal the chemical and local bonding environment around each of the elements in the sample, pre/post-anneal, at various doping concentrations. Results show that the nitrogen dopant remains at the grain boundary

of the GST crystallites, forming a locally, chemically ordered Ge-N bonding environment such that the annealed film is comprised of crystallites with a dopant rich grain boundary.

## **1.2 The Structural Implications of Reactive Ion Etching N-GST**

Scalability limitations far below the threshold of current memory technology represents one of phase change memory's most appealing attributes. Current metal oxide semiconductor field effect transistors (MOSFETs) and floating gate transistors, which are the fundamental building blocks of current NAND and NOR flash memory and DRAM, begin to suffer from reduced device performance when scaling beyond the 22nm node. As an example, quantum mechanical modeling has projected a gate oxide scaling limit of 20 Å before which chip standby power will become excessive due to electron tunneling currents [23]. The scalability of PCM based memory, on the other hand, suffers no physical limitations into the next 3-4 lithography generations [24] as 3nm doped eutectic Ge-Sb PCM bridge prototype memory cells have been recently reported [25]. Although fundamentally this may indicate that PCM based memory technology is easily scalable, one area in which scalability is still under evaluation is within the arena of materials processing and device fabrication. Reactive ion etching (RIE) in an Ar/Cl<sub>2</sub>/CHF<sub>3</sub> plasma chemistry allows anisotropic patterning of millions of high density, high fidelity phase change memory devices. However, a combined study of depth profiled XPS, TEM, and electron energy loss spectroscopy (TEM-EELS) concluded that this etch method inadvertently leads to selective removal of antimony and nitrogen along with an increased amount of oxidized tellurium [7].

More importantly, this study concludes that this layer penetrates to a thickness approximately 10nm into the material and shows the process to be chemically driven (independent of ion bombardment). A subsequent submission to the Journal of Applied Physics, shown in appendix 3, examines the chemical and structural effects of this etch modification layer and its implications for device performance and crystallization, from XPS, X-ray absorption fine spectroscopy (XAFS), time resolved laser reflectivity and time resolved X-ray diffraction (XRD). Laser reflectivity data shows that etch modification hinders nucleation in the optical device by changing the interfacial properties of the surrounding dielectric medium. In situ XRD data shows that the transition from the FCC to HCP phase is increased as a result of the etch modification layer, and this is likely due to formation of an oxide which desorbs at the HCP crystallization temperature. This oxide was confirmed by depth profiled XPS, as well as XAFS of partially and fully etch films. XAFS results revealed the nature of the etch modification region resulting from fluorine and chlorine etch chemistries, to consist of significant amorphous  $\text{GeO}_2$  and  $\text{Sb}_2\text{O}_3$ .

### **1.3 The local structure of GeSb & the role of Te in the Ternary System**

Although the commercial success of ternary GST is undeniable, due to its widespread adoption in optical storage, there are some consequences of Te which may challenge the realization of GST solid state memory. The low melting point and high vapor pressure of Te results in high mobility and therefore phase segregation and void formation during thermal cycling [26]. This mobility and subsequent Te aggregation on the grain boundaries also

allows Te to easily interact with the adjacent Ti adhesion layer in the device structure, forming exotic Ti-Te phases, which ultimately undermine the lifetime of the device [27]. These problems led to increased focus on alternative PCMs such as the binary GeSb alloys. Apart from circumventing the chalcogen related issues, these materials are more easily deposited (due to their simpler composition), and demonstrate great technological promise. Prototype phase change memory bridge cell devices fabricated using undoped eutectic Ge-Sb show very fast switching ( $\sim 10$ ns) and RESET currents ( $\sim 80$ uA) [28]. Anticipative results aside, in situ XRD studies and TEM of GeSb films show significant phase segregation and Ge precipitation post anneal, leading to serious questions regarding device reliability [29]. This dissertation clarifies the structural mechanism of Te in the ternary system and the phase segregation in the binary system, and investigates the structural role of the chalcogen in crystallization and nucleation. It is widely accepted that Te forms 2 fold coordinated linkages in the amorphous phase and occupies the 4a site in the NaCl-like rocksalt metastable crystal structure post anneal [30]. Of particular note is a proposed “umbrella flip” mechanism involving the Ge atoms, which attempts to explain the ultra fast crystallization mechanism in terms of the preservation of strong covalent bonds [31]. However, these results do not clarify the important role of Te during crystallization. XAFS of various GeSb and Ge-Sb-Te glasses in the binary and ternary systems, in conjunction with time resolved XRD presented in chapter 3, addresses these concerns. In the ternary compounds, thin films of GeSb with gradually increasing Te atomic concentration to demonstrate the role of Te plays in preventing phase segregation, while promoting stability, and crystal nucleation. We also

refine our data analysis by understanding typically un-used features at the near edge data and correlating these to structural phenomenon.

## 1.4 Outline of the rest of this Dissertation

This dissertation is a discourse on the structure-property relationships of PCMs obtained by combining EXAFS and XANES with complementary spectroscopies. Each chapter presents experiments, results, and discussions meant to illuminate the local structure of Ge-Sb-Te containing PCM, as it is modified for solid state memory applications. In chapter 2, XAFS, FTIR, XRD, and depth profiled XPS results on as-deposited and annealed N-GST films are presented along with a detailed description of the experiment and analysis. We discuss the implications of a predominantly germanium nitride dopant environment and relate this to the shift in  $T_x$ , as well as the observed grain refinement in TEM. Furthermore, a discussion of observed long range order of the N-GST crystalline environment raises important questions for future studies, but also emphasizes the distinct, separate dopant environment pre / post anneal. In chapter 3, we present a combined XAFS study of  $\text{Ge}_x\text{Sb}_{(1-x)}$  ( $x=75, 50, 25, 15, 4$ ) glasses together with the implications as Te is gradually added to the binary system. XAFS results of interesting ternary samples, including  $(\text{Ge}_{15}\text{Sb}_{85})_x\text{Te}_{(1-x)}$  ( $x = 0.9, 0.8$ ),  $(\text{Ge}_{50}\text{Sb}_{50})_x\text{Te}_{(1-x)}$  ( $x = 0.9, 0.8, 0.66$ ) and  $\text{Ge}_2\text{Sb}_2\text{Te}_x$  ( $x=4,5,6,7$ ) are presented in light of in situ time resolved XRD. These results allow us to show the role of Te in crystallization and nucleation, as well as its importance to structural stability post anneal. This chapter also develops formalism for understanding the often disregarded features

approximately 200 eV past the white line at the Ge K edge. These near edge spectra reveal electronic structure information resulting from core level, many electron final states and relate these to structural behavior. Finally chapter 4 presents our conclusions followed by the appendix.

## Chapter 2 The Structural Implications of Nitrogen doping in GST

The primary purpose of nitrogen doping is to advantageously modify the material properties of the GST system. These effects can be understood structurally via a combination of XAFS (XANES and EXAFS), FTIR, XPS, and XRD, where the *in-situ* time resolved XRD measurements and depth-profiled XPS measurements were performed by others. Chapter 2 is organized as follows. In section 2.1, we introduce and describe the ATR-FTIR measurements of as-deposited N-GST, while section 2.2 presents the results and analysis of the observed IR vibrational modes. Section 2.3 presents the depth profile XPS of the Ge 2p<sub>3/2</sub> spectra of 5 atomic percent nitrogen doped GST (5%N-GST) versus undoped GST. The EXAFS equation is introduced in section 2.4. In section 2.5, we present the as-deposited N-GST XAFS analysis, consistent with our FTIR and XPS data. This section includes the near edge analysis (2.5.1), the local structural analysis from EXAFS (2.5.2) and a description of the modeling and fitting done (2.5.3).

The remaining sections of chapter 2 present the local structural role of the dopant in the crystallization. This is done by comparing *in-situ*, time resolved, XRD measurements (section 2.6) and XAFS results (section 2.7) for 5%N-GST after various annealing conditions. Section 2.8 concludes the chapter with a brief discussion of local structure of the distorted rocksalt structure observed in FCC annealed N-GST samples.

## 2.1 Amorphous N-GST ATR-FTIR Measurements

A Nicolet Nexus 870 Fourier transform infrared spectrometer (FTIR) with a Harrick attenuated total reflection (ATR) accessory was used to measure the nitrogen vibrational modes within the N-GST films. The ATR microscope objective contains a small internal reflection element (IRE) fabricated from a pure Ge crystal, and placed at the focus of a Cassegrain optic, i.e the sample contact surface. The contact surface is circular and typically smaller than sample pieces cleaved for measurements. The spectral region examined was from  $400 - 4000 \text{ cm}^{-1}$  at a resolution of  $4 \text{ cm}^{-1}$  and was detected by a liquid nitrogen cooled MCT detector. N-GST samples were prepared by DC reactive sputtering from a  $\text{Ge}_2\text{Sb}_2\text{Te}_5$  compound target in a mixture of argon and nitrogen feedgas chemistries to thicknesses of 100 nm or 1000 nm on bare Si wafers. The nitrogen flow rate was varied between 0, 13, and 100 sccm for the 100 nm films, but only 100 sccm for the 1000 nm thin film (sccm = standard cubic centimeter per minute at STP). Previous compositional measurements showed that the 13 sccm N flow rate resulted in approximately 5% bulk N atomic concentration.

An ATR accessory facilitates FTIR measurements on samples that are too thick for transmission IR measurements [32], and is ideal for N-GST thin films on thick bare Si wafers. It utilizes internal reflectance, where IR light is directed into the IRE, at a critical angle causing total internal reflections as it passes through the Ge crystal. At each reflection a part of the light, called the evanescent wave passes beyond the crystal interface and interacts with the N-GST sample. The sample must be bolted firmly to ensure close contact, but carefully to prevent damage to the objective. If the sample is IR active at any energy, this

evanescent wave will be attenuated, and this intensity change will be recorded as the IR light exits the crystal and passes through the spectrometer to the detector. The crystal material used for the IRE affects the measurement; each crystal's particular refractive index affects the depth of penetration and the occurrence of anomalous dispersion.

Effective depth of penetration into the sample depends on the wavelength of the radiation, the refractive indices of both sample and IRE, and on the angle of incidence of the radiation, as given, to a good approximation, in the equation below first proposed by Harrick [33],

$$d_p = \frac{\lambda}{2\pi n_1 (\sin^2 \alpha - n_{21}^2)^{1/2}} \quad [\text{Eqn. 2.1}]$$

where  $\lambda$  is the wavelength of the radiation,  $\alpha$  is the angle of incidence,  $n_1$  is the refractive index of the IRE,  $n_2$  is the refractive index of the sample and  $n_{21}$  is  $n_2/n_1$ . Numerous IREs are in use including Ge, Si, ZnSe and diamond ( $n= 4, 3.4, 2.4$  and  $2.4$ , respectively), but we only had access to a Ge objective.

Table 2-1: Calculated penetration depth ( $d_p$ ), and the estimated final depth after passing through a 100nm and 1000nm thick sample, for the spectral range observed.

wave # (cm-1)	$\lambda$ (m)	$d_p$ (m)	100nm- $d_p$ (m)	1000nm- $d_p$ (m)
400	2.50E-05	1.67E-06	-1.57E-06	-6.67E-07
550	1.82E-05	1.21E-06	-1.11E-06	-2.12E-07
700	1.43E-05	9.52E-07	-8.52E-07	4.76E-08
850	1.18E-05	7.84E-07	-6.84E-07	2.16E-07
1000	1.00E-05	6.67E-07	-5.67E-07	3.33E-07
1150	8.70E-06	5.80E-07	-4.80E-07	4.20E-07
1300	7.69E-06	5.13E-07	-4.13E-07	4.87E-07
1450	6.90E-06	4.60E-07	-3.60E-07	5.40E-07

Using a Ge crystal IRE, a typical angle of incidence of  $45^\circ$  and a typical sample refractive index of 1.5, table 2-1 shows the penetration depths  $d_p$ , and the resultant penetration into a 100nm and 1000nm thick sample over the IR spectral range used for our analysis. Table 2-1 shows that over the range of  $\sim 700 \text{ cm}^{-1}$  and higher wavenumbers, we are more likely to sample within the bulk of a 1000nm thick sample (positive values), and the substrate of the 100nm thick sample (negative values).

## 2.2 Amorphous N-GST ATR-FTIR Results and Analysis

We measured a bare Si wafer sans N-GST, and noticed that there was significant IR activity, due to impurities in the Si wafer. No analysis was performed on these background spectra, except to approximate the location of these features for subsequent discrimination from the N-GST data. This spectrum was identical to a measurement of 100nm thick, undoped GST, as expected from the expected depth of penetration ( $100\text{nm}-d_p$ ), into an IR inactive sample. Figure 2-1 (A) to (D) shows the subsequent measurements of the doped N-GST samples compared to the bare Si wafer. In figure 2-1, there is clearly a doublet feature just between  $700\text{-}800 \text{ cm}^{-1}$  which scales with N atomic % and film thickness. These absorption features were deconvolved using multiple Gaussian peak fitting in Origin 5.0, where the consistent variation in each spectra was due to peaks at  $770$  and  $720 \text{ cm}^{-1}$ . The group formed by a planar bonded N atom and its three Ge neighbors is the skeletal  $\text{Ge}_3\text{N}$  group, with normal modes of vibration given by [34]: a breathing mode, an out-of-plane stretching mode, the symmetric and asymmetric in-plane stretching mode, and an in-plane bending mode. The

asymmetric stretching vibration involved the displacement of the N as well as the three Ge neighbors; it is the most strongly IR active and has an intensity proportional to the N concentration [35].

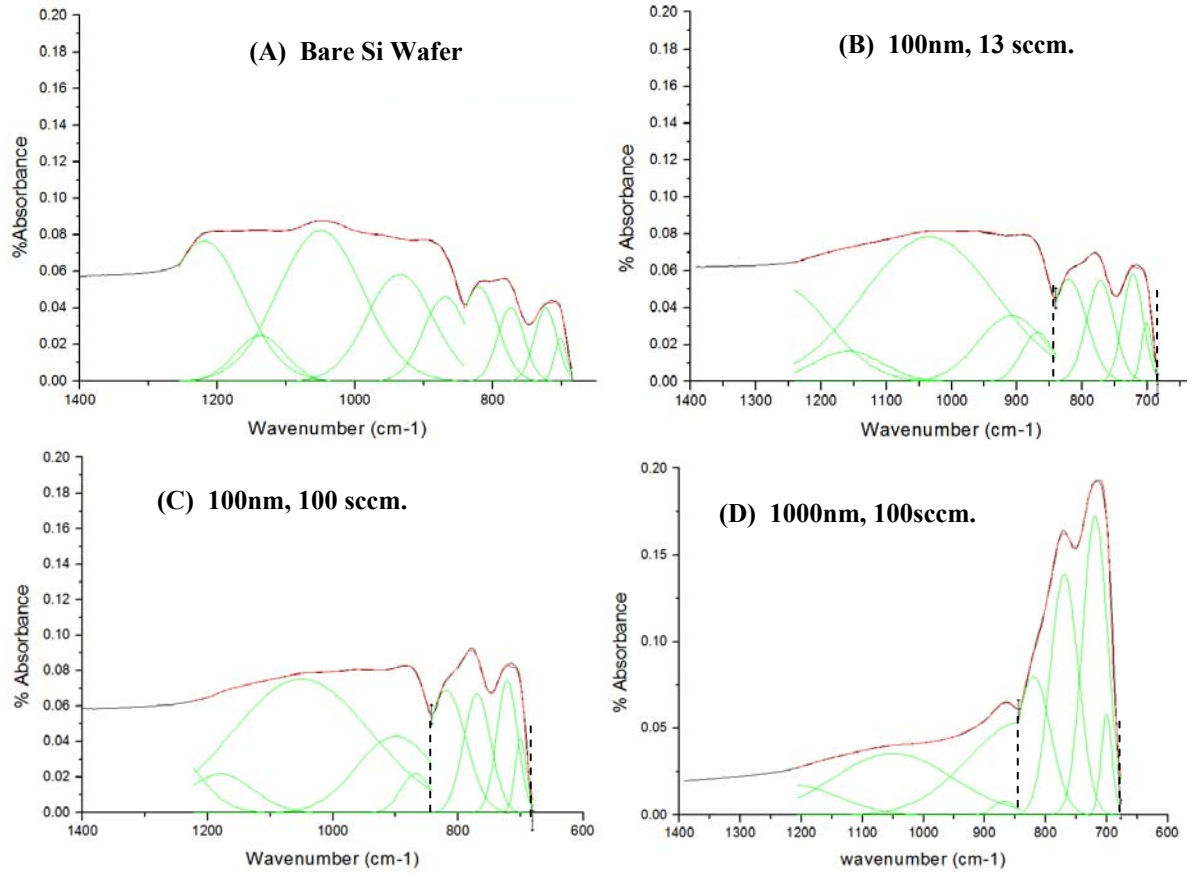


Figure 2-1: FTIR spectra showing % Absorbance vs wavenumber for N-GST samples and a bare Si wafer. The titles in B, C, and D refer to the film thickness (nm) and N flow rate (sccm.) used for deposition. The fine dashed lines are fits to the spectra, with the fitting range indicated by vertical dashed lines.

The main absorption features in figure 2-1 at 770 and 720  $\text{cm}^{-1}$  is the asymmetric stretching mode, as previously observed in IR spectroscopic studies of amorphous  $\text{Ge}_x\text{N}_{(1-x)}$  [36]. More stable compounds of  $\alpha\text{-Ge}_3\text{N}_4$  and  $\beta\text{-Ge}_3\text{N}_4$  actually displayed more resemblance to our spectra [37; 38], the most notable being a plasma nitrided Ge sample hypothesized to

consist of 80%  $\beta$ -Ge<sub>3</sub>N<sub>4</sub> + 20%  $\alpha$ -Ge<sub>3</sub>N<sub>4</sub> having identically observed bands at 780 cm<sup>-1</sup> and 730 cm<sup>-1</sup> [38]. These results imply an ordered germanium nitride forms in as deposited N-GST, but do not provide an acceptable explanation for this, considering that N-GST films deposited by plasma reactions are expected to be completely amorphous. It is known that the presence of back impurity atoms of a different electronegativity, and even the absence of back atoms, i.e. the inclusion of dangling bonds, influences the charge distribution around the Ge-N dipole, thus changing the position of the absorption band [39; 40]. The resulting shift of the absorption peak may be to lower [41] or higher [42] energies, depending on electronegativity of the back atom. It is therefore possible that the doublet feature in the N-GST samples in figure 2-1 represents the influence of the Ge-Te and Ge-Sb next nearest neighbor environment on the charge distribution of the Ge-N dipole.

### **2.3 Amorphous N-GST Depth Profile XPS**

XPS spectra were collected about the Ge 2p<sub>3/2</sub> binding energy of as-deposited, 100nm thin films of 5%N-GST and undoped GST, deposited in the manner described in section 2.1. XPS measurements were performed by Dolores Miller, using a Physical Electronics Quantum 2000 ESCA Microprobe using a monochromatic Al K<sub>a</sub> source with a 200  $\mu$ m spot size. Charge neutralization (or compensation) is performed as necessary, since a positive charge can accumulate upon electron ejection from low resistance films (such as as-deposited GST). Depth profiling was done using 1.0 keV Ar<sup>+</sup> ions, 3 x 3 mm raster. High resolution scans (46 eV pass energy; 0.2 eV/step) were taken at a 45° take-off angle between the sample

and the analyzer axis. Figure 2-2 shows the results of the first depth profile XPS spectra for 5%N-GST and GST into a depth of approximately 34nm and 17nm, respectively.

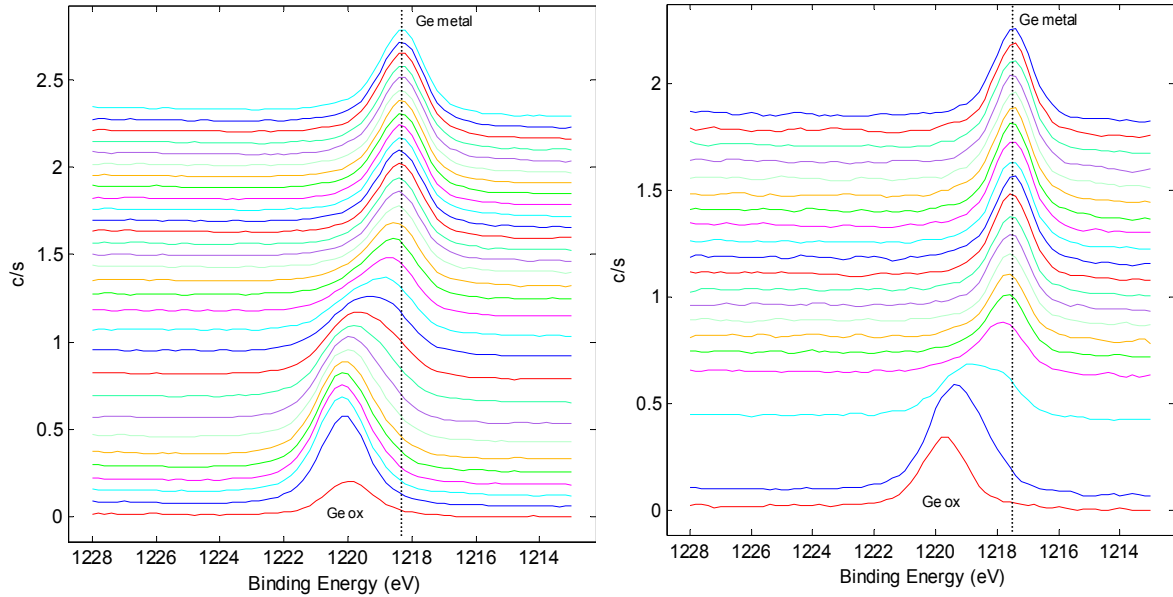


Figure 2-2: Comparison of depth profiled XPS Ge 2p<sub>3/2</sub> binding energy spectra for A) 5%N-GST and B) GST. The 5%N-GST spectra represents a depth of ~34nm versus ~17nm for the GST sample. The dashed line in both spectra shows the binding energy of the final depth profile.

The vertical dashed lines in the figure above represent the binding energy of the final depth profile (presumed to be from the metallic Ge bonds as compared to the GeO<sub>x</sub> bonds at the near surface) and show that there is a shift in binding energy in 5%N-GST (1218.25) as compared to GST (1217.5). This agrees well with previously published Ge 2p<sub>3/2</sub> XPS results for Ge<sub>3</sub>N<sub>4</sub> (1218.8) [43] and crystalline Ge (1217.38) [44], and provides additional evidence of a shift in binding energy due to the formation of Ge-N bonding. Furthermore, no similar shifts were observed at Sb or Te 3d peaks. The N 1s peak was present in 5%N-GST, as expected, occurring at a binding energy of ~397.5, which was similar to the 397.4 reported for Ge<sub>3</sub>N<sub>4</sub> [43] but was 0.4eV more than previously observed in N-GST films by others [45].

These XPS and FTIR measurements both confirm the formation of Ge-N bonding as nitrogen is added to GST.

## 2.4 The EXAFS Equation

During XAFS measurements, we record X-ray intensities; that is, the intensity of an incident and transmitted X-ray beam through a given sample, or the intensity of incident and fluorescent X-rays (i.e. fluorescence mode). We obtain the X-ray absorption coefficient  $\mu(E)$ , given by  $\mu(E)x = \ln(I_o/I_t)$  (transmission) or  $\mu(E)x = (I_f/I_o)$  (fluorescence), where  $x$ ,  $I_o$ ,  $I_t$ , and  $I_f$  are the sample thickness, and intensities of the incident, transmitted, and fluoresced X-rays, respectively.  $\mu(E)$  is the probability for an X-ray to be absorbed by a sample. For an isolated atom, for instance a monoatomic gas, the measured  $\mu(E)$  looks roughly like a decaying step function. This step function is broadened by lifetimes of the core hole [46] and of the excited photoelectron, as well as the energy resolution of the experimental apparatus. For an atom in condensed matter, this broadened, decaying step function is modulated by an oscillatory fine structure associated with the presence of surrounding atoms. It is this oscillatory structure which is called the EXAFS. We isolate and analyze this in order to yield information of the local structural environment of the excited atom.

Sayers, Stern, and Lytle forever changed EXAFS theory when they showed that an appropriate Fourier analysis of the EXAFS data can locate the positions of atoms

surrounding the excited atom [47]. This changed EXAFS from a qualitative effect to a quantitative one, allowing accurate comparison of experimental data to theoretical models for amorphous solids and complex materials. The derivation and development of modern EXAFS theory, including important approximations (e.g. self energy effects) and methods of data analysis is covered in detail by others [48; 49; 50; 51]. A conceptually transparent, plane wave approach to the EXAFS equation is shown in appendix 1, which shows off much of the essential physics. This EXAFS equation, is shown in eqn. 2.2 in terms of a sum of the contributions from all scattering paths of the photoelectron:

$$\chi(k) = \sum_j N_j S_o^2 F_j^{eff}(k) e^{-2\sigma_j^2 k^2} e^{-2r_j^2/\lambda_j(k)} \frac{\sin(2kr_j + \vartheta_{oj}(k))}{kr_j^2} \quad [\text{Eqn. 2.2}]$$

with  $r_j = r_{oj} + \Delta r$  [Eqn. 2.3]

and  $k^2 = \frac{2m_e(E - E_o + \Delta E_o)}{\hbar}$  [Eqn. 2.4]

Here  $k$  is the photo-electron wave vector,  $E_o$  or ( $E_F$ ) is the Fermi energy, and  $r_j$  is the interatomic distance between the absorber and the coordinating atoms,  $\Delta r_i$  is the slight (<0.1 Å) calculated change to the interatomic distance relative to the initial  $r_j$ , and  $\Delta E_o$  is the calculated change in the photoelectron energy value used to align the energy scale of the theoretical spectrum to match the measured spectrum.

$N_j S_o^2$  are amplitude terms, which modify the amplitude of the EXAFS signal and do not have a  $k$ -dependence.  $N_j$  represents the number of coordinating atoms within a particular shell for single scattering, or it is the number of identical paths (path degeneracy) in multiple scattering. The passive electron reduction factor ( $S_o$ ) accounts for the slight relaxation of the

remaining electrons in the presence of the core hole vacated by the photoelectron, and usually has a value between 0.7 and 1.0 [52]. The amplitude is reduced by the  $\frac{1}{r_j^2}$  term, i.e. contributions diminish for shells of atoms located at increasing distance from the absorber. The amplitude is further modified by  $e^{-2\sigma_j^2 k^2}$ , where  $\sigma_j^2$  is the mean-square displacement of the bond length between the absorber atom and the coordinating atoms in a shell. It has contributions from dynamic (thermal) disorder as well as static disorder (structural heterogeneity). Increasing the distribution of distances within a single shell decreases the amplitude of the EXAFS signal because the phase differences between outgoing and scattered photoelectrons are shifted slightly for each atom in the coordination shell. The EXAFS process occurs on the femto-second ( $10^{-15}$  s) time scale, while thermal vibrations occur on a much longer time scale of  $10^{-10}$  to  $10^{-12}$  s. Because the atoms are essentially “frozen” at one position about their thermodynamic minima during the excitation process, EXAFS measures the distribution of the distances between the absorber atom and each of the coordinating atoms within a shell in terms of a  $\sigma_j^2$  value.

$e^{-2r_j^2/\lambda_j(k)}$  also modifies the amplitude, and is due to inelastic losses in the scattering process. It depends on photoelectron mean free path  $\lambda_j(k)$ , and explains why the EXAFS signal is dominated by the scattering contributions from atoms within approximately 10 Å of the absorber atom; this makes EXAFS a local structural probe.

$F_j^{eff}(\mathbf{k})$  is the effective scattering amplitude. For a single scattering path it is the atomic scattering factor used in XRD. For a multiple scattering path it is the effective scattering

amplitude written in terms of the single scattering formalism [53]. Atoms with more electrons scatter photoelectrons more strongly at higher wavenumbers, and thus  $F_j^{eff}(k)$  depends on the atomic  $Z$  number. This presents a difficulty in distinguishing between the EXAFS signal from say, Ge-N and Ge-O backscatters on the basis of their scattering amplitudes alone.

$\sin[2kR_i + \varphi_i(k)]$  accounts for the oscillations in the EXAFS equation and describes the path,  $2r_i$  of the photoelectron, multiplied by  $k$  to give it its phase.  $\varphi_i(k)$  is the phase shift caused by the photoelectron's interaction with the surrounding atomic environment. It is the Fourier transform of this sine term, which allows us to observe and parameterize separate shells (peaks) at distances related to  $r_i$ . However, the peak is not precisely at  $r_i$  due to  $\varphi_i(k)$ , which causes a shift of  $\sim -0.5 \text{ \AA}$ .

Computer programs, such as FEFF, calculates the effective scattering amplitude  $F_j^{eff}(k)$ , effective phase shift  $\vartheta_{oj}(k)$ , and, the mean free path of the photoelectron  $\lambda_j(k)$ , for each atom in a path using first principles [54].

## 2.5 Amorphous N-GST XAFS Analysis

XAS measurements were performed at MRCAT beamline ID-10 [55], at the Advanced Photon Source (APS) at Argonne National Laboratory, in Argonne, IL as well as NIST beamline X23A2 [56] at the National Synchrotron Light Source (NSLS), Brookhaven National Laboratory, in Upton, NY. Appendix 2 highlights some important experimental considerations, pertaining to the energy selection method (monochromator type, monochromator slits), harmonic X-ray elimination (detune percentage, type of mirror), focusing optics (KB mirrors, zone plates), the sample geometry (grazing incidence, rotating stage), detector specifications (ionization chambers, solid-state detectors, filters, fill gases), and the incident X-ray beam profile. Effective harmonic rejection is of particular significance for samples containing Ge + (Sb and/or Te) since a typical Si crystal monochromator at the Ge K edge (11103 eV) will diffract, according to Bragg's Law, both the fundamental harmonic ( $k=1$ ) as well as the third harmonic ( $k=3$ ). The 3<sup>rd</sup> harmonic, with energies  $\sim 33309$  in this case, increases the probability that Sb or Te photoelectrons will be excited, to the detriment of Ge absorption spectrum. The principal XAFS samples were thin films of varyingly doped N-GST deposited to approximately one micron film thickness, at room temperature on 200mm bare Si wafers and 0.2mm glass substrates (for transmission EXAFS) by DC reactive sputtering a  $\text{Ge}_2\text{Sb}_2\text{Te}_5$  compound target in a mixture of argon and nitrogen feedgas chemistries. The nitrogen flow rate was varied between 0, 5, 13, and 18 sccm which corresponded to bulk nitrogen atomic concentrations of 0, 2.5, 5, and 6.1 at% as

confirmed by Rutherford Backscattering Spectrometry (RBS), Particle Induced X-ray Emission (PIXE), and Auger Emission Spectroscopy (AES).

Four or more EXAFS spectra were collected for each sample, and these raw data were subsequently aligned and averaged (merged). The merged spectrum, is then normalized using a standard algorithm [48] of pre-edge subtraction and edge-step normalization. Additionally, the fine structure oscillations are isolated using the AUTOBK [57] program. All important preprocessing features, such as alignment, merging, normalization and background removal are implemented in a user-friendly manner by ATHENA [58], which is a GUI to IFEFFIT [59]. To model EXAFS spectra, we utilize Athena for background refinement, and ARTEMIS (another GUI to IFEFFIT) for building structural models and optimizing these versus the experimental data [58]. IFEFFIT is an interactive engine containing the algorithms for fitting the theoretical FEFF calculations [60]. FEFF calculates well spaced atomic potentials based on the scattering processes from a cluster of atoms, *with respect to the absorber atom*, providing that an initial structural model (e.g an isomorphic crystal structure) is supplied. Table 2-2 briefly summarizes the computer programs mentioned here.

Table 2-2. Summary of Programs used for XAFS Analysis

<i>Program</i>	<i>Purpose</i>	<i>Input</i>	<i>Output</i>
Athena	GUI to IFEFFIT for background removal, normalization, XANES Analysis, etc.	Absorption data $\mu(E)$	Norm $\mu(E)$ , EXAFS $\chi(k)$ and $\chi(R)$ spectra
Artemis	GUI to IFEFFIT and FEFF for fitting theoretical model to experimental data	EXAFS $\chi(k)$ spectra	Best fit model / Results
FEFF	Calculates $F_j^{eff}(k)$ and $\Phi_j^{eff}(k)$ based on atom cluster.	Cluster of Atoms	Theoretical EXAFS
IFEFFIT	Interactive engine for performing least squares fitting of FEFF theory to experimental data	IFEFFIT script	Results from processes

### 2.5.1 Near Edge Analysis

Normalization is particularly important, specifically for a standards based approach to XANES analysis. It negates differences between  $\mu(E)$  spectra due to absorber element concentration, measurement type (fluorescence / transmission), sample preparation and thickness, and detector response. Consequently, variations in the near edge are ascribed to differences in local molecular bonding environment and/or allowed electronic states. Figure 2-3 shows a comparison of as deposited, 5% N-GST, Ge K edge absorption spectra taken at different beamlines, with different fluorescence detectors, before and after normalization.

The normalization process involves a regression to the absorption edge in the pre-edge region ( $-200$  to  $-30$  eV before the edge energy) and the post-edge region ( $50$ – $1000$  eV above the edge energy). We typically regress a linear function to the pre-edge region, and a linear or quadratic function to the post-edge region. These lines are extrapolated to the absorption edge,  $E_0$ , and the difference in absorption between these projected lines at  $E_0$  is called the edge step. Finally, normalized  $\mu(E)$  spectra are produced by subtracting the pre-edge line from the entire data spectrum and then dividing the spectrum by the step height. In the normalized spectrum, the pre-edge region lies along zero absorption and the edge step is 1.

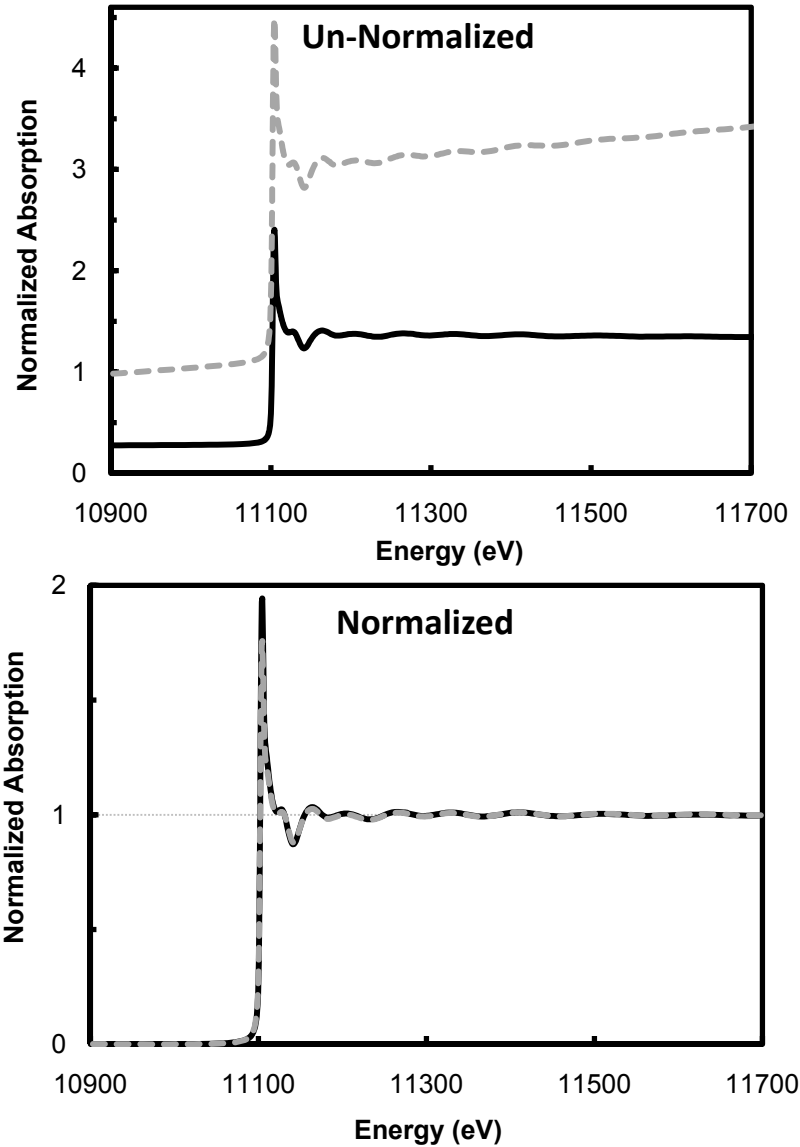


Figure 2-3: A comparison of the un-normalized and normalized Ge K edge absorption data for 5%N-GST. The solid black line was 1000nm thick film on glass substrate, measured at the APS, MRCAT beamline ID-10, using Ar / N mixture in the ionization chamber. The gray dashed line was 100nm film on a bare Si wafer, measured at the NSLS, NIST X23A2 beamline. On either occasion, fill gases of different ratios of Ar / N were used in the ionization chamber.

As shown above, normalization removes detector effects, and allows us to *directly compare* samples measured under different circumstances. A direct comparison of normalized as-deposited N-GST near edge spectra vs nitrogen flow rate, shown in figure 2-4,

reveals a feature just after the absorption edge which clearly scales as a function of nitrogen atomic concentration.

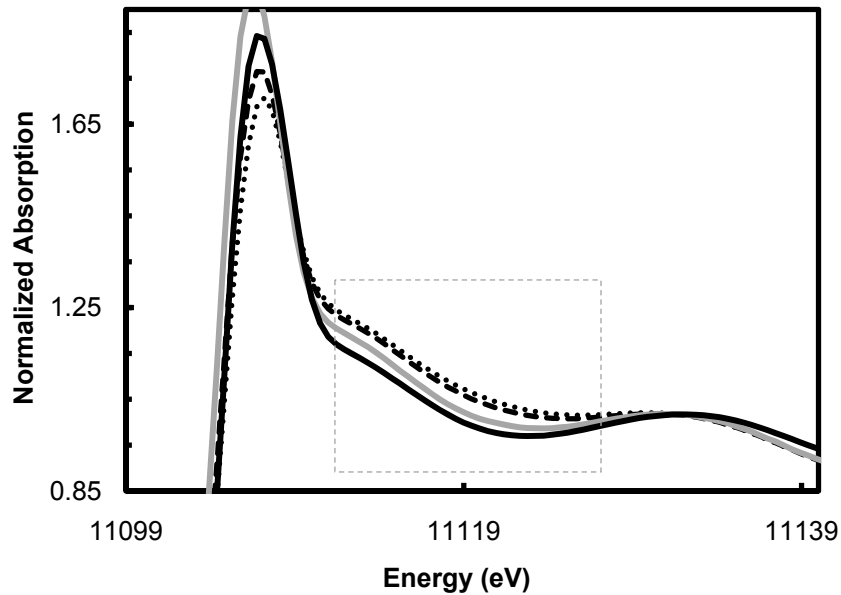


Figure 2-4 : Normalized Ge near edge comparison of as deposited 6.1%N-GST (black dotted line), 5%N-GST (black dashed line), 2.5%N-GST (gray solid line), and GST (black solid line). The feature that is scaling with nitrogen concentration is indicated just past the white line.

Presuming this is Ge-N related, from our FTIR and XPS study, an understanding of the structural standards for thermally stable Ge-N compounds is required. Of numerous published works characterizing germanium nitride, we obtained the near edge spectra for  $\beta$ - $\text{Ge}_3\text{N}_4$ , which exhibits an almost matching feature about 22eV past the edge [61], shown in figure 2-5 (A) with an associated EXAFS spectrum shown in figure 2-5(B) [62].

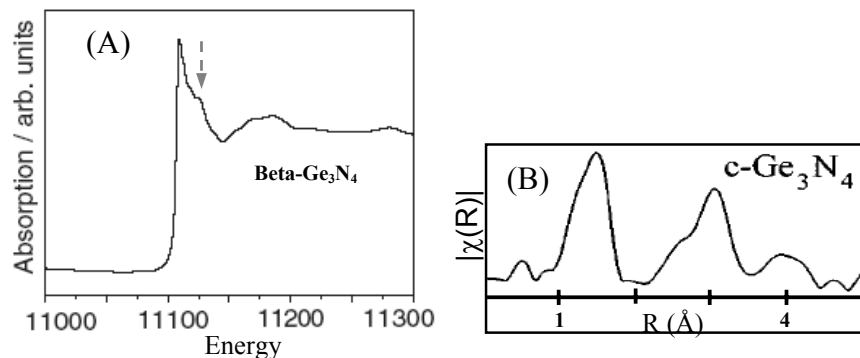


Figure 2-5: (A) Near Edge Spectra of beta-Ge<sub>3</sub>N<sub>4</sub> (arrow indicates the main identifying feature for these) and (B) Fourier transformed EXAFS spectra for beta-Ge<sub>3</sub>N<sub>4</sub> (Republished from [62]).

The authors of that work showed clearly that of the possible bond geometries, the two main peaks in stable Ge<sub>3</sub>N<sub>4</sub> are due only to Ge-N bonds and Ge-N-Ge next nearest neighbor interactions, as per a well classified distorted tetrahedral germanium nitride model [63]. The correspondingly strong distinct feature in the near edge of a well ordered compound such as Ge<sub>3</sub>N<sub>4</sub>, is not mere coincidence. Observed features in the near edge region are due to the photoelectron mean free path,  $\lambda_j(k)$  is quite large, typically tens of Ångstroms [64], just after excitation at the absorption edge. On the other hand,  $\lambda_j(k)$  is a few Å at EXAFS energies, leading to attenuation of contributions from longer paths. This explains why reasonably good approximate theoretical fits to experimental EXAFS,  $\chi(k)$  via single and low order multiple scattering (MS) paths can be obtained. The normalized near edge and magnitude of the Fourier transformed R-space spectra for one of our experimental standards, amorphous germanium nitride (a-GeN) is shown in figure 2-6.

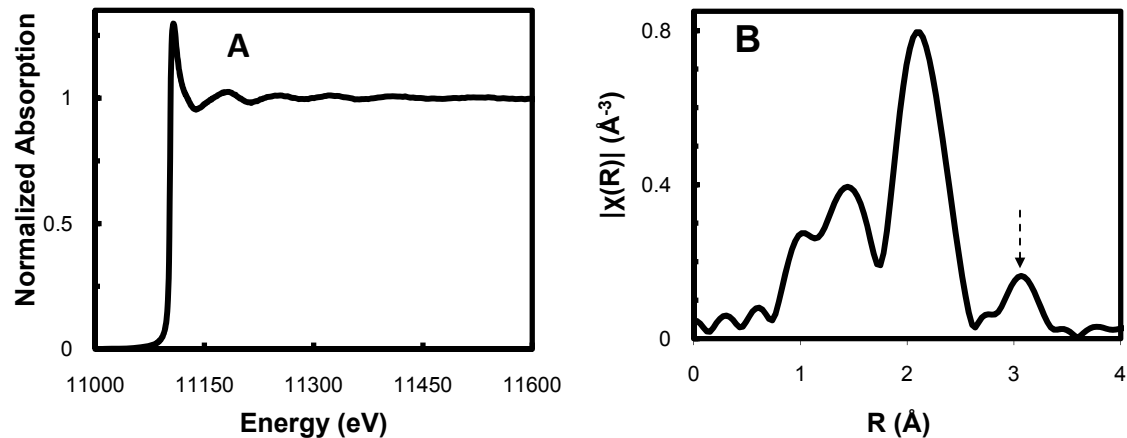


Figure 2-6: (A) Near Edge Spectra of a-GeN and (B) Magnitude of Fourier transformed EXAFS spectra of a-GeN. The  $\chi(k)$  data used for the Fourier transform, used a data range,  $\Delta k = 3 - 13 \text{ \AA}^{-1}$ , and followed our typical background removal procedures.

In this sample, the near edge feature due to MS contributions is not as apparent, as expected from the disordered as-deposited system, but also since a direct near edge comparison with changing N atomic % was not performed. The R-space spectra figure 2-6 (B) shows a distinct multiple scattering shell, indicated by the arrow. Others have measured XAFS of similarly deposited a-Ge<sub>(1-x)</sub>N<sub>x</sub> thin films, obtained identical data, and modeled the XAFS data using Artemis and IFEFFIT [62]. These authors used ATOMS, to generate the theoretical paths using the  $\beta$ -Ge<sub>3</sub>N<sub>4</sub> unit cell parameters, with atomic contributions for a distorted tetrahedral Ge-N 1<sup>st</sup> shell, as well as high amplitude forward scattering Ge-N-Ge next nearest neighbor paths. They also included an ATOMS generated first shell of tetrahedral covalent Ge bonds found in amorphous Ge, and combined the two environments by varying a mixing fraction. Their approach is acceptable, and widely employed in the EXAFS analysis of mixed systems with well defined coordination shells.

### 2.5.2 EXAFS Analysis

Prior to analysis, N-GST samples were set to identical background removal parameters, as shown in figure 2.7. In general accurate background removal is especially difficult for the structural study of elements with short bond distances, such as Ge-N bonding ( $\sim 1.83 \text{ \AA}$ ): background contributions are low frequency oscillations which can overlap with the Ge-N first shell structural content. Background removal is the process of approximating the functional form of the atomic background,  $\mu_o(E)$  [65] and subtracting it from the absorption cross section,  $\mu(E)$  to isolate the EXAFS where  $\chi(E) = \frac{\mu(E) - \mu_o(E)}{\mu_o(E)}$ . In practice, it is not possible to know  $\mu_o(E)$  since one must have *a priori* knowledge of the embedded atom potential, as well as *ab initio* knowledge of multi-electron effects, and the experimental setup (e.g, attenuation of the X-ray in air, harmonic content of the beam, etc.) [66]. Thus, we usually determine this empirically using the AUTOBK program or fitting standards from FEFF. Background removal using AUTOBK [57] employs a set of b-splines [67] to approximate the functional form of  $\mu_o(E)$ , where knots of the spline [68] are placed evenly in wave vector  $k$ , and the number of knots are determined by the information content of the background portion of the data. Since  $k$  and path length  $2r_i$  are Fourier conjugate variates, the shortest path length sets a lower limit on the contribution to the frequency content of  $\mu(E)$  due to scattering from neighboring atoms. Therefore, the low frequency portion of  $\mu(E)$  is due to  $\mu_o(E)$  while the high frequency is due to  $\chi(E)$ , and the cutoff frequency between these two regimes is  $2R_{bkg}$ , where  $R_{bkg}$  is a distance smaller than  $r_j$ .



Figure 2-7: Athena screen shot showing background removal parameters (used in AUTOBK) for N-GST samples. The  $k$  range is the range over which a spline using  $N_{\text{knots}}$  knots was optimized to approximate the background function.  $E_0$  is typically set to the maximum of first derivative of  $\mu(E)$  and can be used to align multiple data sets.  $K$ -weight also us to further tune to frequencies to be minimized below  $R_{\text{bkg}}$ . Pre-edge and normalization range specifies the range used to define the pre-edge and post-edge lines. Spline range defines the range over with AUTOBK minimizes the background.

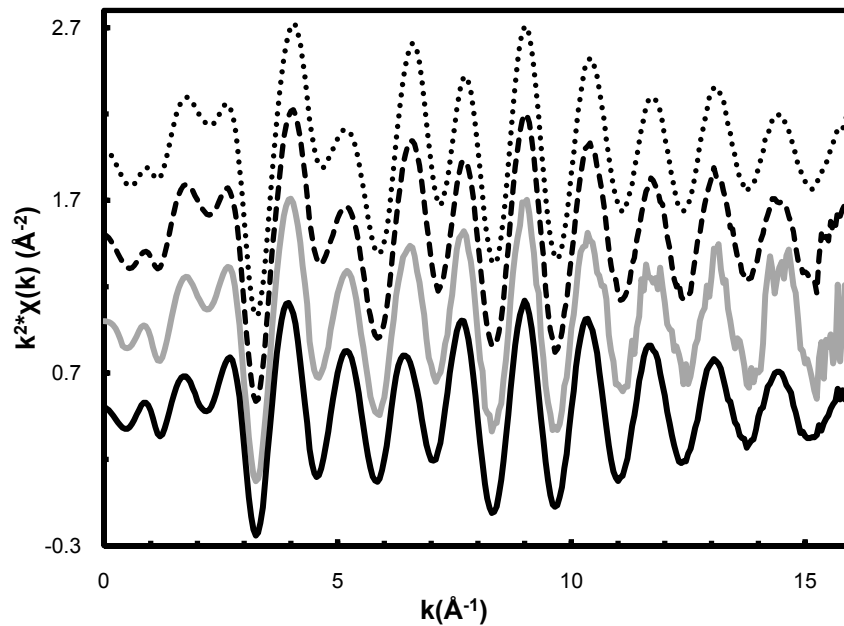


Figure 2-8:  $\chi(k)$  extracted from the  $\mu(E)$  of as-deposited 6.1%N-GST (black dotted line), 5%N-GST (black dashed line), 2.5%N-GST (gray solid line), and GST (black solid line), using the AUTOBK program. Each spectrum is the average of at least four fluorescence measurements. Each  $\chi(k)$  function is multiplied by  $k^2$  to emphasize the high-energy oscillations, as shown on the  $y$ -axis.

Figure 2-8 shows the  $\chi(k)$  spectra extracted from  $\mu(E)$ , using the background removal values above. The presence of high  $k$  noise in 2.5%N-GST lead us to use  $\Delta k = 3-13 \text{ \AA}^{-1}$  for the comparison in figure 2-9. Since EXAFS oscillations rapidly diminish with increasing energy, it is normal to multiply  $\chi(k)$  by either  $k$ ,  $k^2$ , or  $k^3$ , to emphasize the high

$k$  portion of the data. As a rule, all  $\chi(k)$  data in this dissertation will be  $k^2$  weighted (e.g y-axis label of figure 2-8), and the magnitude of the FT will similarly always reflect this, (e.g y-axis label of figure 2-9).

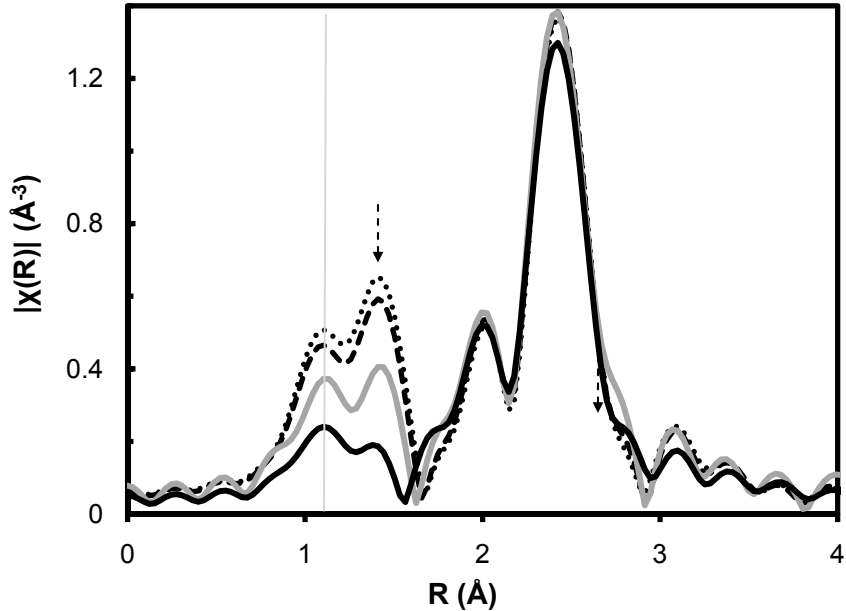


Figure 2-9: Magnitude of Fourier transformed EXAFS spectra of 6.1%N-GST (black dotted line), 5%N-GST (black dashed line), 2.5%N-GST (gray solid line), and GST (black solid line), using a window range of  $\Delta k = 3-13.5 \text{ \AA}^{-1}$ . The gray line shows the background feature.

Figure 2-9 is the magnitude of the complex FT of  $\chi(k)$ , that is  $|\chi(R)|$ , for these data sets. At  $\sim 1.1 \text{ \AA}$ , in all cases, there is a split shell which can be misleading. Indeed, if the feature at  $\sim 1.1 \text{ \AA}$  was structure related to surface oxide or impurities on the substrate prior to deposition (which may form an unknown Ge interfacial layer), we would not expect it to increase in proportion to Ge-N bonding feature as observed. This is not a real feature, but rather FEFF's (specifically, AUTOBK) difficulty in defining a background function in the near edge-region of the spectra, where the absorption spectrum changes abruptly and beyond the flexibility of a spline. An appropriate cutoff is needed here to exclude the Fourier

components that are longer in wavelength than that in the Ge-N EXAFS structure [69] by setting a maximum  $R_{\text{bkg}}$ , below which contributing Fourier components are considered to be part of the background. For our N-GST data,  $R_{\text{bkg}}=1.0\text{\AA}$  (figure 2-7) was used, since higher values seemed to remove both the background as well as part of the EXAFS data. For completeness, we show the typically ignored surface oxide in the undoped sample, and thus any resemblance to the Ge-N related spectra in the doped samples is coincidental. “Typically ignored” means that this surface oxide may actually be any number of impurities (plus oxygen), and it’s amplitude is usually just above the background noise level: it usually disappears completely after background subtraction. However, in this case depth profile XPS implies that it is mainly germanium oxide, so we can retain it for fitting. The location of the arrows in figure 2-9 indicated a Ge-N and Ge-N-Ge feature, clearly separate from the amorphous GST structure [70]: the local structure of amorphous GST bonds appeared unperturbed by nitrogen addition.

One must exercise caution in interpreting EXAFS spectra quantitatively, i.e by only considering the magnitude of the FT spectra. The magnitude of the FT *is like a* radial distribution function (RDF) of the atoms about the absorber atom because there is usually a peak corresponding to the first shell of atoms with an  $R$  value related to the interatomic distance. The magnitude of the EXAFS FT *is not* an RDF. First, the peak position in the FT of the EXAFS does not correspond to the distance between the absorbing atom and its neighboring atoms as they do in an RDF for several reasons. First, the shift of the peaks in the FT depends on the identity of both the absorbing atom and the coordinating atom(s),

captured in  $\varphi_i(k)$  in the sine term in the EXAFS (Eqn 2.2). This is seen in figure 2-9, where the first shell bond lengths are shifted to a distance of 1.5Å. Second, MS paths of the photoelectron can produce strong signals in the FT of the EXAFS and are not part of a RDF. Third, unlike an RDF, the interference between two scattering paths of the photoelectron may result in a minimum rather than a peak in the FT of the EXAFS data. Fourth, the amplitude of the peaks in the FT of the EXAFS data depends on many EXAFS variables (Eq. 2.2). For instance,  $\lambda_j(k)$  causes the EXAFS amplitude to diminish with increasing radial distance. The amplitude of a RDF depends only on the coordination number ( $N$ ).

The FT is defined for a spectrum that extends from  $-\infty$  to  $+\infty$ . Since EXAFS data consist of a range from  $k_{min} = 0$  to  $k_{max} \approx 14\text{Å}^{-1} - 17\text{Å}^{-1}$ , zeros are added to the data outside this range to pad the data set from  $-\infty$  to  $+\infty$ . Consequently, there is a discontinuity between the region which defines our data and the values of zero outside the data range, which is essentially a step function. A FT of a step function gives a signal at all R values, which is referred to as a FT ripple or ringing. The FT ripple can obscure the phase and amplitude of scattering shells, for instance, the arrow at  $\sim 3\text{Å}$  in figure 2-9. But we know that this scattering shell is likely real since the FT ripple effect was minimized by multiplying the spectrum by a FT window. A window function gradually brings the data up from zero at the start of spectrum and back down to zero at the end of the spectrum. In this case, we used a Hanning window function [48], and various values of steepness of the transition region to find the ideal case to minimize the FT ripple. The added effect of a window function is that

specific scattering shells of a FT can be isolated for analysis and fitting, however this was not done for any of our data sets.

### 2.5.3 EXAFS Models and Fitting

The similarities between the vibrational spectra and Ge near edge spectra of N-GST versus other amorphous and crystalline germanium nitrides, will direct our models for quantitative EXAFS analysis. The strong absorption in FTIR at  $\sim 700\text{ cm}^{-1}$  is consistent with a Ge-N bonding, where we observed the dominant asymmetric stretching mode associated with the  $\text{Ge}_3\text{N}$  skeletal group. The N atomic configuration,  $1s2s2p_x2p_y2p_z$ , can complete its valence shell by a) electron gain to form the nitride ion  $\text{N}^-$ ; b) strong covalent bonds (single or multiple), like in molecular  $\text{N}_2$ ; c) other covalent bonds from electron gain, as in  $\text{NH}_2^-$ ; d) electron-pair bonds with electron loss, as in tetrahedral ammonium [71].  $\text{NR}_3$  molecules are pyramidal; the bonding involves  $sp^3$  orbitals so that the lone pair occupies the fourth position. Electronic studies of amorphous and crystalline germanium [72] and silicon [73; 74] nitrides reveal that nitrogen bonds to both Ge and Si in a similar, unique, pyramidal configuration which has been described as  $sp^2$  hybridization [75]. In this structure, Ge (or Si) both form distorted tetrahedral covalent bonds via  $sp^3$ - hybridization while N bonding is explained in terms of a linear combination of  $p$  orbitals, given by a strong repulsion of nonbonded Ge / Si atoms by the N lone pair electrons, leading to a planar geometry [76]. These local structural characteristics are the same in both the  $\alpha$  and  $\beta$ - $\text{Ge}_3\text{N}_4$  and amorphous

Ge<sub>(1-x)</sub>N<sub>x</sub> nitrides [62] and main electronic features between amorphous Si and Ge nitrides are the same [72; 77].

Consequently, we used the ATOMS interface in IFEFFIT to generate a list of atomic coordinates about the Ge absorber, based on: A) the distorted tetrahedral unit cell parameters from  $\beta$ -Ge<sub>3</sub>N<sub>4</sub> [63] as well as B) the simple first shell tetrahedral bonded Ge-Ge, Ge-Te, and Ge-Sb. Typically for amorphous samples and mixed systems, it is a known technique in EXAFS modeling to use mixing variables to calculate the bonding fraction of each unique environment [78]. Therefore, we have (Ge-N paths)\*x + (Ge-Ge)\*y +(Ge-Sb)\*z +(Ge-Te)\*(1-x-y-z), where  $0 < x, y, z < 1$ . The ATOMS output is a theoretical FEFF calculation, each with paths which can be arbitrarily chosen for fitting by the user. Once a path has been selected and added for testing, the remaining math expressions for the path variables (from the EXAFS equation) were constrained as follows:

- **$\Delta R$**  – The change in path length was determined independently for each path in the GST environment, ie, Ge-Ge, Ge-Te, and Ge-Sb.  $\Delta R$  values were constrained to be the same for all paths in the Ge-N 1<sup>st</sup> shell, while all Ge-N-Ge paths in the second shell also had one  $\Delta R$  variable .
- **$\sigma^2$**  – Coordination shells with similar atoms and bond distance were constrained to have the same debye waller factors. For instance, all Ge-N-Ge paths, for all data sets utilized just a single  $\sigma^2$  variable.
- **$\Delta E$**  – One energy alignment parameter was needed for each N-GST data set to account for the misalignment of data with the theoretical calculations.

- $N$  – The path degeneracy for the Ge-N and Ge-N-Ge paths were determined from the  $\beta$ - $\text{Ge}_3\text{N}_4$  crystal structure. For the GST related paths, we followed the 8-N rule, and  $N$  was constrained to 4.
- $S_0^2$  – One value of the amplitude reduction factor was used for each sample, and this was restrained to be close to fitted values of known Ge references standards measured at each run, since it is mostly chemically transferable [52]. We set  $S_0^2 = 0.80$  for all N-GST samples.

Each N-GST sample was imported into the Artemis project, creating 4 unique data sets, and multiple data sets (MDS) was employed. MDS is the simultaneous calculation of best fits to the theoretical paths for more than one N-GST sample (data set) at a time. For instance, it was reasonable to assume that the Ge-N and Ge-N-Ge bond lengths were similar for all N-GST Ge environments. We can easily implement this constraint using MDS fitting, to obtain a better measure of the parameterized path parameters and significantly reduce the number of variables that must be determined in our fits, thus improving the statistical significance of the results. Multiple k-weight (MKW) fitting, using  $kw=1, 2, \text{ and } 3$ , was done in all cases. Since different parameters effect different regions of data, MKW allows us to distribute the importance of the evaluation of the chi-square over the entire  $k$  range.

“Fitting” means adjusting the path parameters and mathematical variables to arrive at a least squares fit between the experimental data and the theoretical spectrum. The fitting results include the user defined variables versus their best fit values and their uncertainties, as well as the important statistical parameters such as number of independent points,  $N_{ind}$ , the

number of variables,  $N_{var}$ , which must be less than  $N_{ind}$ , the  $\chi^2$  (chi-square),  $\chi^2_{\nu}$  (reduced chi-square), and the  $\mathcal{R}$  factor. The important considerations of these standard goodness-of-fit statistical parameters for EXAFS analysis are covered in by Stern et al. [79], but the highlights are:

**$\mathcal{R}$  factor** – The  $R$  factor is the sum of the squares of the differences between the data and the fit at each data point, divided by the sum of the squares of the data at each corresponding point. It represents the mean square misfit between the data and the fit for both the real and imaginary parts of the Fourier transform and it is defined as:

$$R = \frac{\sum_i (data_i - fit_i)^2}{\sum_i data_i^2} \quad [\text{Eqn. 2.5}]$$

In general, fits with  $R$  factor values  $\leq 0.05$  are considered reasonably good.

**$\chi^2$**  – The  $\chi^2$  value is the sum of the squares of the difference between the predicted fit and the data divided by the uncertainties ( $\varepsilon$ ) at each data point ( $i$ ). It is calculated as:

$$\chi^2 = \frac{N_{ind}}{N_{pts}} \sum_i \left( \frac{data_i - fit_i}{\varepsilon_i} \right)^2 \quad [\text{Eqn. 2.6}]$$

The sum is over each data point in the real and imaginary parts of the Fourier transform,  $N_{ind}$  is the number of independent points in the model fit, and  $N_{pts}$  is the number of data points.

**$\chi^2_{\nu}$**  – To compare models with different numbers of variables, the  $\chi^2_{\nu}$  values are used. It is the  $\chi^2$  divided by the degrees of freedom in the fit,  $\nu$ . The degrees-of-freedom in the fit is defined as the number of independent points in the measured spectra minus the number of variables fit in the model.

Table 2-3: Final fitting statistical parameters for N-GST samples showing the Fourier transform ranges ( $\Delta k$ ), fitting ranges ( $\Delta R$ ), the R factor for each data set ( $R$ ). The MDS results shown: the number of independent parameters used in the fits ( $N_{ind}$ ), the number of variables ( $N_{var}$ ), the chi-squared ( $\chi^2$ ), the reduced chi-squared ( $\chi^2_v$ ), the R factor, and the measurement uncertainty in R ( $\epsilon$ ).

N at.%	$\Delta k$	$\Delta R$	R	MDS Goodness of Fit Results					
				$N_{ind}$	$N_{var}$	$\chi^2$	$\chi^2_v$	R	$\epsilon$
0%	3.0:15.4	1.0:3.0	0.00389	65.6	33	16901.01	518.47	0.0025	0.0009
2.5%	3.0:14.0	1.0:3.3	0.01334						
5%	3.0:15.4	1.0:3.3	0.00959						
6.1%	3.0:15.4	1.0:3.3	0.01027						

Table 2-4: A summary of the fitting parameters calculated from the fits to the amorphous N-GST samples and their percent errors (the fitting results of undoped GST is shown and discussed in chapter 4). In total, 16 parameters are determined from the three data sets.  $S_0^2$  was 0.8 for all data sets.

	Bond	Bond Env. %			N		$\sigma^2(\text{\AA}^2)$		Energy shift (eV)	R ( $\text{\AA}$ )	
		2.5%	5.0%	6.1%							
Germanium Nitride	Ge-N	32 +/- 7	44 +/- 3	48 +/- 2	2.0 +/-0.25		0.003	+/- 0.001	2.5 at% 4.05 +/- 0.9	1.80	+/- 0.003
	Ge-N				1.0 +/-0.13					1.82	
	Ge-N				1.0 +/-0.13					1.89	
	Ge-N-Ge				2.0 +/-0.25		0.011	+/-0.001		3.08	
	Ge-N-Ge				2.0 +/-0.25					3.18 +/-0.01	
	Ge-N-Ge				4.0 +/-0.50					3.24	
GST	Ge-Ge	68 +/- 8	56 +/- 6	52 +/- 4	0.41 +/-0.1	2.5 at%	0.003	+/-0.001	5.0 at% 4.02 +/- 0.5	2.43	+/-0.01
					0.36 +/-0.2	5.0 at%					
					0.46 +/-0.2	6.1 at%					
	Ge-Sb				1.00 +/-0.3	2.5 at%	0.003	+/-0.001		6.1 at% 4.15 +/- 0.4	2.71
					0.79 +/-0.2	5.0 at%					
					0.69 +/-0.2	6.1 at%					
	Ge-Te				2.59 +/-0.5	2.5 at%	0.003	+/-0.001			2.60
					2.86 +/-0.6	5.0 at%					
2.85 +/-0.6		6.1 at%									

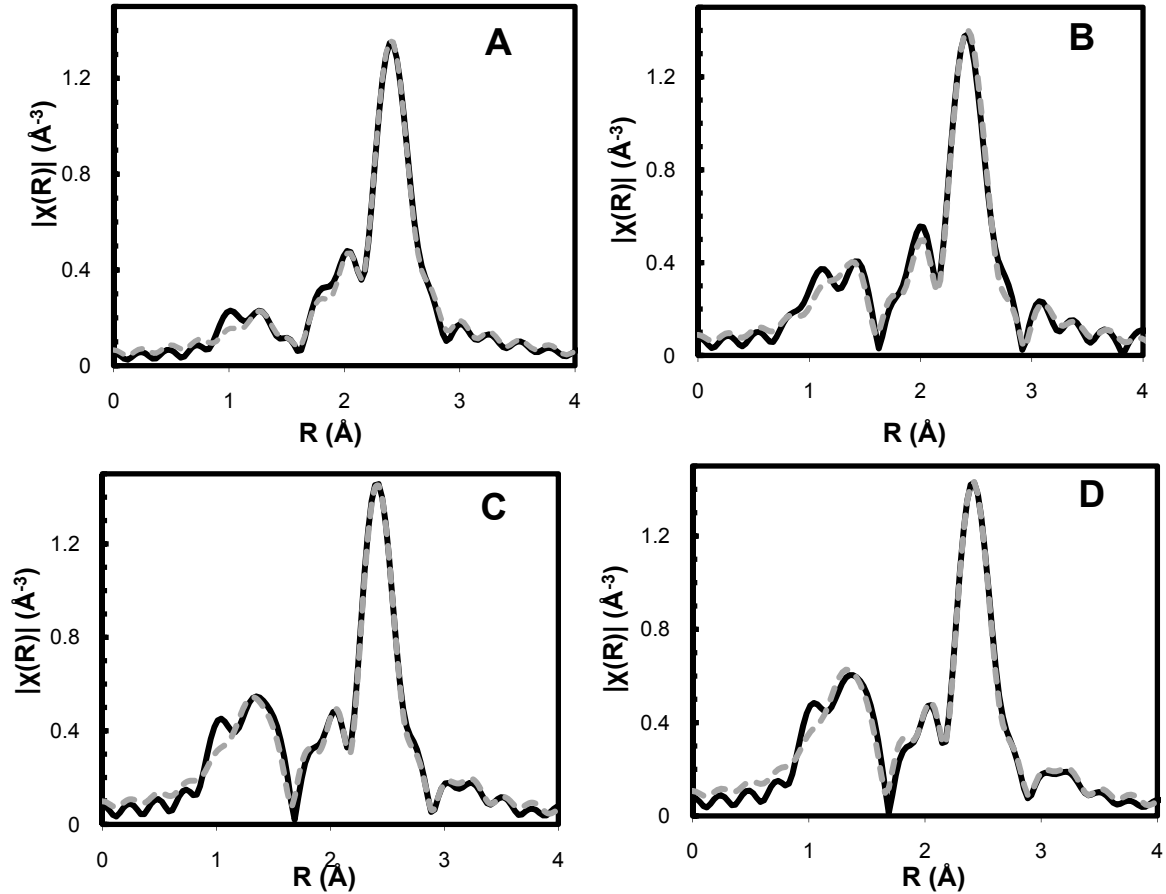


Figure 2-10: (A-D): Fits to the Ge K edge as-deposited N-GST data for A) GST, B) 2.5%N-GST, C) 5%N-GST, and D) 6.1%N-GST. Magnitude of the complex Fourier transformed of EXAFS spectra is shown. The solid black line is the data, and gray dash line is the fits.

We present the resultant goodness-of-fit parameters in table 2-3 and fits are shown in figure 2-10. Table 2-4 shows the results of the fitting parameters for only the doped N-GST samples (B, C, and D above). The fitting model resulted in our lowest reduced chi-squared ( $\chi^2_v$ ), the R factor, and the measurement uncertainty in R ( $\epsilon$ ), with very good fits to the data. The R and  $\sigma^2$  found for the Ge-N and Ge-N-Ge paths were similar to previously observed results for a-Ge<sub>(1-x)</sub>N<sub>x</sub> [62] with negligible uncertainties. The calculated R and  $\sigma^2$  of Ge-Te and Ge-Sb are consistent with previously fitted results for as-deposited germanium telluride

and germanium antimony references, as well as covalent bond distances in literature. The Ge-Ge bond distance was shorter than those observed in the undoped GST sample (2.47Å). It was previously shown that Ge-Ge bonding is inherent to GST and GeTe films [80], with Ge-Ge bond lengths of ~2.47Å for ...-Te-Ge-Ge-Te-... structures. In fact, the observed Ge-Ge bond distance in amorphous  $\text{Ge}_{(1-x)}\text{N}_x$  was consistently close to 2.44Å [62], implying that homopolar Ge-Ge bonds in N-GST are found in ...-N-Ge-Ge-N-... structures.

The percent error of bond fraction and coordination environment was noticeable higher for the 2.5% N-GST sample, due to the higher random noise in that data set. As expected, the germanium nitride bond environment fraction increased as the N at. % increased, accounting for 32%, 44% and 48% of the Ge environment of 2.5, 5, and 6.1%N-GST, respectively. The total bonding fraction of Ge-Te, Ge-Sb, and Ge-Ge contributions decreased as more germanium nitride was formed. We noticed that the number of Ge-Sb bonds decreased proportionally to an increasing number of Ge-Te bonds, as N at% increased.

The observed Ge-N-Ge bonding in our EXAFS models indicates that the nitride is a separate phase, in which N always bonds to 3 Ge neighbors inducing local chemical ordering. This was seen previously in as-deposited  $\text{Si}_{(1-x)}\text{N}_x\cdot\text{H}$  [81] and  $\text{Ge}_{(1-x)}\text{N}_x\cdot\text{H}$  [62] films where preferential N-Si or N-Ge bonding led to the films being characterized as totally chemically order networks (TCON) [82]. Preferential Ge-N bonding in the N-GST local structure, in the limit where all N is bonded to three Ge neighbors, is consistent with the FTIR and XPS data. This N environment is characterized by strong repulsions from non-bonded Ge, due to interactions between the N lone pair  $p\pi$  orbital and the next nearest neighbors. In N-GST,

these repulsions are equally likely, and may involve interactions with Te next nearest neighbors. This, together with the resulting planar N local structure, and the strong Ge-N covalent bonding, are likely the main driving forces behind the observed grain size reduction and refinement in annealed N-GST films. Studies showed that N doping lead to roughly spherical crystallites, accompanied by dramatic reduction (and restriction) of the average grain size to ~20nm for 2.9% N content and ~10nm for 6.9% N content, even after prolonged annealing [19].

## 2.6 *In-situ* Time Resolved XRD of N-GST

The strong covalent Ge-N bonds in both amorphous  $\text{Ge}_{(1-x)}\text{N}_x$  and  $\beta\text{-Ge}_3\text{N}_4$ , are thermally stable over the range of annealing temperatures [83], and are therefore expected to persist post anneal. Undoped GST, 2.5%, 5%, and 6.1% N-GST 100nm thin film samples were RF sputter-deposited on bare Si wafer. *In-situ*, time-resolved, XRD experiments were performed by Simone Raoux and Jean Jordan-Sweet at beamline X-20C of the National Synchrotron Light Source using a photon energy of 6.9keV. The setup consisted of a high-throughput synthetic multilayer monochromator and fast linear-diode-array detector [84; 85]. A special chamber for controlling the sample ambient (purified He gas) was outfitted with a BN heater for rapid annealing up to 1200°C at  $\leq 35^\circ\text{C}/\text{sec}$  [86; 87]. For blanket films, resistivity was also measured simultaneously using a 4-point probe in square geometry. In figure 2-11, the appearance of XRD peaks assigned to the FCC rocksalt phase of GST occurs at 175°C while this transition shifts to higher temperatures with increasing N content. This

transition is relatively sharp and clear for the undoped film, while for the nitrogen doped films, the transitions are less sharp and extend over a larger temperature range. The crystallization temperatures (marked by solid gray lines) were calculated by integrating over the intensity of the most intense diffraction peak for each phase and calculating the maximum of the derivative. The rocksalt peaks at  $2\theta = 29.2^\circ$  and  $33.8^\circ$  can be identified as the NaCl cubic phase (111) and (200) with a lattice constant of a  $\sim 0.618$  nm. The samples in figure 2-11 were ramped to  $450^\circ\text{C}$  and quenched.

Similar 100nm N-GST films on bare Si (with slightly higher N at. %) were previously studied by Shelby and Raoux via *in-situ* time resolved XRD measurements described below, in addition to normalized laser reflectivity and AFM measurements [88]. Their study showed that increased nitrogen concentration, lead to increased rocksalt and hexagonal crystallization temperatures and more gradual transitions as observed in XRD. Their study concluded that nitrogen doping hinders nucleation, and slows down crystallization. Our *in-situ* time resolved XRD measurements are also in agreement with previous XRD studies of GST [89], in which all peaks were assigned to the FCC NaCl rocksalt crystal lattice. In rocksalt, the Na and Cl form a face-centered cubic lattice, respectively, and they are shifted mutually by a  $\frac{1}{2}$  of the lattice in the  $x$ ,  $y$ , or  $z$  direction, forming a nesting structure [90]. XRD studies by T. Nonaka et al. showed that GST annealed (or laser crystallized) over FCC transition temperatures, will have Ge and Sb atoms randomly occupy the 4(b) site in this  $Fm-3m$  crystal structure, together with approximately 20 at.% vacancies, while the 4(a) site was occupied by Te atoms only [91].

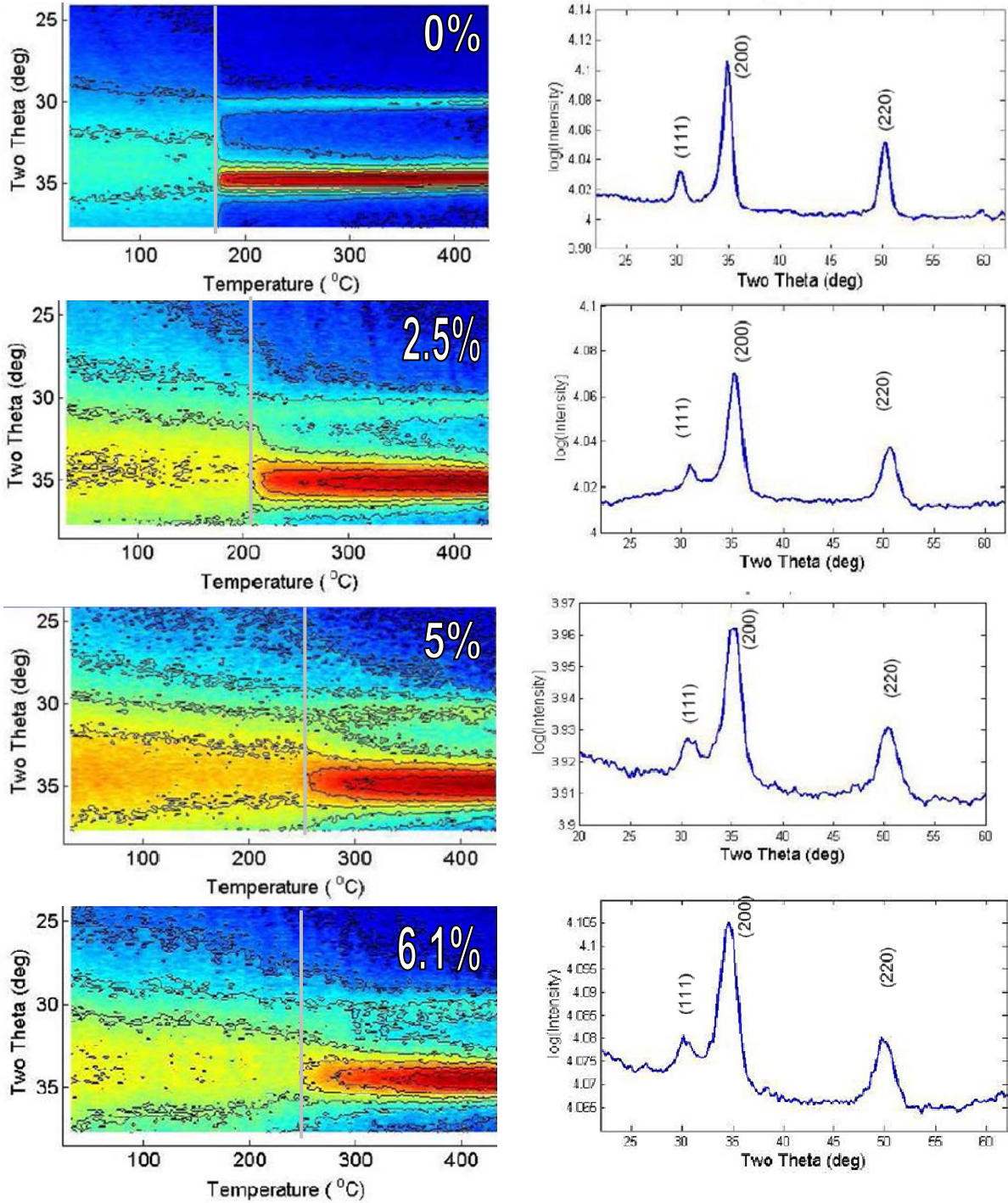


Figure 2-11: Intensity of diffracted x-ray peaks is plotted vs diffraction angle ( $2\theta$ ) over a range of  $15^\circ$  (vertical axis) vs temperature (horizontal axis) for blanket films of GST and 5%N-GST heated at a rate of  $1^\circ\text{C/s}$ . This is shown alongside the Intensity vs ( $2\theta$ ) which was taken at  $450^\circ\text{C}$ . Transitions to the crystalline rocksalt phase are marked by vertical solid gray lines, corresponding to  $175^\circ\text{C}$ ,  $215^\circ\text{C}$ ,  $250^\circ\text{C}$ , and  $250^\circ\text{C}$  for 0%, 2.5%, 5%, and 6.1%N-GST, respectively. The cubic peak indices are shown.

## 2.7 XAFS of 5%N-GST versus Anneal Condition

Additional information on the structural role of the dopant during crystallization was obtained from XAFS of N-GST vs anneal condition. 5%N-GST films of differing anneal conditions were studied: a 100nm film on Si, annealed in the deposition chamber to 250°C for 10 minutes, a 1000nm film on glass, annealed in a tube furnace at 300 °C for 30 minutes, and a 100nm film on Si, ramped to 250°C (and quenched) on the time resolved in-situ XRD apparatus. Florescence measurements were performed at the Ge K edge in similar fashion to the amorphous N-GST samples in section 2.5, and followed similar normalization, background removal, and XANES analysis. The background removal parameters are shown in table 2-5. Figure 2-12 shows a direct comparison of the normalized Ge near edge absorption for the as-deposited, XRD 250°C Ramp / quenched, the 250°C 10 minute annealed, and 300°C 30 minute furnace annealed samples (for the remainder of this section, we call these AS\_DEP, 250C\_RAMP, 250C\_10MIN, and 300C\_30MIN). Similarly, figure 2-13 compares the EXAFS, and figure 2-14 shows the magnitude of the complex Fourier transform for these samples.

Table 2-5: Background removal quantities used in AUTOBK for Ge K edge N-GST crystallized samples. The  $E_0$  values is not shown since all samples were aligned to a common  $E_0$  of ~11097eV.

Sample	$\Delta k$ ( $\text{\AA}^{-1}$ )	$R_{\text{bkg}}$ ( $\text{\AA}$ )	Pre-Edge	Post-Edge
AS_DEP	[0.0 : 15.05]	1.0	[-197.1 : - 6.5]	[100 : 862.11]
250C_RAMP	[0.0 : 15.05]	1.0	[-197.1 : -86.5]	[100 : 862.11]
250C_10MIN	[0.0 : 15.05]	1.0	[-197.1 : -86.5]	[100 : 862.11]
300C_30MIN	[0.0 : 16.17]	1.0	[-197.1 : -86.5]	[79.42 : 994]

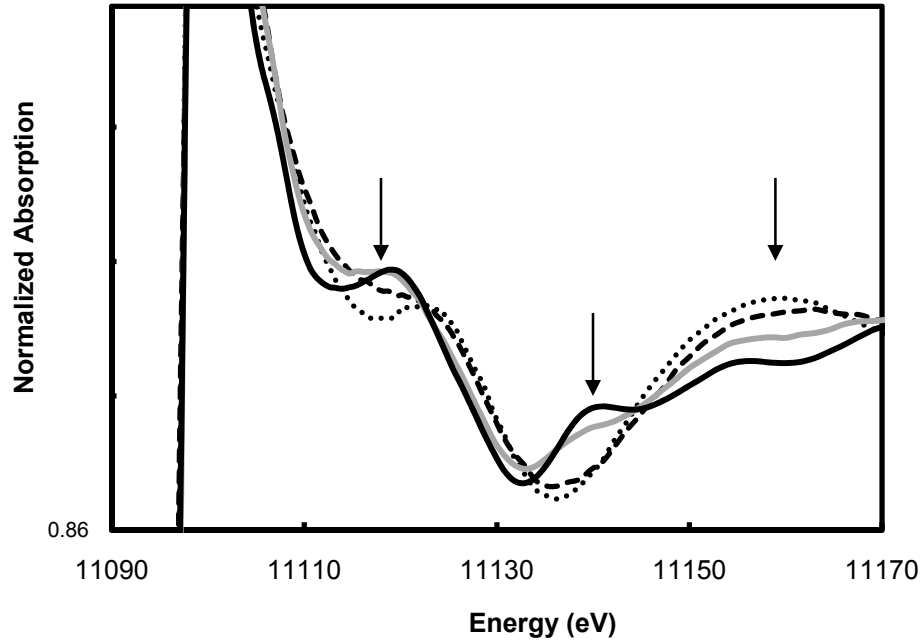


Figure 2-12: Normalized Ge near edge comparison of AS\_DEP (black dotted line), 250C\_RAMP (black dashed line), 250C\_10MIN (gray solid line), and 300C\_30MIN (black solid line). Arrows indicate the appearance of sharp features relating the long range order in GST

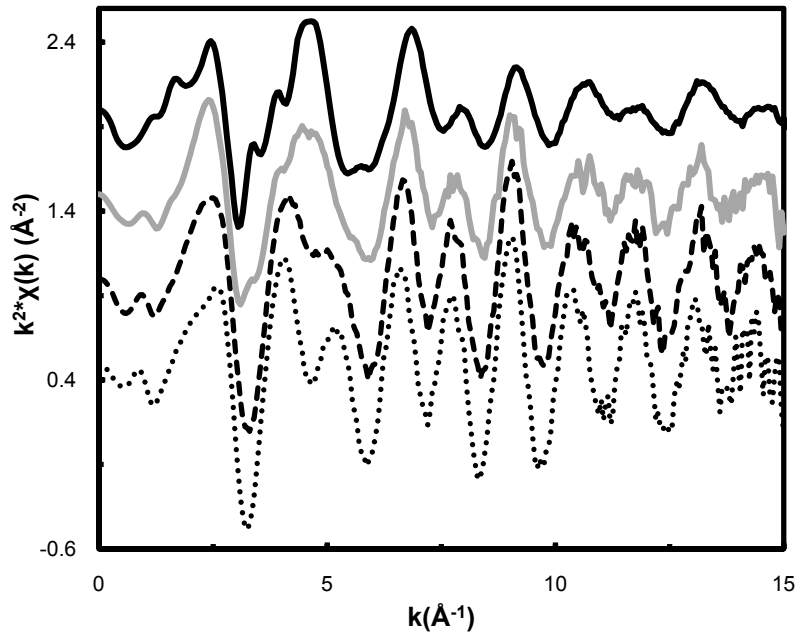


Figure 2-13:  $\chi(k)$  extracted from the  $\mu(E)$  of AS\_DEP (black dotted line), 250C\_RAMP (black dashed line), 250C\_10MIN (gray solid line), and 300C\_30MIN (black solid line), using the AUTOBK program. Each spectrum is the average of at least four fluorescence measurements.

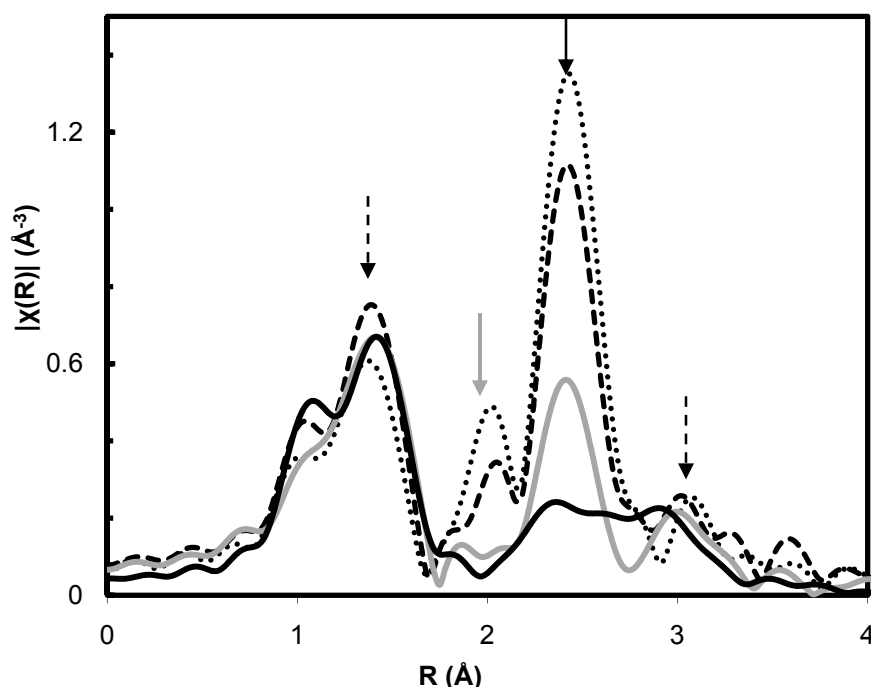


Figure 2-14: Magnitude of Fourier transformed EXAFS spectra AS\_DEP (black dotted line), 250C\_RAMP (black dashed line), 250C\_10MIN (gray solid line), and 300C\_30MIN (black solid line), using  $\Delta k = 3-15\text{\AA}$

The new features at the near edge indicated by the solid arrows in figure 2-12 become sharper and scale in intensity with annealing. These are new multiple scattering states, related to the GST rocksalt structure and grain growth. An interesting future study may consider the relationship between the fraction of crystallites in N-GST and the intensity of these near edge features. In the magnitude of the FT shown in figure 2-14, some interesting inferences were drawn. We noted that the amplitude of the main amorphous GST contribution (tetrahedral Ge-Te bonding), marked by the solid black arrow, decreased as anneal duration and temperature increased, while the region in the FT corresponding to Ge-Ge bonding in amorphous GST, completely disappears as crystallization progresses (solid gray arrow). As

the majority of Ge absorbers phase change from amorphous tetrahedral bonding to the FCC crystalline local structure, we expect the intensity of the amorphous bond distribution to decrease, although the abrupt decline in Ge-Ge bonds after a 250°C anneal and implies a breaking of the ...-N-Ge--Ge-N-... bonding structures. On the other hand, the germanium nitride environment (1<sup>st</sup> Ge-N shell and multiple scattering Ge-N-Ge shell) is mainly unchanged by anneal time and duration (dashed arrows). This is consistent with our expectations that the local structure of germanium nitride in N-GST is a thermally stable, separate phase as we previously reported [92]. The slight changes in amplitude of the Ge-N first shell cannot be treated quantitatively: as the near edge region of each sample becomes increasingly complex with crystallization (figure 2-12), so does the difficulty in defining an appropriate  $R_{\text{bkg}}$  value to separate the Ge-N features from background.

The apparent location of the crystalline feature apparently overlaps the region of R space also occupied by Ge-N-Ge. Yet, it is also clear that the amplitude of the crystalline contribution is not increasing in proportion to the decrease in the amorphous component. In this case, the amplitude of the EXAFS (eqn. 2.2), is reduced by the  $\frac{1}{r_j^2}$  term, since XRD estimates the Ge-Te nearest neighbor distance in the FCC lattice at  $\sim 3.0\text{\AA}$  (versus 2.59 for tetrahedral Ge-Te bonds). The amplitude is further modified by  $e^{-2\sigma_j^2 k^2}$  term in the EXAFS, where the local disorder in the Ge environment and the resulting high  $\sigma_j^2$  reported by others, leads to much lower amplitudes than those observed in the amorphous environment.

## 2.8 Crystallization of 5%N-GST in XRD vs EXAFS

Interestingly, the 250C\_RAMP sample is predicted crystalline due to the appearance of peaks in the XRD, but EXAFS data in figure 2-14 shows that its amorphous environment is quite significant, albeit with a noticeable drop in amplitude. Crystallization in GST proceeds via critical nucleation, where small unstable clusters of the new phase are formed as we approach the critical temperature. Park et al observed this in HR-TEM, where GST thin films, *in-situ* annealed to 110°C showed 20Å (less than 4 unit cells) grains preceding the formation of larger clusters at higher temperatures [93]. Eventually grains grow to a critical size beyond which they are stable – they grow rather than dissolve. The classical nucleation theory derived by Turnbull and Fisher [94] using the Becker–Doring formalism [95] assumes that formation of grains requires a free energy,  $\Delta G$ , given by

$$\Delta G = 4\pi r^2 \sigma - n\Delta g \quad [\text{Eqn. 2.7}]$$

where  $\sigma$  is the interfacial energy density between amorphous and crystalline phases and  $r$  is the cluster radius. It has been assumed that clusters are of spherical shape, such that the relation between cluster radius and number ( $n$ ) of GST molecules (monomers) in the cluster is,

$$n = \frac{4}{3} \pi \frac{r^3}{v^m} \quad [\text{Eqn. 2.8}]$$

where  $v^m$  is the volume of a monomer, which can be easily estimated from the density and the molar weight of the material ( $v^m = 2.9 \times 10^{-22} \text{cm}^3$ ).  $\Delta g$  in eqn. 2.7 is the bulk free energy difference per GST molecule between the two phases and can be calculated using

the approximation proposed by Singh and Holz [96]. Eqn. 2.7 shows that free energy decreases in proportion to the volume of the cluster but increases in proportion to the area of its interface with surrounding amorphous material. Thus, below a certain critical size, the overall energy increases with cluster size, and above the critical size it decreases. The steady-state rate of nucleation of crystalline GST clusters is the number of newly formed nuclei per unit time and volume, as the free energy approaches its critical limit (i.e. the barrier to nucleation) [97]. Senkader and Wright modeled the steady-state nucleation rate of crystalline GST clusters of critical size, as a function of temperature, shown in figure 2-15 [98].

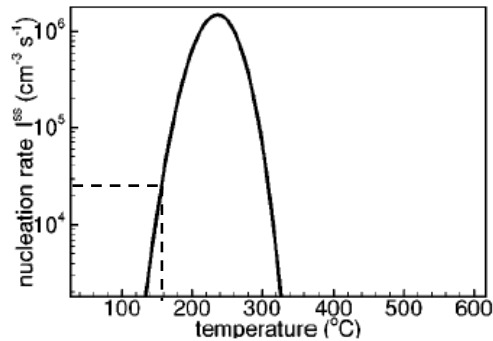


Figure 2-15: The steady state nucleation rate [97] of GST as a function of time, reaches a maximum at about 250°C. The dashed line corresponds to the amorphous to FCC crystalline transition temperature for GST sample as observed in *in-situ* XRD in figure 2-11. (Republished from [98] © JAP 2004)

The dashed line in figure 2-15 which corresponds to the 175°C FCC crystallization temperature for our GST sample observed during ramping in the *in-situ* XRD apparatus, similarly corresponds to low steady state nucleation rate of critical clusters. This could indicate a crude relationship between the modeled nucleation rate and the *in-situ* time resolved measurements for N-GST films: the appearance of diffraction spectra corresponds to relatively low steady state nucleation rates, and by extension, low concentrations of critical sized grains. This might explain the high amorphous contribution in the EXAFS of the

250C\_RAMP EXAFS sample, which was ramped and quenched as soon as XRD peaks appeared at 250°C. Although this sample was crystalline via XRD, it likely consisted of a low fraction of critical sized grains. Furthermore, the relationship above does not take into account the Ge-N environment, which may additionally lower the nucleation rate. The 250C\_10MIN sample EXAFS has a further attenuated amorphous GST contribution, implying that there are considerably more critical sized nuclei, while the 300C\_30MIN sample is likely comprised of the germanium nitride environment + the FCC GST grains.

### **2.8.1 EXAFS Data Analysis and Fitting**

Both the 250C\_RAMP and 250C\_10MIN samples were modeled as a mixture of three distinct environments: an amorphous GST contribution, consisting of tetrahedral Ge-Te bonds; a germanium nitride environment, as found in the amorphous N-GST samples; and, crystalline GST environment, created from a distorted NaCl rocksalt unit cell. The characteristics of each of these environments are:

**Amorphous GST** – Only 4-fold, tetrahedral Ge-Te bonds were used to represent the amorphous GST matrix since we did not expect the Ge-Ge and Ge-Sb environments to remain stable after 250°C annealing. Furthermore, in the XRD, there were no peaks associated with crystalline Ge, even after 400°C, as observed with cases of Ge precipitation. The amorphous Ge-Te bond distances and  $\sigma^2$  were varied independently for either sample.

**Germanium Nitride** – The thermal stability of both amorphous and crystalline germanium nitrides meant that we expect no changes of our Ge-N over the range of anneal temperatures.

We used the same structural model from the amorphous N-GST films, and constrained bond distances and  $\sigma^2$  to behave identically in both samples.

**Distorted NaCl Structure** - The 250C\_RAMP *in-situ* XRD data (figure 2-11) is consistent with previous XRD studies by Yamada and Matsunaga which showed that this metastable crystalline structure corresponds to the NaCl-type structural model in the space-group *Fm3-m*. [99]. In this structure, the 4(a) site is wholly occupied by the Te only, and the 4(b) site is randomly occupied by the Ge, Sb, and some vacancies with different probabilities depending on the actual compositions of the GST. EXAFS measurements of laser crystallized GST by Kolobov et al, showed a slightly different structure. It was similar to the rocksalt structure but the Ge, and to a lesser extent Sb, was shifted from the corresponding FCC sites, giving rise to a system of shorter bonds and longer bonds in an overall buckled structure [31]. We modeled the crystalline contribution according to a similar buckled structure in which path parameters were written in terms of the lattice parameters, and distortion term for Ge was included. We did not constrain both the 250C\_RAMP and the 250C\_10MIN samples to have the same changes in lattice parameters and Ge displacement. The resultant goodness-of-fit parameters are shown in table 2-5 while figure 2-16 shows the final data and fits.

Table 2-6: Final fitting statistical parameters for 250C\_RAMP and 250C\_10MIN showing the Fourier transform ranges ( $\Delta k$ ), fitting ranges ( $\Delta R$ ), the R factor for each data set (R). The MDS results shown: the number of independent parameters used in the fits ( $N_{ind}$ ), the number of variables ( $N_{var}$ ), the chi-squared ( $\chi^2$ ), the reduced chi-squared ( $\chi^2_v$ ), the R factor, and the measurement uncertainty in R ( $\epsilon$ ).

Ann.	$\Delta k$	$\Delta R$	R	MDS Goodness of Fit Results					
				$N_{ind}$	$N_{var}$	$\chi^2$	$\chi^2_v$	R	$\epsilon$
RAMP	3.0:15.0	1.1:3.5	0.01759	37.0	20	923.37	54.25	0.0157	0.0010
10MIN	3.0:14.5	1.1:3.5	0.01431						

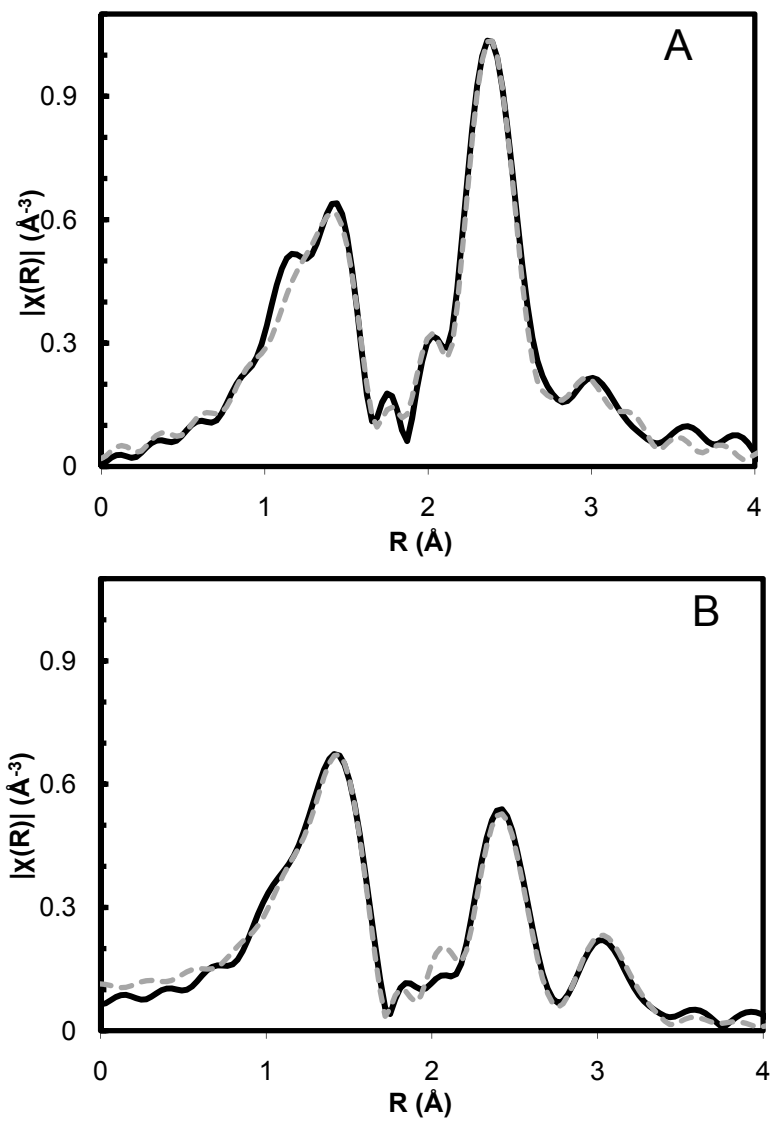


Figure 2-16: Fits to the Ge K edge for (A) 250C\_RAMP and (B) 250C\_10MIN. Magnitude of the complex Fourier transformed of EXAFS spectra is shown. Solid black line = data, gray dashed line = fit.

Table 2-7: A summary of the fitting parameters calculated from the fits to the 250C\_RAMP and 250C\_10MIN samples and their percent errors. In total, 22 parameters are determined from the two data sets.  $S_0^2$  was 0.8 for all data sets.

	Bond	Bond Env. %		N	$\sigma^2(\text{\AA}^2)$	Energy shift (eV)		R (\text{\AA})	
		RAMP	10MIN			RAMP	10MIN	RAMP	10MIN
Germanium Nitride	Ge-N	45 +/- 2	43 +/- 2	2.0 +/-0.25	0.002 +/- 0.001	9.9 +/- 1.0	9.9 +/- 1.0	1.80	+/- 0.003
	Ge-N			1.0 +/-0.13				1.83	
	Ge-N			1.0 +/-0.13				1.90	
	Ge-N-Ge			2.0 +/-0.25				3.10	
	Ge-N-Ge			2.0 +/-0.25				3.20 +/-0.01	
	Ge-N-Ge			4.0 +/-0.50				3.26	
GST	Ge-Te	40 +/- 3	22 +/- 3	4.0 +/-0.50	0.004 +/-0.001			2.59 +/-0.004	
Buckled Rocksalt	Ge-Te (short)	15 +/- 3	35 +/- 3	2.7 +/-1.19 10MIN	0.011 +/-0.004	1.4 +/- 0.78	0.25 +/- 1.47	2.84	+/-0.02
				0.0 +/-0.0 RAMP				3.16	
	Ge-Te (long)			3.3 +/-1.46 10MIN	0.018 +/-0.01			3.16	+/-0.04
				6.0 +/-0.75 RAMP					

The values obtained for the fitting parameters are shown in table 2-7. The bond distances and  $\sigma^2$  of the Ge-N and Ge-N-Ge bonds are at similar distances observed in amorphous N-GST. More significantly, there is negligible change in the fraction of the germanium nitride environment with increased annealing, although this environment was allowed to vary independent of either sample. The reason this fraction is not equal for both samples include: i) there may be increased surface Ge-O oxidation on the 250C\_RAMP sample, and/or ii) the presence of background noise. A separate energy shift variable was defined for all paths in the germanium nitride environment. Using a single  $\Delta E$  variable led to poor fits, specifically, the Ge-N 1<sup>st</sup> shell theory was poorly aligned to the data, and  $\chi^2_v$  as well as measurement uncertainties, increased dramatically. The use of a single  $\Delta E$  is typical, and necessary, to align the k grid of the data with the k grid of the theory. FEFF approximates its scattering phase shifts by constructing spherically symmeterized muffin tin potentials with a flat interstice, which are not calculated self consistently, and do not implement charge

transfer (electrically neutral atomic spheres) [100]. These approximations in the potential model introduce error into the calculation of the phase shift, which in our case can be quite large, unless accounted for by introducing an additional  $\Delta E$  variable to align the theoretical standards to the numerous scattering shells in crystalline N-GST. Although varied independently, the additional  $\Delta E$  variables were consistently close to each other, yet another indication of the similarity in scattering from the nitride environment in both samples.

Unlike the germanium nitride environment, the percentage of tetrahedral Ge-Te bonds at a distance of  $2.59\text{\AA}$  decreased by  $\sim 50\%$  as annealing increased. Varying the coordination number ( $N=4$ ) doubled  $\chi^2_v$  and implied that the amorphous environment at the grain boundary is still similar to the as-deposited sample, i.e. tetrahedral 4 fold covalent bonding. It is possible that the bonds may be slightly shorter - we varied  $\Delta R$  and  $\sigma^2$  independently for the amorphous Ge-Te environment, and observed this improved some fits. High correlations between these additional phase variables and the co-ordination variables (for instance rocksalt bond percent) and with the  $\Delta E$  variables, discredited those results.

As expected, the bonding environment fraction of FCC crystal GST increased from  $\sim 15\%$  to  $\sim 35\%$  after a 10 minute anneal, where the error percentages on these values are consistent with the expected uncertainty surrounding a small fraction of stable, critical sized grains. If we estimate that the fraction of stable germanium nitride environment is  $\sim 44\%$  (from the amorphous and crystalline environment), and assuming that the final grain boundary will be only germanium nitride, then the 250C\_RAMP and 250C\_10MIN sample are roughly 26% and 62% of their maximum crystallization percentage. The crystal

environment was modeled as a variable co-ordination shell consisting of short and long octahedral 6-fold Ge-Te bonds at distances of 2.85Å and 3.16Å. For the fits above,  $\Delta R$  and  $\sigma^2$  for both long and short octahedral Ge-Te paths varied separately, but both sets of variables were constrained to vary similarly in either sample: HR-TEM and XRD indicate that there are no major structural differences between initially formed smaller grains, and large grains formed from continued annealing. The uncertainties in bond distances for the long and short bonds (0.04 and 0.02, respectively), were much higher than those observed in other bonding environments. This is also true for the  $\sigma^2$ , where the error for the uncertainty for the long bond environment implies that  $\sigma^2$  could be as high as 0.03Å, consistent with a large distribution of bond lengths, and significant local structure disorder in the rocksalt Ge-Te environment. When the co-ordination number in either NaCl path was weighed by a fraction variable, in order to determine the percentage of bonds that were short vs long, we observed that there were no short bonds in the 250C\_RAMP while the 250C\_10MIN was almost evenly split between short and long bonds. In these samples, it is clear that the high uncertainties, especially in fits to the R and  $\sigma^2$  within the rocksalt environment, warrant a more detail refinement from the Sb and Te edges in the future. For now, we can conclude on the basis of this data that the fraction of Ge-N and Ge-N-Ge bonds are indeed constant post anneal, and while the amorphous tetrahedral Ge-Te bonds changing phase to a highly distorted structure consisting of long octahedral Ge-Te bonds split between 2.85Å and 3.16Å.

## 2.8.2 The Nature of Crystalline N-GST

Our analysis of the crystal structure of annealed N-GST will conclude with a look at the local structure of 0.0, 2.5, 5.0, and 6.1 at % N-GST films on glass substrates, annealed in a helium ambient using a tube furnace for 30 minutes at 300°C (for the remainder of this chapter, we call these FCC\_GST\*, FCC\_2.5%, FCC\_5.0%, and FCC\_6.1%, respectively). We performed fluorescence measurements at the Ge K edge and followed the similar data processing methods previously discussed. The background removal parameters are shown in table 2-8.

Table 2-8: Background removal quantities used in AUTOBK for Ge K edge N-GST crystallized samples. The  $E_0$  values are not shown since all samples were aligned to a common  $E_0$  of  $\sim 11103\text{eV}$ . The FCC\_0.0% sample was capped with a thin layer of Nb to prevent surface oxidation, so we increased Rbkg to remove to low R background signal. We were unable to collect similar range of data for FCC\_6.1% due to beamline power outage.

Sample	$\Delta k (\text{\AA}^{-1})$	$R_{\text{bkg}} (\text{\AA})$	Pre-Edge	Post-Edge
FCC_0.0%	[0.0 : 15.76]	1.4	[-197.1 : -86.5]	[110 : 946.15]
FCC_2.5%	[0.0 : 16.16]	1.0	[-197.1 : -86.5]	[110 : 989.41]
FCC_5.0%	[0.0 : 16.16]	1.0	[-197.1 : -86.5]	[110 : 989.41]
FCC_6.1%	[0.0 : 11.94]	1.0	[-197.1 : -86.5]	[110 : 533.78]

Previous EXAFS studies of laser crystallized GST films by Kolobov et al at the Ge K edge found two types of bonds: shorter (2.83 Å) and longer (3.2 Å) Ge-Te bonds, which were very similar in distance and distribution to the rhombohedral models of GeTe [101]. They could not reach any definitive conclusions on the long bond, due to high uncertainties. At the Te edge, they noticed that there was a 2<sup>nd</sup> nearest neighbor Te peak at 4.26Å, which was in perfect agreement with XRD. From these results, they proposed a rocksalt structure in which

---

\* The undoped sample was annealed at 200°C for 10 minutes.

Ge and Sb were shifted from their FCC sub-lattice sites giving rise to a system of shorter bonds and longer bonds, where the shorter bonds were more rigid. We observed this similar splitting of short / long bonds in our EXAFS analysis of 250°C anneal 5%N-GST samples above.

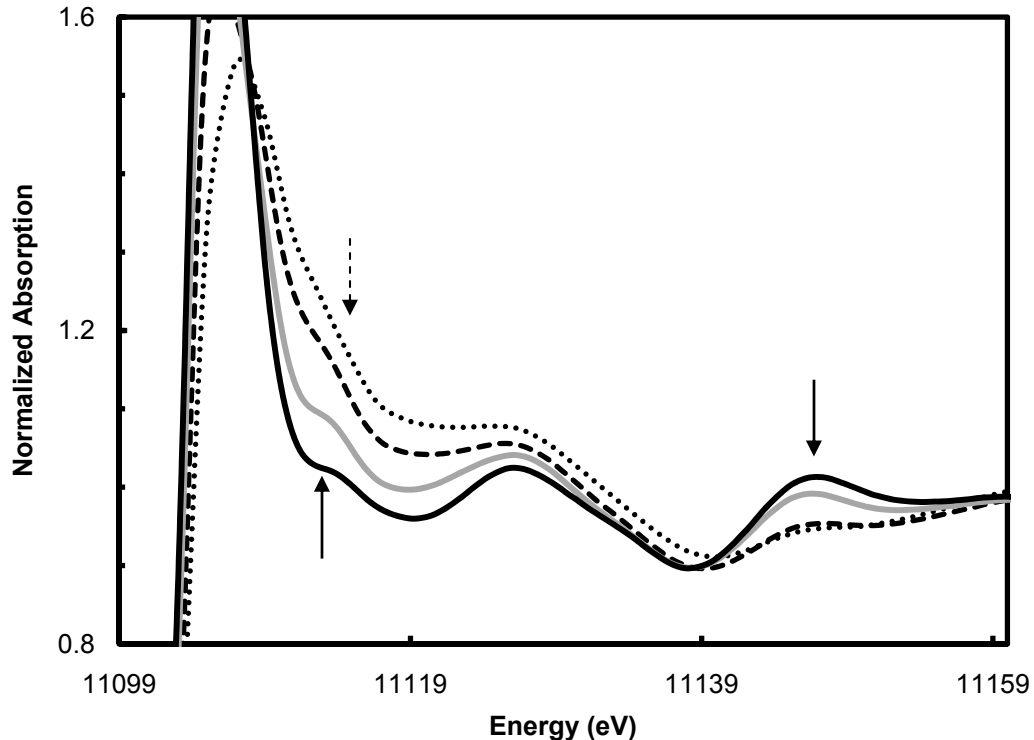


Figure 2-17: Normalized Ge near edge comparison of FCC\_0.0% (solid black line), FCC\_2.5% (gray dashed line), FCC\_5.0% (black dashed line), FCC\_6.1% (black dotted line). The solid black arrow indicates sharp features relating the long range order in GST, while dashed arrow at the near edge indicates the region increasing with N at %.

Figure 2-17 shows a direct comparison of the normalized Ge near edge absorption spectra for FCC\_GST, FCC\_2.5%, FCC\_5.0%, and FCC\_6.1%. After a 300C anneal, we can still see a feature just past the white line relating to the germanium nitride bonds in the system. We also see that the near edge spectrum of the undoped sample has several sharp

features relating the long range order in FCC rocksalt crystalline GST probed by the excited photoelectron. The black arrows indicate that these features are suppressed in the FCC\_5.0% and FCC\_6.1% samples.

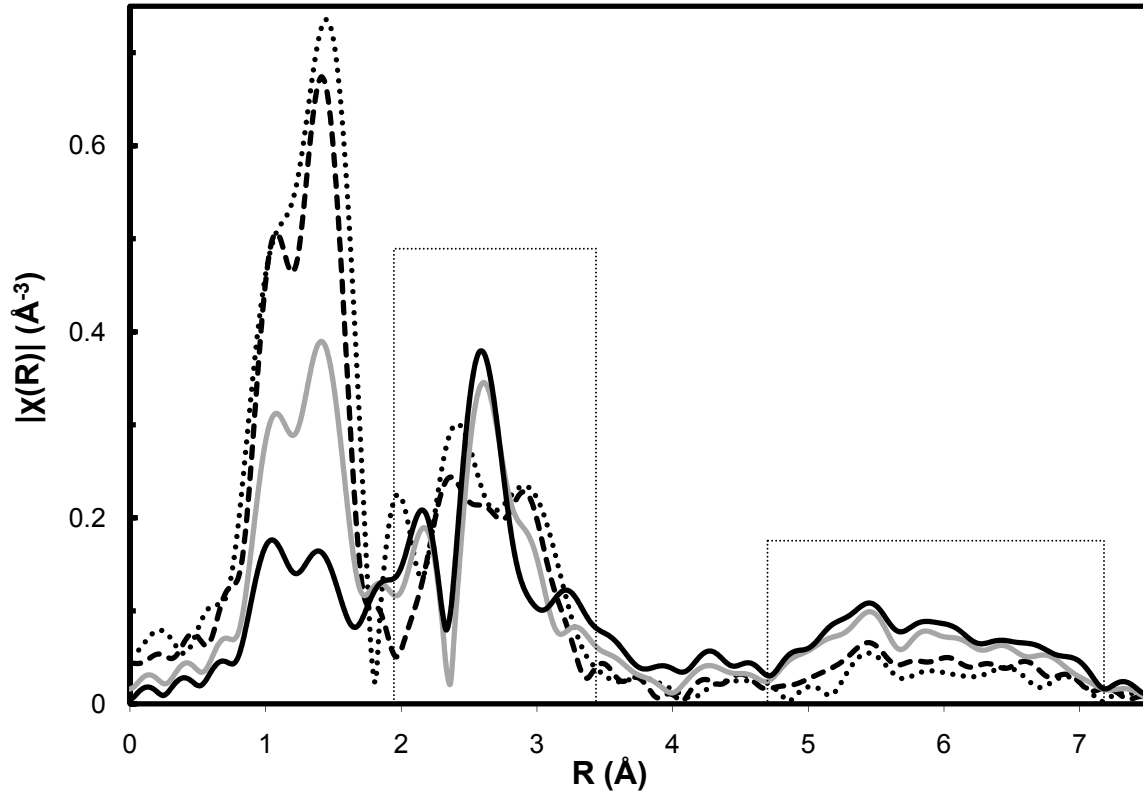


Figure 2-18: Magnitude of the complex Fourier transformed EXAFS spectra of FCC\_0.0% (solid black line), FCC\_2.5% (gray dashed line), FCC\_5.0% (black dashed line), FCC\_6.1% (black dotted line) their respective using  $\Delta k$  values shown in table 2-5. The Ge-N 1<sup>st</sup> shell is clearly distinguishable between 1 - 2Å. The box between 2 – 3.5 Å is crystalline GST first shell, where there is variation between the samples. The box between 5 -7.5 Å is the location of FCC GST multiple scattering contributions. The only variation between samples in this region is a drop in amplitude as N at % increase.

In the  $|\chi(R)|$  data in figure 2-18, we see three separate shells corresponding to a Ge-N first shell, a crystalline GST / Ge-N-Ge second shell, and crystalline GST long range order shell. The drop in intensity as a function of N at % which is more apparent in the region between 5 and 7Å can be a result of termination effects, explained as follows. EXAFS

provides structural information for a region less than a nanometer away from atoms of the element being probed, but there will be measurable size effects (i.e termination effects) if the GST crystallites are less than 10 nm in size, even if the crystal structures are identical. This is because atoms near the boundary of the crystal will be “missing” some of their neighbors, and this will thus lower the average coordination numbers in the sample [102]. Since nearly half of the atoms in a 5 nm radius sphere, for example, lie within 1 nm of the boundary; EXAFS would sense a different environment for these atoms than for those in the interior [103].

Apart from the drop in amplitude, the bond distribution between 5 - 7 Å is the same in all samples, and implies that the increase in N concentration does not lead to substitution of N into the FCC lattice. Nor does it lead to distortion of the FCC lattice. The N dopant instead resides on the grain boundary, where stability and structural nature of Ge-N and Ge-N-Ge bonding refines the grain. As a future study, it would be interesting to model this system as an effective medium consisting of two distinct environments (germanium nitride + GST), with distinct dielectric responses. Appendix 6 contains a few results of our efforts to obtain the dielectric functions of N-GST using spectroscopic ellipsometry.

## Chapter 3 Phase Segregation in binary $\text{Ge}_x\text{Sb}_{(1-x)}$

In searching for alternatives to GST, there has been increased focus on GeSb binary alloys since devices fabricated from these do not suffer the chalcogen related failure mechanisms while also exhibiting improvements in crystallization speed. However, it has been shown that  $\text{Ge}_x\text{Sb}_{(1-x)}$  films suffer from significant phase segregation upon crystallization and cycling. In order to understand the nature of this observed phase segregation, we studied as-deposited and annealed films of  $\text{Ge}_x\text{Sb}_{(1-x)}$  ( $x=0.75, 0.50, 0.25, 0.15, 0.07$ ) using EXAFS to correlate the local structure with previously observed XRD results. We also selected two compositions to which Te was added during deposition:  $\text{Ge}_{15}\text{Sb}_{85}$  and  $\text{Ge}_{50}\text{Sb}_{50}$  in which 10, 20, and 33\* at. % Te was added. We performed a combined XAFS and in-situ, time resolved XRD study on these Te alloyed films, as deposited, and annealed, in order to understand the role of Te in preventing phase segregation and facilitating nucleation.

In section 3.1, we show EXAFS results and analysis for amorphous and annealed  $\text{Ge}_x\text{Sb}_{(1-x)}$ . In 3.2, we analyze the EXAFS local structure of as-deposited films of  $\text{Ge}_{15}\text{Sb}_{85}$  and  $\text{Ge}_{50}\text{Sb}_{50}$  as Te is gradually added to the system. Section 3.3 shows a combined EXAFS and in-situ XRD study of these samples, to gain insight into the Te role in facilitating crystallization and preventing phase separation. In the final section, 3.4, we present our EXAFS results of amorphous as-deposited  $\text{Ge}_2\text{Sb}_2\text{Te}_x$  ( $x=4,5,6,7$ ), and briefly highlight some

---

\* 33 at% Te added to 50:50 sample only

observed correlations between bonding and electronic information contained in the Ge near edge of glasses in the GST ternary system.

All  $\text{Ge}_x\text{Sb}_{(1-x)}$  XAS measurements at the Ge and Sb K edges were performed at the NIST beamline X23A2 [56] at the National Synchrotron Light Source (NSLS), Brookhaven National Laboratory, in Upton, NY. These measurements were done in fluorescence mode, in grazing incidence. The  $\text{Ge}_2\text{Sb}_2\text{Te}_x$  samples were measured at all three edges, at the MRCAT beamline ID-10 [55], at the Advanced Photon Source (APS) at Argonne National Laboratory, in Argonne, IL, using transmission geometry. In-situ, time-resolved, XRD experiments were performed by Simone Raoux and Jean Jordan-Sweet at beamline X-20C of the National Synchrotron Light Source using a photon energy of 6.9keV, with the experimental setup discussed in section 2.3.1.

### 3.1 $\text{Ge}_x\text{Sb}_{(1-x)}$ EXAFS studies

Thin films of the  $\text{Ge}_x\text{Sb}_{(1-x)}$  PCMs were deposited on bare Si wafers via co-sputtering from elemental targets with Ge:Sb ratios of 0.75, 0.50, 0.25, 0.15, 0.07, as determined by Rutherford Backscattering Spectrometry (RBS). The composition was varied by changing the relative powers of the Ge and Sb sputter sources. Samples were cleaved and annealed in a tube furnace at 400°C under a helium ambient for 30 minutes. Ge and Sb K edge measurements were performed before and after annealing and we followed similar data processing methods as previously discussed. We will use a convention of referring to samples in this section by their ratios of Ge:Sb (e.g ‘ $\text{Ge}_{50}\text{Sb}_{50}$ ’ is ‘50:50’).

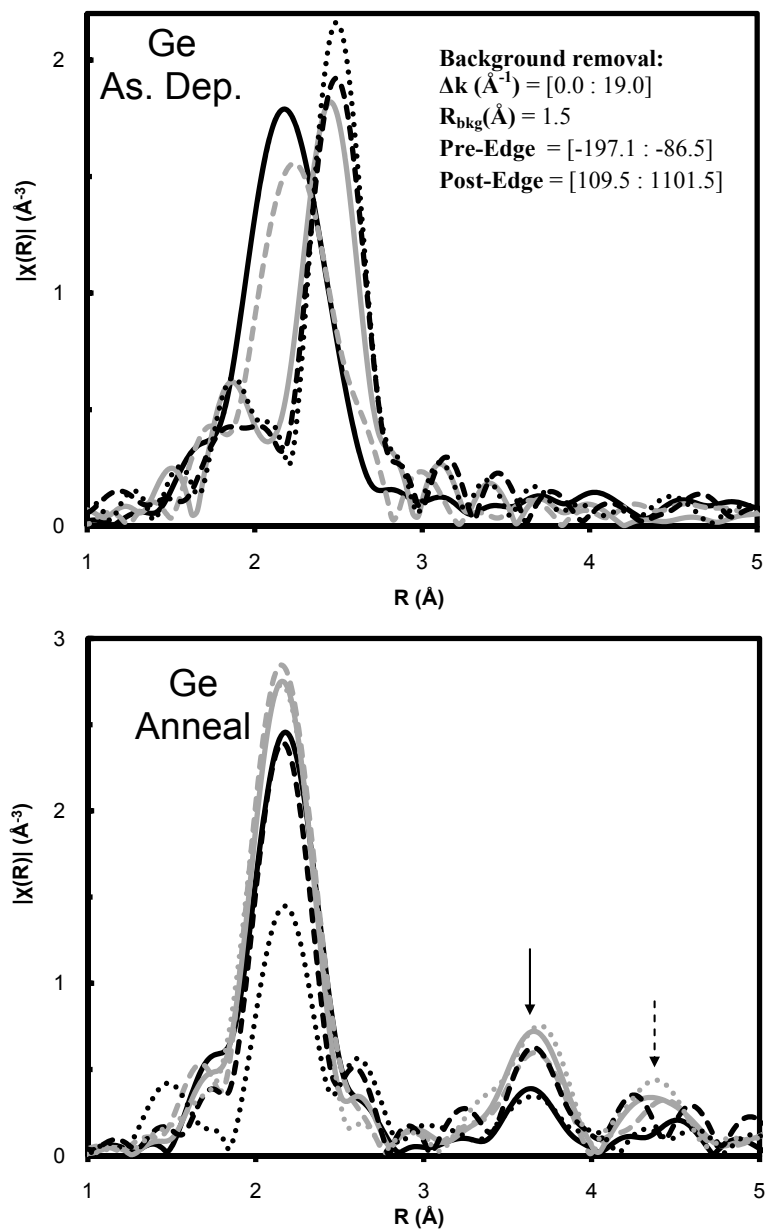


Figure 3-1: Comparison of the magnitude of the complex FT of the Ge K edge EXAFS for as deposited (top) and the 400°C annealed (bottom) 75:25 (solid black line), 50:50 (dash gray line), 25:75 (solid gray line), 15:85 (black dashed line), 7:93 (black dotted line), and Ge metal foil (gray dotted line). Background removal quantities used in AUTOBK for both amorphous and annealed  $\text{Ge}_x\text{Sb}_{(1-x)}$  samples are shown in the inset. The  $E_0$  values are not shown since all samples were aligned to a common  $E_0$  of  $\sim 11102\text{eV}$  for Ge analysis.

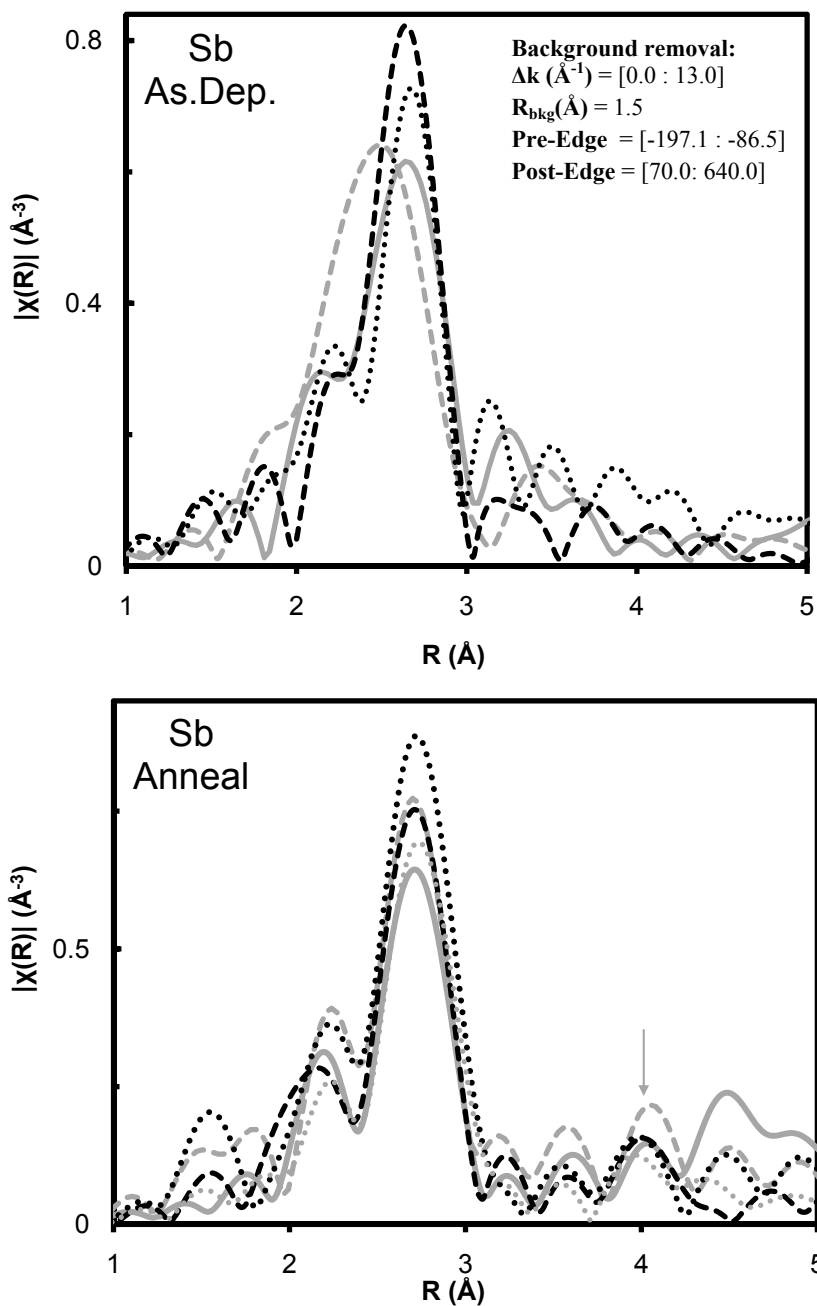


Figure 3-2: Comparison of the magnitude of the complex FT of the Sb K edge EXAFS for as deposited (top) and the 400°C annealed (bottom) 50:50 (dash gray line), 25:75 (solid gray line), 15:85 (black dashed line), 7:93 (black dotted line), and Sb metal foil (gray dotted line). Background removal quantities used in AUTOBK for both amorphous and annealed Ge<sub>x</sub>Sb<sub>(1-x)</sub>Sb edges are shown in the inset. The  $E_0$  values are not shown since all samples were aligned to a common  $E_0$  of  $\sim 30491$  eV for Sb analysis.

The Ge and Sb K edge magnitude of the complex Fourier transform (FT) EXAFS data for the as-deposited and 400°C annealed samples are shown in figures 3-1 and 3-2, along with the parameters used for data normalization. We see a clear dependence of bond distances on the Ge:Sb ratio as the Ge-Sb bond fraction changes with composition. This *pseudo*-radial distribution function is consistent with changes in the fractions of short Ge-Ge bonds to longer Ge-Sb bonds. Phase shifts in the magnitude of the FT depend on changes to the phase of the scattered photoelectron, and consequently, the  $\sin(2kr_j + \vartheta_{oj}(k))$  term in the EXAFS equation (eqn. 2.2). The structure after a 400°C anneal is quite different. We noticed that the bond distribution of all the samples were the same at the Ge edge, following a similar distribution as the EXAFS of Ge metal foil. At the Sb edge, annealed samples followed a similar distribution as Sb metal foil, except for 75:25, which had much lower signal:noise ratio as compared to the other Sb edge data. For this reason, the Sb 75:25 data not shown; they should be re-measured for future analysis. Overall, the bond distribution of the annealed samples is similar to previously observed EXAFS measurements of 13:87 and 49:51 films, showing a Ge crystal local structure post-anneal, and an Sb rhombohedral crystal phase in XRD [104].

Ge has on average four valence electrons per atom and as a consequence,  $sp^3$ -hybridization and tetrahedral covalent bonding is most favorable [105]. It would be consistent to model the local structure of Ge in the amorphous samples as a mixture of tetrahedrally bonded covalent Ge-Ge and Ge-Sb bonds. On the other hand, Sb has the electron configuration  $[Kr]4d^{10}5s^25p^3$ , which explains the stability of oxidation states Sb(III)

and Sb(V) in various Sb oxides [106]. Sb(III) atoms are characterized by a  $5s^2$  lone pair, which does not take part in bonding but whose properties are directly correlated to the Sb coordination polyhedron – three bonds point away from the lone pair, forming a trigonal, pyramidal configuration [107]. Other the hand, Sb(V) is forms a octahedral structure, bonding to 6 oxygen atoms, in line with the symmetric  $4d^{10}$  electron configuration [106; 108]. Discerning the coordination environment of 3-fold Sb(III) and 6-fold Sb(V) is one of the strengths of a XAFS analysis. In Ge-Sb-Te compounds, there is strong evidence that the local structure of Sb in the amorphous phase is trigonal pyramidal from previous EXAFS [70; 109], and follows the 8-N rule of covalent bonding [110]. Reverse Monte Carlo simulations which incorporated results from XRD, EXAFS, and nuclear diffraction converged when a significant concentration of this type of Sb-Ge bond is included in the amorphous phase [111]. Nuclear magnetic resonance (NMR) experiments, which compared the values of measured quadrupole coupling constants ( $\nu_q$ ) for compounds containing Sb bonded in various configurations, found that  $\nu_q$  was extremely sensitive to coordination number and bond distance. They showed that the local structure of Sb in amorphous  $\text{Ge}_2\text{Sb}_2\text{Te}_x$  ( $x=4, 5$ ) and  $\text{Ge}_1\text{Sb}_2\text{Te}_4$  obeyed the 8-N rule, and corresponded to the 3-fold, trigonal pyramidal structure of  $\text{Sb}_2\text{O}_3$ ,  $\text{SbF}_3$ ,  $\text{Sb}_2\text{Se}_3$ , and  $\text{Sb}_2\text{S}_3$  [112]. It is consistent for the Sb local structure of as-deposited,  $\text{Ge}_x\text{Sb}_{(1-x)}$  compounds to follow the 8-N rule, with a pyramidal bonding arrangement consisting of Sb-Ge and Sb-Sb bonds. Figure 3-3 shows the basic structural motifs of Ge and Sb in the as-deposited GeSb and GeSbTe systems.

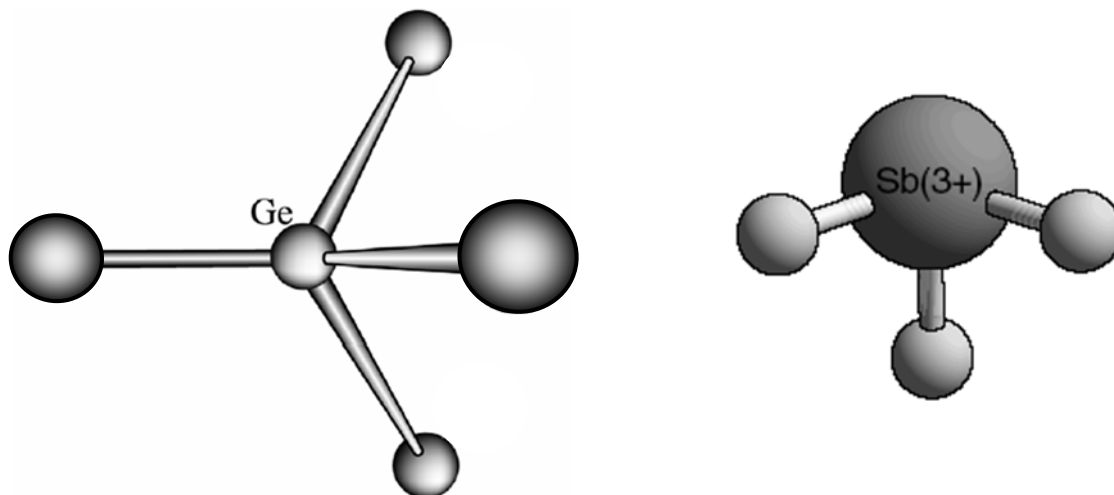


Figure 3-3: Basic structural models for tetrahedrally bonded Ge and trigonal pyramidal coordinated Sb.

### 3.1.1 $\text{Ge}_x\text{Sb}_{(1-x)}$ EXAFS Fits and Modeling

We modeled the Ge edge of the as-deposited films as a mixture of 4-fold, tetrahedral coordinated Ge-Ge and Ge-Sb bonds, i.e.  $(\text{Ge-Ge})_x + (\text{Ge-Sb})_{(1-x)}$ , where  $x$  was a determinable mixing fraction of bonds in each coordination environment. At the Sb edge, we modeled Sb-Sb and Sb-Ge bonds using a 3-fold, trigonal, pyramidal model with similar mixing scheme to determine the fraction of bonds in each environment, i.e.  $(\text{Sb-Sb})_y + (\text{Sb-Ge})_{(1-y)}$ , where  $y$  is to be determined. Both edges were restrained to obey the 8-N rule, so the total coordination at the Ge and Sb edge was 4 and 3 respectively.

For the annealed films, the Ge edge was best simulated using the theoretical paths generated from the unit cell parameters of the Ge diamond-like structure (space group  $Fd\bar{3}m$ ,  $a=b=c=5.65750\text{\AA}$ ,  $\alpha=\beta=\gamma=90^\circ$ ; Ge at 0.125, 0.125, 0.125). For 15:85 and 07:93, the first coordination shell still contained a variable mixture of Ge-Sb bonds as in the as-deposited

films. This can be interpreted as a small fraction of Ge-Sb bonding at the grain boundary. These Ge-Sb bonds accounted for only a small fraction of the first coordination shell. In our models, we obtained fits for path contributions out to the third shell in our samples 75:25, 50:50, 25:75, (indicated by a dashed black arrow in fig. 3-1) but only out to the second shell distance in 15:85, and 7:93 (solid black arrow). At the Sb edge of the annealed samples, there was significantly more noise, and a smaller usable data range ( $\Delta k = 0.0 - 13.0 \text{ \AA}^{-1}$ ). This prevented fits to the Sb-Ge contribution observed at the Ge edge of the 15:85 and 07:93 samples, due to high uncertainties in the estimated Sb-Ge bond fraction. We were able to model all annealed samples using the Sb As-A7 crystal structure ( $R -3 m$ ,  $a=4.30070$ ,  $c=11.22200$ ,  $\alpha=120.00000$ , Sb at 0.0, 0.0, 0.234). 75:25 was not fitted. Below, we show the goodness-of-fit statistical parameters (table 3-1) as well as data + fits (figure 3-4), for amorphous 15:85 and 50:50. These were chosen as representatives of the fit quality obtained in the other amorphous and annealed data sets analyzed.

Table 3-1: Final fitting statistical parameters for Ge and Sb K edges for amorphous 15:85 and 50:50 showing the Fourier transform ranges ( $\Delta k$ ), fitting ranges ( $\Delta R$ ), the R factor for each data set (R), the number of independent parameters used in the fits ( $N_{ind}$ ), the number of variables ( $N_{var}$ ), the chi-squared ( $\chi^2$ ), the reduced chi-squared ( $\chi^2_v$ ), the R factor, and the measurement uncertainty in R ( $\epsilon$ ).

<b>Data Set</b>	<b><math>\Delta k</math></b>	<b><math>\Delta R</math></b>	<b>R</b>	<b><math>N_{ind}</math></b>	<b><math>N_{var}</math></b>	<b><math>\chi^2</math></b>	<b><math>\chi^2_v</math></b>	<b><math>\epsilon</math></b>
Ge_15:85	3.0:13.5	1.6:3.0	0.007	8.9	6	393.4	135.9	0.001
Sb_15:85	3.0:12.5	1.8:3.1	0.0038	7.75	6	27.05	15.4	0.0018
Ge_50:50	3.0:13.0	1.6:3.5	0.0046	11.9	7	910.72	187.60	0.0006
Sb_50:50	3.0:12.0	1.8:3.1	0.016	13.8	9	173.28	36.06	0.0024

In table 3-1, the goodness-of-fit parameters are different between edges, and even between data sets. This is a good example of the poor scaling of the  $\chi^2$  and  $\chi^2_v$  statistical parameters in FEFF. Generally speaking, we can only look for statistically significant

changes between two  $\chi^2_v$  within a specific fitting model for a data set, where an improved  $\chi^2_v$  is a decrease of greater/equal to two standard deviations. Furthermore, the 50:50 sample had comparatively higher levels of random noise in the data, especially at higher k. To compensate, we used smaller k ranges, as well as multiple data set (MDS) fitting, which has the advantage of increasing the number of independent variables. MDS is appropriate when each data set in the fit contains related structural elements (for instance, the tetrahedral Ge environments) which can be fit simultaneously for all data sets. The Ge edge data for 50:50 was fit simultaneously with 75:25, constraining both to have similar bond variables. Also, the Sb edge was fit simultaneously with as-deposited Sb reference data, constraining both to have similar Sb-Sb bond variables (R and  $\sigma^2$ ). 15:85 was not MDS fitted, and consequently  $\chi^2_v$  cannot be compared in this case.

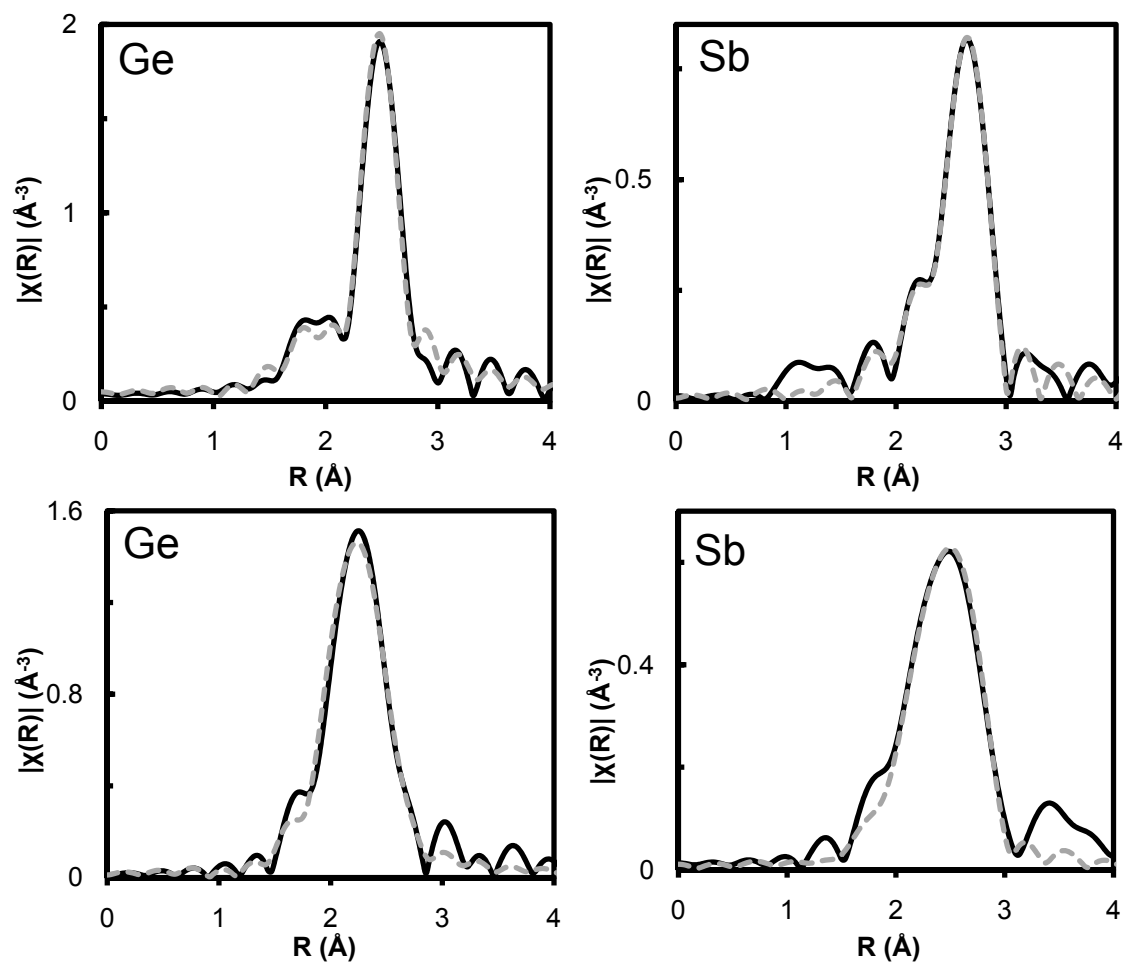


Figure 3-4: Fits to the Ge and Sb K edge for 15:85 (top) and 50:50 (bottom). Magnitude of the complex Fourier transformed of EXAFS spectra is shown. Solid black line = data, gray dashed line = fit. These fits are representative of the typically good fit to data obtained in all amorphous and annealed  $\text{Ge}_x\text{Sb}_{(1-x)}$ .

Table 3-2: A summary of the fitting parameters calculated from the fits to the amorphous  $\text{Ge}_x\text{Sb}_{(1-x)}$  samples and their percent errors. Each alloy shows both the parameters from the Ge edge as well as the Sb edge. In total, 71 parameters are determined from the 10 data sets (5 samples, 2 edges).  $S_0^2$  was 0.8 for all Ge edge data and 0.9 for all Sb edge data.

Alloy	Bond	N	$\sigma^2(\text{\AA}^2)$	E(eV)	R (Å)
75:25	Ge-Ge	3.44 +/- 0.52	0.005 +/- 0.001	5.94 +/- 1.9	2.47 +/- 0.02
	Ge-Sb	0.56 +/- 0.10	0.004 +/- 0.003		2.68 +/- 0.01
	Sb-Ge	2.77 +/- 0.5	0.006 +/- 0.001	5.10 +/- 1	2.68 +/- 0.01
	Sb-Sb	0.38 +/- 0.2	0.002 +/- 0.001		2.90 +/- 0.01
50:50	Ge-Ge	2.68 +/- 0.5	0.004 +/- 0.002	4.83 +/- 2.5	2.47 +/- 0.02
	Ge-Sb	1.32 +/- 0.2	0.005 +/- 0.003		2.68 +/- 0.01
	Sb-Ge	2.32 +/- 0.5	0.008 +/- 0.002	6.74 +/- 2.4	2.70 +/- 0.02
	Sb-Sb	0.81 +/- 0.3	0.006 +/- 0.001		2.89 +/- 0.02
25:75	Ge-Ge	1.40 +/- 0.1	0.005 +/- 0.0002	3.16 +/- 1	2.45 +/- 0.01
	Ge-Sb	2.60 +/- 0.2	0.004 +/- 0.001		2.67 +/- 0.02
	Sb-Ge	0.79 +/- 0.3	0.004 +/- 0.003	6.25 +/- 2	2.68 +/- 0.02
	Sb-Sb	2.23 +/- 0.5	0.007 +/- 0.001		2.90 +/- 0.01
15:85	Ge-Ge	0.80 +/- 0.1	0.005 +/- 0.0002	3.76 +/- 0.59	2.45 +/- 0.01
	Ge-Sb	3.20 +/- 0.5	0.005 +/- 0.001		2.67 +/- 0.02
	Sb-Ge	0.60 +/- 0.1	0.004 +/- 0.002	5.10 +/- 0.75	2.68 +/- 0.02
	Sb-Sb	2.40 +/- 0.3	0.004 +/- 0.001		2.89 +/- 0.01
7:93	Ge-Ge	0.27 +/- 0.1	0.008 +/- 0.005	3.31 +/- 0.6	2.46 +/- 0.01
	Ge-Sb	3.63 +/- 0.4	0.005 +/- 0.001		2.67 +/- 0.02
	Sb-Ge	0.24 +/- 0.2	0.003 +/- 0.003	4.42 +/- 2	2.70 +/- 0.02
	Sb-Sb	2.76 +/- 0.3	0.005 +/- 0.001		2.89 +/- 0.01

The calculated parameters for the amorphous samples shown in table 3-2 were mostly consistent in R and  $\sigma^2$ . We allowed the Sb-Ge and Ge-Sb bond distances to vary independently, and with the exception of 50:50 and 07:93, these bond lengths were consistent. A multi-edge refinement is appropriate in this system. This means fitting both the Ge and Sb edge simultaneously in order to implement useful constraints (e.g  $R_{\text{Ge-Sb}} = R_{\text{Sb-Ge}}$ ). It was not helpful due to the signal to noise in the Sb data. We noticed that the  $\sigma^2$  for the Ge-Ge bonds of the 07:93 sample had high uncertainties, due to high correlation to the measured bonding fraction of (a small fraction of) Ge-Ge bonds. The values for coordination shown

reflect the bonding fraction percent of each bond type at the respective edges. The fraction of Ge-Sb and Sb-Ge bonds, as measured at each edge versus composition, is shown in figure 3-5 below.

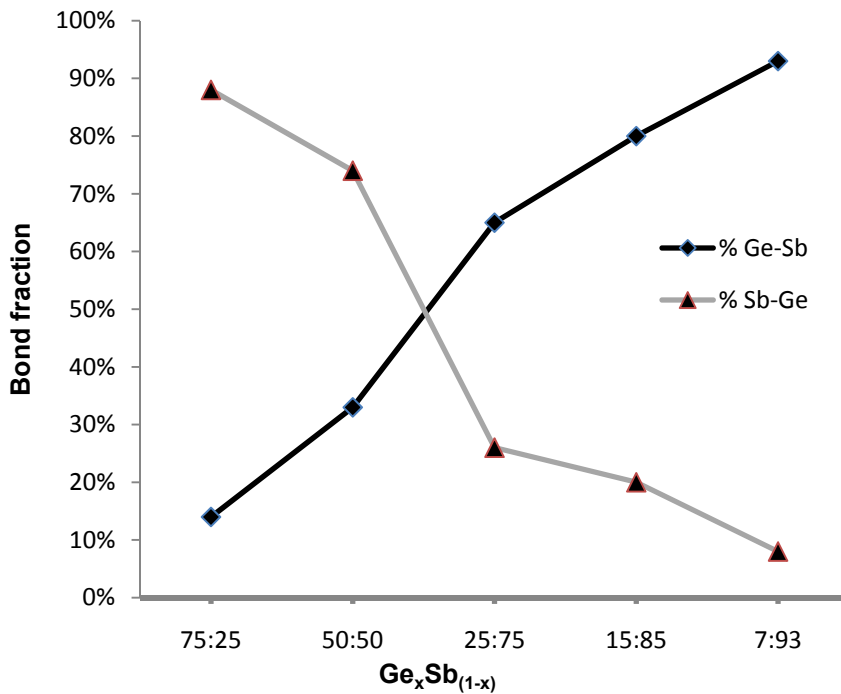


Figure 3-5: Ge-Sb bonding fraction calculated from the Ge edge (black line), versus the Sb-Ge bond fraction calculated at the Sb edge (gray line) of the  $Ge_xSb_{(1-x)}$ . We can compare the fraction of Ge atoms bonded to Sb (as opposed to Ge-Ge bonds) and the fraction of Sb environment bonded to Ge (as opposed to Sb-Sb).

As the atomic fraction of Ge in the system increases, Ge-Ge bonds are preferential compared to Ge-Sb bonds, and the composition with the most Ge as-deposited, had the fewest Ge-Sb bonds. Expectedly, the Sb bonding fraction shows a similar trend: as the Sb content increased, Sb-Sb bonds replace Sb-Ge bonds. The calculated parameters for the annealed films at the both edges are shown as an appendix.

### 3.1.2 EXAFS vs XRD in annealed 15:85

Cabral et al. used in-situ time resolved XRD measurements to show that crystallization of 15:85 films was divided into a two step process in which the crystallization of Sb first occurs at 240°C, evidenced by the appearance of the (003) and (101) rhombohedral peaks, and later at 350 °C, Ge (111) peaks appear [113]. They also indicated that temperature-induced Ge diffusion, and the presence of pure crystalline Sb could be the cause of Ge precipitation and subsequent crystallization via a metal-induced trigger mechanism [114]. Figure 3-6 shows the in-situ XRD data they measured for 15:85.

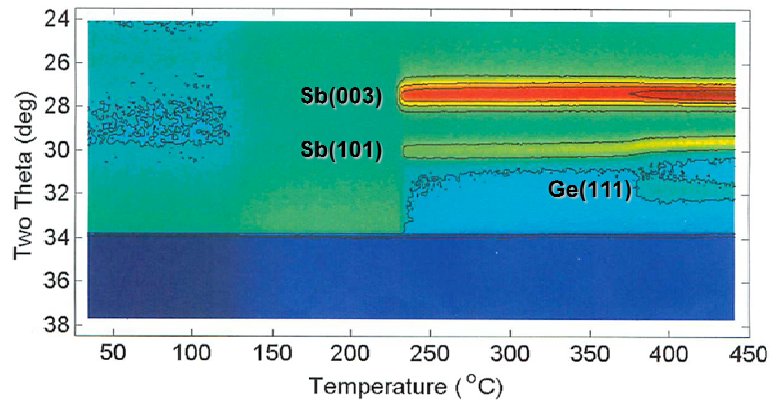


Figure 3-6: *In situ* XRD of 15:85 film during a 1°C/min ramp anneal in He. At crystallization, Bragg peaks of Sb with Ge in solid solution are seen. Ge (111) peak appears at 375°C (from ref [114]).

Using the same apparatus, we ramped samples of 15:85 to 300°C, in order to use EXAFS to investigate the Ge local structure prior to the observed Ge crystallization at 375°C. We did not collect any Sb edge EXAFS on this sample. Figure 3-7 shows a comparison of the FT  $|\chi(R)|$  EXAFS for 15:85: as-deposited, after a 300°C ramp/quench, and after a 400°C 30 minute anneal. The black arrow in the figure shows a feature at low R of the

300°C ramp/quench sample which depends on the parameters chosen for background removal. It is likely that an oxide layer was formed on the sample post-anneal (sample was annealed in a He ambient), but we could not separate what was attributable to background or surface oxide. Our fits to this data set excludes this region, where  $\Delta R_{\text{fit}} = 1.7 - 3.0 \text{ \AA}$ .

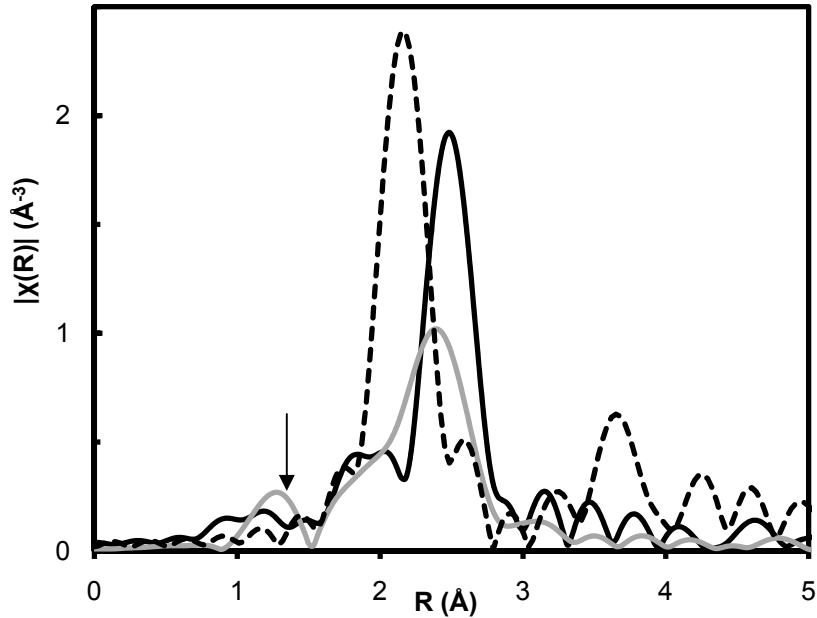


Figure 3-7: Comparison of the magnitude of the complex Fourier transform of the EXAFS data at the Ge K edge 15:85 as deposited (black dash line), after a 300°C ramp/quench (gray solid line), and after a 400°C 30 minute anneal (solid black line).

The change in phase seen in the EXAFS data of the as-deposited (solid black line) and the annealed (black dashed line) material is clearly related to the crystallization and phase separation of Ge and Sb crystal as observed in XRD [8; 29]. This behavior is also predicted by the Ge-Sb binary phase diagram [115], where no thermodynamically stable intermediate phases are possible with increasing temperature. Others have shown that  $\text{Ge}_x\text{Sb}_{(1-x)}$  alloys prepared by splat cooling showed a structure similar to the Sb As-A7 crystal structure, and identified a new tetragonal distorted NaCl-B1 type structure [116]. Since splat

cooling involves rapid quenching from a melt, we cannot confirm (or deny) this unique phase from a study of amorphous as-deposited and annealed 15:85. Instead, we want to understand the Ge local structure of the 300°C ramp/quench sample (solid gray line in figure 3-7).

The local structure of the metastable crystalline phase of many PCMs in the Ge-Sb-Te ternary system, including  $\text{Ge}_2\text{Sb}_2\text{Te}_5$  [30; 31],  $\text{Ge}_1\text{Sb}_2\text{Te}_4$  [117],  $\text{Ge}_1\text{Sb}_4\text{Te}_7$  [118], GeTe [119],  $\text{Sb}_2\text{Te}_3$  [120] as well as several  $(\text{GeTe})_x(\text{Sb}_2\text{Te}_3)_{1-x}$  glasses [121; 122], are based on the distorted, 6-fold coordinated, A7 rhombohedral structure of GeTe. This structure is a distorted NaCl rocksalt Fm-3m crystal structure in which Ge and Sb atoms randomly occupy the 4(b) site, together with approximately 20 at.% vacancies, while the 4(a) site is occupied by Te atoms only [123]. Pure Sb is a simple PCM which also crystallizes into a similar distorted A7 rhombohedral structure [124]. XRD and EXAFS shows that Sb in the  $\text{Ge}_x\text{Sb}_{(1-x)}$  system crystallizes into this structure as well. In the amorphous phase, Sb can form covalent bonds to three nearest neighbors via its three available p electrons in a pyramidal trigonal configuration, while in the crystalline phase it forms a 6-fold octahedral configuration. Pauling coined the term resonant bonding to describe the situation where covalent bonding occurs with unsaturated bonds, that is, less than two electrons per bond [125]. Resonant bonding was used to describe the local, and medium range bonding of crystalline Sb as well as other PCMs in the Ge-Sb-Te system, and it also explained the pronounced electron delocalization and significantly increased electron polarizability observed post anneal [126]. Tetrahedrally coordinated,  $sp^3$ -bonded semiconductors, such as Ge, are excluded from resonance bonding since they possess on average 4 valence electrons per atom, and strong

saturated covalent bonds are more likely. This fact, coupled with the nature of crystalline Sb, explains the observed phase segregation after the 400°C anneal: as Sb crystallizes into a resonant bonding environment, medium range rhombohedral Sb ordering develops, leading to Ge clustering as well as thermally induced Ge diffusion. It follows that the Ge edge EXAFS of the 300°C ramp/quench sample is not a new phase, but rather an amorphous, yet-to-be segregated Ge phase. We modeled the 300°C sample as a mixture of 4-fold tetrahedral Ge-Ge and Ge-Sb bonds found in the as-deposited 15:85 system and obtained very good fits to the data.

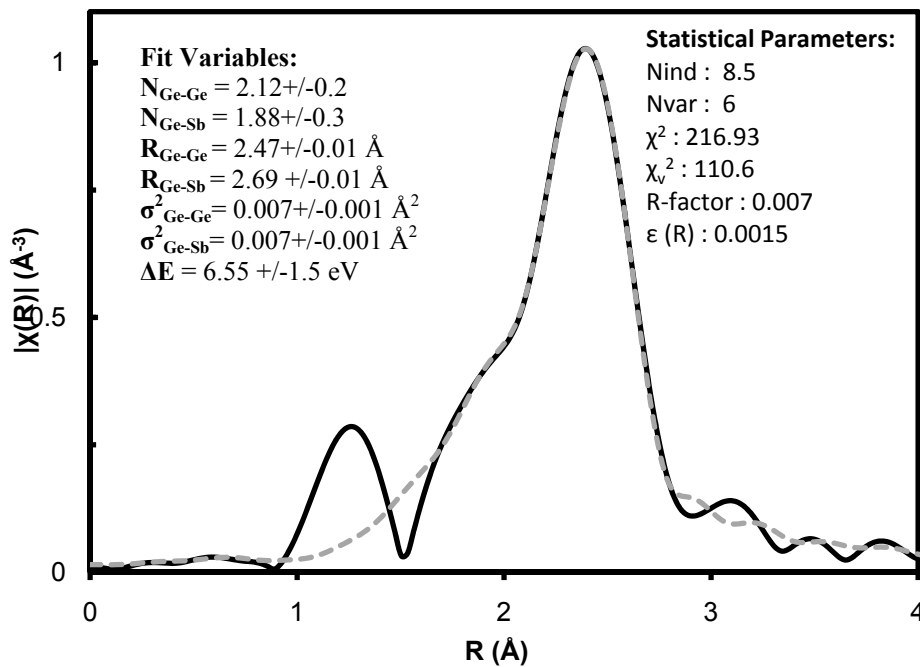


Figure 3-8: Fits to the Ge K edge for 15:85 after a 300°C ramp/quench. Magnitude of the complex Fourier transformed of EXAFS spectra is shown. Solid black line = data, gray dashed line = fit. For convenience, we show the calculated fit variables and the statistical goodness-of-fit parameters in the figure.

Figure 3-8 shows the data and fit to the 300°C ramp/quenched sample. The low R surface oxide / background feature was not included in the fitting range ( $\Delta k=3.0 - 13.0$ ; and  $\Delta R=1.6 - 3.0$ ). As compared with the as-deposited amorphous 15:85 sample fits (see table 3-2), we see an increase in both the bond distances and structural disorder term in this sample, which explains the drop in amplitude compared to a-15:85 and 400°C annealed 15:85. The amplitude of the EXAFS equation is attenuated by both these occurrences, through the  $\frac{1}{r_j^2}$  as well as  $e^{-2\sigma_j^2 k^2}$  dependence. Physically, this can be interpreted as an increase in the strain associated with Ge-Sb and Ge-Ge bonds in the ...Ge-Ge-Sb-Sb... environment which becomes more common at the boundary between crystallized Sb and amorphous Ge. Further comparison to as-deposited amorphous 15:85 shows an increase from 20% to 53% of the Ge-Ge bonding. This indicates that Ge diffusion and precipitation is a gradual process which proceeds as Sb crystallizes and Ge-Sb bonds are broken [114]. The implication is that there is no intermediate phase in the Ge local environment, as crystallization progresses. The Ge local structure remains in the metastable alloy phase, becoming increasingly rich in Ge-Ge bonds with increasing temperature, with Ge-Sb bonds becoming increasingly strained at the Ge boundary, until finally Ge aggregates and crystallizes, possible via a metal-induced crystallization.

### 3.2 EXAFS of as-deposited $(\text{Ge}_{15}\text{Sb}_{85})_x\text{Te}_{(1-x)}$ & $(\text{Ge}_{50}\text{Sb}_{50})_x\text{Te}_{(1-x)}$

$\text{Ge}_x\text{Sb}_{(1-x)}$  forms a metastable alloy, as deposited, but these films crystallize separately as Ge and Sb upon annealing. We wanted to investigate what structural changes occur in the

binary Ge-Sb system as Te is gradually added to the system to potentially understand what role the Te plays in bridging the Ge-Sb network. In this section, we look at the Ge K edge EXAFS of these films, as-deposited amorphous. Ge-Sb-Te films were deposited on bare Si wafers via co-sputtering from elemental targets with Ge:Sb:Te ratios targeting the composition  $(\text{Ge}_{15}\text{Sb}_{85})_x\text{Te}_{(1-x)}$  ( $x = 0.9, 0.8$ ) as well as  $(\text{Ge}_{50}\text{Sb}_{50})_x\text{Te}_{(1-x)}$  ( $x = 0.9, 0.8, 0.66$ ), as determined by Rutherford Backscattering Spectrometry (RBS). The compositions were varied by changing the relative powers of the Ge, Sb, and Te sputter sources. We will follow the convention of referring to the Ge:Sb composition + the % Te in the film, e.g. 50:50+33 is  $(\text{Ge}_{50}\text{Sb}_{50})_{0.66}\text{Te}_{0.33}$ .

### 3.2.1 EXAFS of the amorphous 15:85+Te & 50:50+Te

Ge K edge measurements were performed on the as-deposited films, and we followed similar data processing and background removal methods as discussed previously. These background removal parameters are relevant for all the amorphous and annealed 15:85+Te and 50:50+Te samples:  $\Delta k = [0.0 : 15.06 \text{ \AA}^{-1}]$ ,  $R_{\text{bkg}} = 1.0 \text{ \AA}$ , pre-edge =  $[-97.1 : -86.5]$ , and post-edge =  $[78.5 : 859.38]$ . The  $|\chi(R)|$  EXAFS of 15:85+(10, 20) and 50:50+(10, 20, 33) are shown in figure 3-9 .

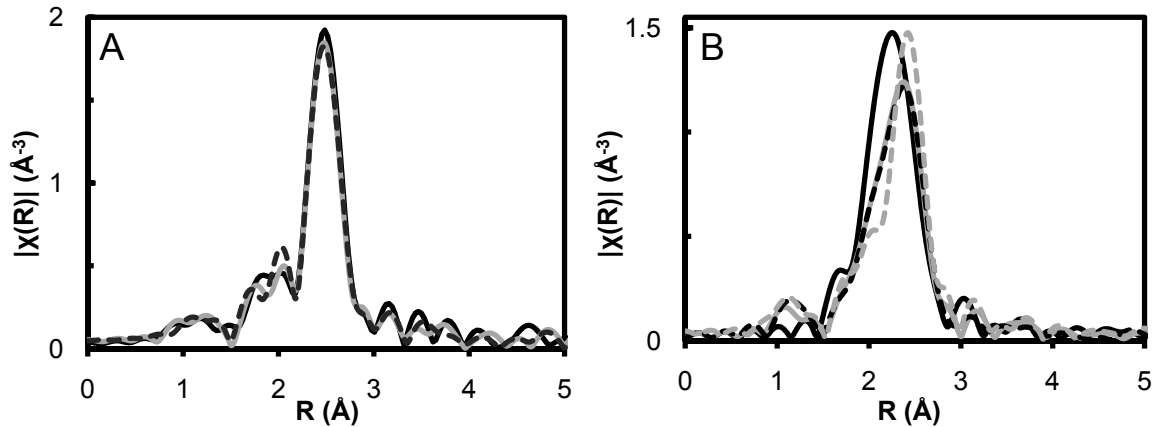


Figure 3-9: Comparison of the magnitude of the complex Fourier transform of the Ge K edge EXAFS for the as deposited (A) 15:85+Te and (B) 50:50+Te, for samples with no Te (solid black line), 10% Te (solid gray line), 20% Te (black dashed line), and 33% Te (gray dashed line).

As Te was added to the 15:85 samples, there was hardly any observable change in local structure, unlike the 50:50 samples, in which there was significant shift in structure as Te was increased during deposition. Initially we interpreted this as an indication that the high concentration of Sb-Sb bonds present meant that Te was bonding mainly to Sb in 15:85, while Ge-Te bonds were predominantly being formed in 50:50+Te. Consequently, we modeled the 15:85+Te system exactly as discussed and fitted in section 3.1.1, while the 50:50+Te system was modeled using a similar model to amorphous GST, that is, a 4-fold, tetrahedral mixture of  $(\text{Ge-Ge})_x, (\text{Ge-Sb})_y$  and  $(\text{Ge-Te})_{(1-x-y)}$ , where  $x$  and  $y$  are fractions to be determined. Our initial fits using these assumptions looked very good, but they were misleading. In 15:85, we noticed that the fitted Ge-Sb bond length was consistently 2.65  $\text{\AA}$  in the Te containing samples, meaning that the average bond length decreased by 0.03  $\text{\AA}$  (+/- 0.005  $\text{\AA}$ ). In 50:50+Te, we noticed that the fitted values for the Ge-Te bond distance was increased to  $R=2.66$   $\text{\AA}$  (from expected 2.61  $\text{\AA}$ ) and the Ge-Te bond fraction was close to zero.

There were also extremely high correlations between the mixing variables for Ge-Te and Ge-Sb, and their bond distances. These false “good” fits were caused by the similarity in backscattering from Sb and Te, as observed by the Ge absorbers in the system, and consequently the difficulty of defining an adequate set of muffin tin potentials to approximate the difference between the two. Since the effective scattering amplitude in the EXAFS equation depends on the ‘Z’ number of the scattering element, it is difficult to distinguish between Sb and Te, especially here where both Sb and Te nearest neighbors are equally likely. We obtained reasonable bond distances for Ge-Te and Ge-Sb by restraining them to be around values as predicted by their tabulated covalent bond radius (Ge-Te = 2.59 +/- 0.02, Ge-Sb=2.68 +/- 0.02) [127]. This restraint dramatically improved fits in both the 50:50+Te and the 15:85+Te system. Finally, we increased the number of independent variables by performing an MDS fit, constraining the R and  $\sigma^2$  for each bonding environment in 15:85+Te, as well as 50:50+Te to be the same. The goodness of fit parameters are shown in table 3-3, the calculated fitting parameters are shown in table 3-4, while the fits are shown together in figure 3-10.

Table 3-3: Final fitting statistical parameters for Ge and Sb K edges for a-15:85+Te and 50:50+Te showing the Fourier transform ranges ( $\Delta k$ ), fitting ranges ( $\Delta R$ ), the R factor for each data set (R), the number of independent parameters used in the fits ( $N_{ind}$ ), the number of variables ( $N_{var}$ ), the chi-squared ( $\chi^2$ ), the reduced chi-squared ( $\chi^2_v$ ), the R factor, and the measurement uncertainty in R ( $\epsilon$ ). 15:85+Te samples were fit together in a MDS, as were 50:50+Te, and shared parameters are shown in parentheses () and brackets [].

Data Set	$\Delta k$	$\Delta R$	R	$N_{ind}$	$N_{var}$	$\chi^2$	$\chi^2_v$	$\epsilon$
15:85+10	3.0:14.5	1.7:3.0	0.0090	(18.3)	(11)	(795.5)	(108.4)	(0.0015)
15:85+20	3.0:14.5	1.7:3.0	0.0069	(18.3)	(11)	(795.5)	(108.4)	(0.0015)
50:50+10	3.0:14.5	1.7:3.0	0.0027	[28.17]	[17]	[1228.56]	[109.9]	[0.0012]
50:50+20	3.0:14.5	1.7:3.0	0.0051	[28.17]	[17]	[1228.56]	[109.9]	[0.0012]
50:50+33	3.0:14.5	1.7:3.0	0.0083	[28.17]	[17]	[1228.56]	[109.9]	[0.0012]

Table 3-4: A summary of the fitting parameters calculated from the fits to the amorphous 15:85+Te and 50:50+Te samples and their uncertainties. In 15:85+Te, 16 parameters are determined from the 2 data sets while in 50:50+Te, 20 parameters were calculated from 3 data sets.  $S_0^2$  was 0.8 for all data sets.

	Bond	Bond %	N	$\sigma^2(\text{\AA}^2)$	$\Delta$ Energy (eV)	R ( $\text{\AA}$ )
15:85+Te	Ge-Ge	24 +/- 4%	0.95 +/-0.3 10 at%	0.010 +/-0.004	10 at% 3.46 +/- 0.5	2.47 +/-0.01
		20 +/- 4%	0.79 +/-0.3 20 at%			
	Ge-Sb	59 +/- 3%	0.68 +/-0.1 10 at%	0.002 +/-0.001	20 at% 3.86 +/- 0.4	2.69 +/-0.01
		59 +/- 4%	0.85 +/-0.1 20 at%			
	Ge-Te	17 +/- 6%	2.45 +/-0.1 10 at%	0.001 +/-0.001		2.58 +/-0.01
		21 +/- 6%	2.42 +/-0.1 20 at%			
50:50+Te	Ge-Ge	61 +/- 3%	2.45 +/-0.3 10 at%	0.007 +/-0.001	10 at% 4.83 +/- 0.71	2.47 +/-0.01
		61 +/- 3%	2.42 +/-0.3 20 at%			
		40 +/- 3%	1.58 +/-0.2 33 at%			
	Ge-Sb	21 +/- 3%	0.83 +/-0.1 10 at%	0.002 +/-0.002	20 at% 4.65 +/- 0.52	2.70 +/-0.01
		20 +/- 3%	0.81 +/-0.1 20 at%			
		28 +/- 3%	1.10 +/-0.13 33 at%			
	Ge-Te	18 +/- 3%	0.72 +/-0.1 10 at%	0.002 +/-0.001	33 at% 4.15 +/- 0.50	2.60 +/-0.01
		19 +/- 4%	0.77 +/-0.1 20 at%			
33 +/- 5%		1.31 +/-0.2 33 at%				

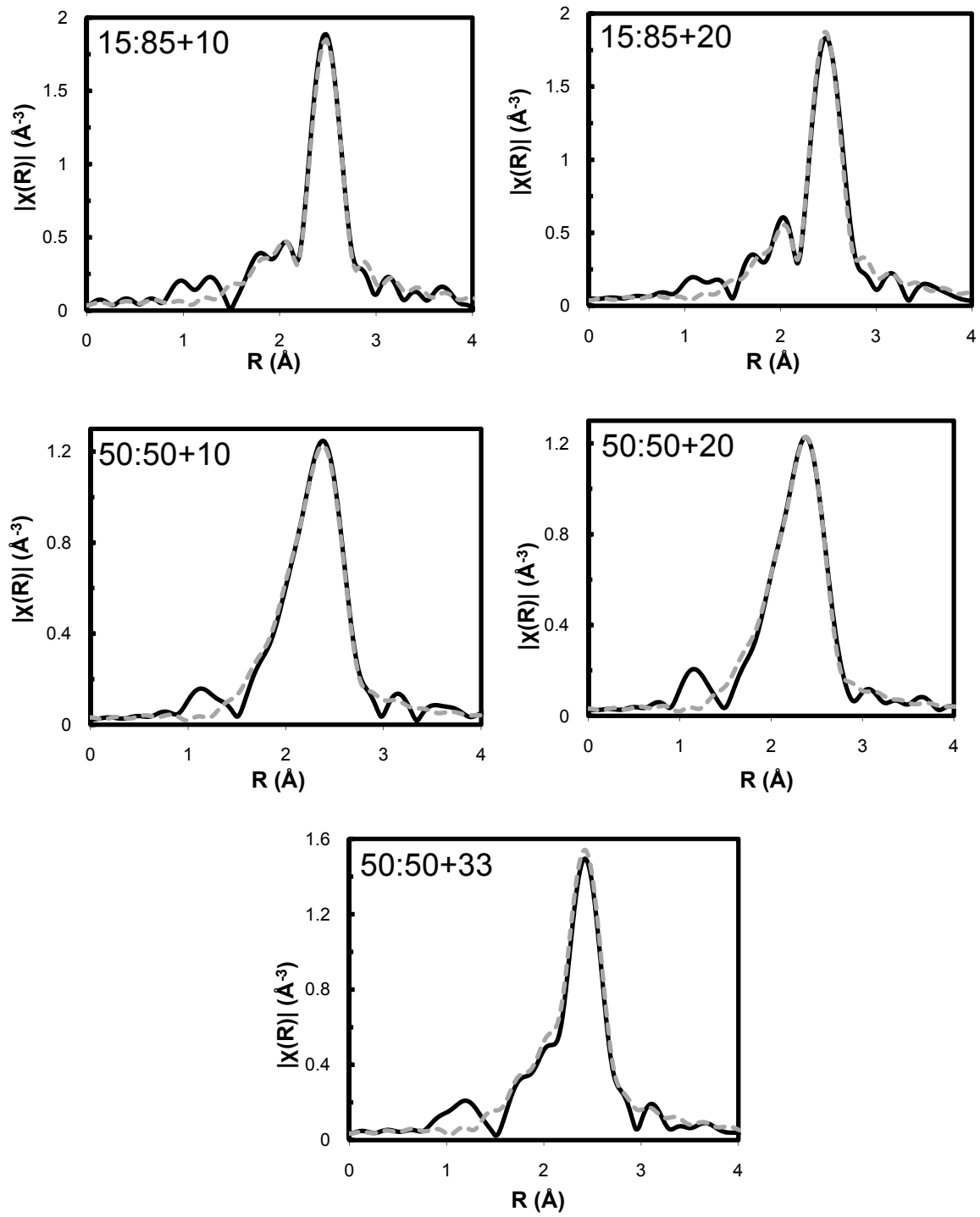


Figure 3-10: Fits to the Ge K edge for 15:85 +10 (20) and 50:50+10 (20, 33) samples. Magnitude of the complex Fourier transformed of EXAFS spectra is shown. Solid black line = data, gray dashed line = fit.

The calculated  $R$  and  $\sigma^2$  for the Ge-Sb and Ge-Te bond environments are consistent between 15:85+Te and 50:50+Te samples, and all bond lengths agree with expected physical values. We noticed higher than normal  $\sigma^2$  for the Ge-Ge bonds in 15:85+Te and 50:50+Te system. This is related to the change in  $R_{\text{Ge-Ge}}$  between 15:85 / 50:50 (2.45Å in table 3-3) and  $R_{\text{Ge-Ge}}$  in Te containing systems (2.47Å). Baker et. al reported a similar  $R_{\text{Ge-Ge}}$  of 2.47 in amorphous GST [70], as did Maeda et al in amorphous GeTe [80], which in both cases, correspond to ...Te-Ge-Ge-Te... bonding. These 15:85+Te and 50:50+Te results indicate both ...Ge-Ge-Ge-Ge... as well as ...Te-Ge-Ge-Te... bonding. The associated increase in  $\sigma_{\text{Ge-Ge}}$  is a measure of structural disorder due to a slight broadening in distribution of the Ge-Ge bond distances.

The higher uncertainties in the calculated Ge-Te bond fraction may only be improved by performing a multiple edge fit with the Te and Sb K edges. Notwithstanding, a comparison of the percent change in Ge bonding fraction environment with Te addition can give us an indication of the structural role of Te in the 15:85+Te and 50:50+Te system. In figure 3-11, we plotted the bond fraction found in each sample.

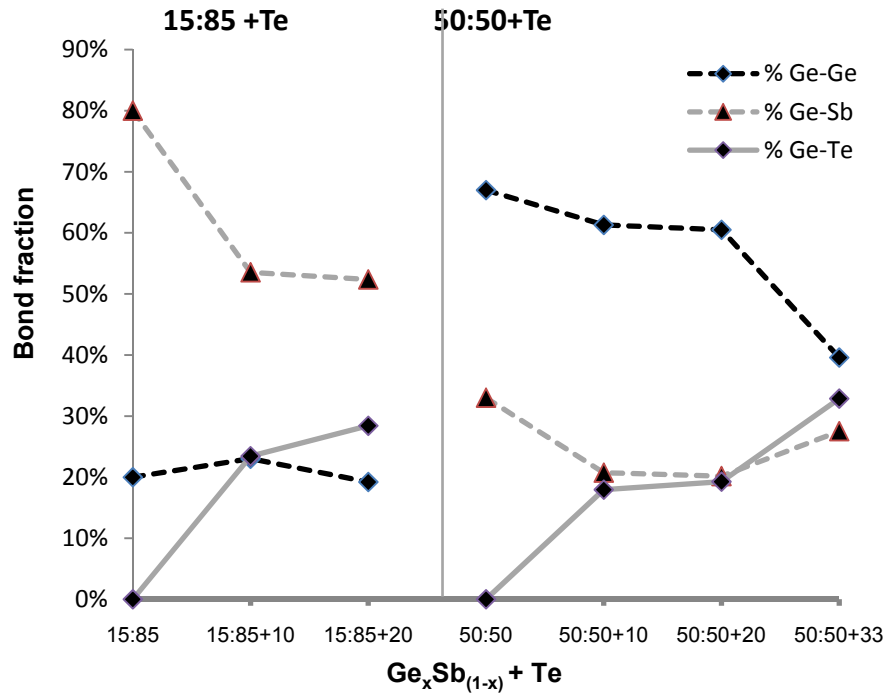


Figure 3-11: Change in bonding fraction of Ge-Ge (black dashed line), Ge-Sb (gray dashed line), and Ge-Te (gray solid line) at the Ge K edge in 15:85 and 50:50 with increasing Te content.

In 15:85, there is a slight increase in the fraction of Ge-Ge bonds, from 0% to 10% Te, and consequently, initial Ge-Te formation is at the expense of Ge-Sb bonds. However, the formation of further Ge-Te bonds in the 20% sample coincides with both a decrease in the fraction of Ge-Ge and Ge-Sb bonds. This coupled with our observed change in  $R_{\text{Ge-Ge}}$ , indicated that after the initial drastic decrease in the number of Ge-Sb bonds after Te addition, additional Te is more preferable to Ge-Ge bonds and is forming Ge-Te-Ge / Ge-Te-Sb chains in the 15:85 system.

In 50:50, the initial ratio of Ge-Ge to Ge-Sb bonds prior to Te addition is much higher. We noticed a decrease in both these bonding environments, as 10% Te is added and Ge-Te bonds were formed. There is a negligible change in the Ge bonding environment up to

20% Te addition. Within this range, Te was primarily bonding to Sb in this system, which explains the almost identical Ge edge bond distribution of 50:50+10 and 50:50+20 observed in EXAFS. In the 33 at% Te limit however, there is a dramatic decrease in the ratio of Ge-Ge bonding versus Ge-Te and Ge-Sb bonding. This is an indication that the sample containing 33% Te, exceeded a critical threshold whereby the added Te bonds favorably to both Sb and Ge, forming two-fold bridges in the glass network. In fact, this is what we will observe in GST, a system which also has equal Ge:Sb ratio.

### **3.3 EXAFS vs XRD of annealed $(\text{Ge}_{15}\text{Sb}_{85})_x\text{Te}_{(1-x)}$ & $(\text{Ge}_{50}\text{Sb}_{50})_x\text{Te}_{(1-x)}$**

In the 15:85+Te films in section 3.3.1, we compared the EXAFS and XRD data, and observed an interesting new structure post anneal. In the 50:50+Te films in section 3.3.2, we showed definitively that 50:50+33 does exceed a threshold Te content in which we start to see GST crystallization behavior. This will segue into section 3.4, where we clarify the nature of Ge-Sb bonds in  $\text{Ge}_2\text{Sb}_2\text{Te}_x$  ( $x=4, 5, 6, 7$ ).

#### **3.3.1 EXAFS vs XRD of annealed 15:85+Te**

In-situ, time resolved XRD measurements on these films were especially invaluable in corroboration with EXAFS. Figure 3-12 shows the in-situ XRD measurements for 15:85+10 and 15:85+20, taken during a  $1^\circ\text{C}/\text{s}$  ramp to  $450^\circ\text{C}$ , as well as the measured diffraction peaks acquired after the ramp.

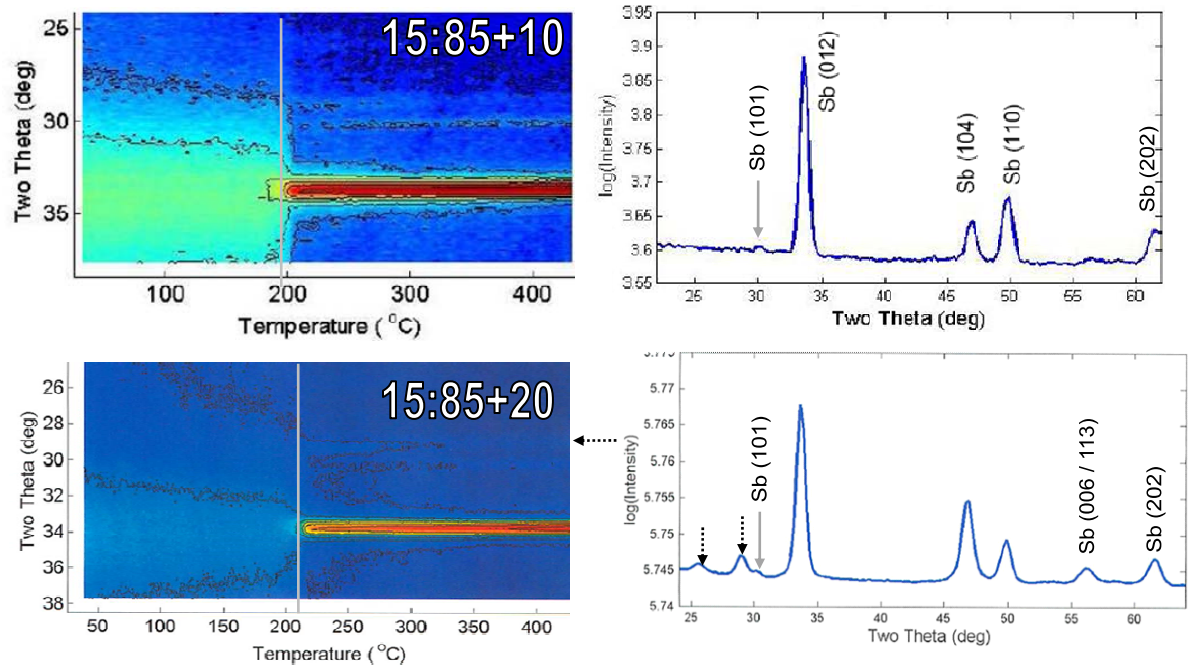


Figure 3-12: Intensity of diffracted x-ray peaks is plotted vs diffraction angle ( $2\theta$ ) over a range of  $15^\circ$  (vertical axis) vs temperature (horizontal axis) for blanket films of 15:85+10 and 15:85+20 heated at a rate of  $1^\circ\text{C}/\text{s}$ . This is shown alongside the Intensity vs ( $2\theta$ ) which was taken at  $450^\circ\text{C}$ . Transitions due to the crystalline Sb rhombohedral phase are marked by vertical solid gray lines. The black dotted arrows show un-indexed features. The Sb rhombohedral peak indices are indicated.

We noticed that the Sb crystal transition shifts to lower temperatures following Te addition – this transition occurred at  $240^\circ\text{C}$  in 15:85. The transition, corresponding to the appearance of the most intense peak, was indexed to the Sb (012) rhombohedral peak, and is related the Sb (As-A7) structure previously observed. In the  $2\theta$  scan taken at room temperature after the  $450^\circ\text{C}$  ramp the main observed peaks were all indexed (as shown) to the Sb crystal phase. Two low intensity peaks did appear following Te addition, but we are still unable to index these to either Sb crystal, Ge crystal, or GST NaCl cubic phases. Most interesting is what we did not observe. No diffraction peaks associated with the Ge crystal phase were observed over the  $450^\circ\text{C}$  ramp, as was clearly evident in the Te free 15:85 system. The addition of at least 10% Te in these films has prevented the diffusion and phase

separation of Ge, most likely related to the Ge-Te bonds formed as-deposited. This is very relevant to PCRAM applications because Ge and Sb elemental segregation and formation of Sb rich regions will lead to a failure of PCRAM cells [128].

We repeated the in-situ XRD measurements on as-deposited blanket films, this time to create EXAFS samples which were ramped to 300°C. We could not analyze the 450°C ramped samples because of an intense background contribution at low R in the EXAFS Fourier transform, possibly due to rapid surface oxidation which appeared upon removal from the helium ambient. It is acceptable to perform our EXAFS analysis on 300°C annealed samples since no new diffraction peaks appeared in the in-situ XRD spectrum between 300°C and 450°C. The normalized Ge near edge comparison and EXAFS of the 300°C ramped 15:85, 15:85+10 and 15:85+20 are shown in figure 3-13 and 3-14, respectively, using the same AUTOBK parameters for the as-deposited samples in section 3.2.1.

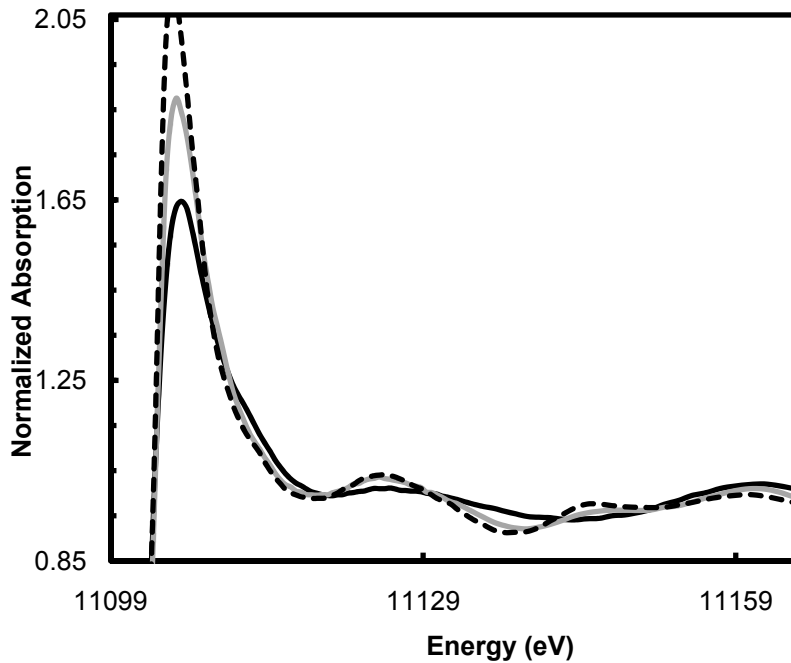


Figure 3-13: Normalized Ge near edge comparison of 300°C annealed 15:85 (solid black line), 15:58+10 (solid gray line), and 15:85+20 (black dashed line). The intensity of the white line, and the appearance of sharper near edge features coincide with Te addition.

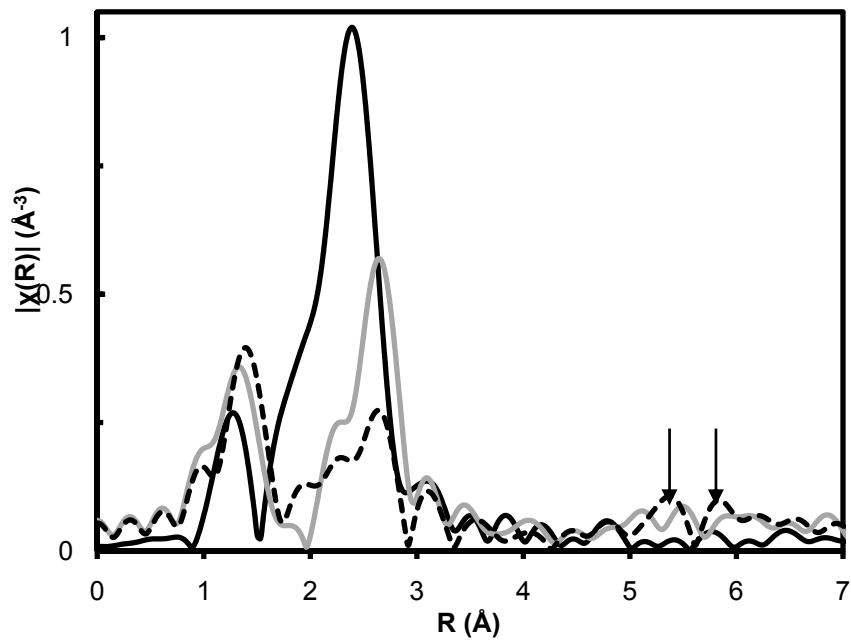


Figure 3-14: Comparison of the magnitude of the complex Fourier transform of the Ge K edge EXAFS for 300°C annealed 15:85 (solid black line), 15:58+10 (solid gray line), and 15:85+20 (black dashed line). The arrows show the appearance of long range order in 15:85+20.

At the near edge, we can clearly see the appearance of new, sharper features due to the creation of new available states following Te addition and annealing. We can also see that there is a distinct shift to longer bond distances in the nearest neighbor environment, and at the 20% Te limit we can start to see long range order, akin to FCC crystalline GST. Unfortunately, the data quality of the 15:85+Te samples, coupled with absence of the Sb and Te K edges, prevented us from fitting the data. But, the appearance of the features at the near edge, and this observed long range order, imply a structural model where there is a Ge-Te crystalline environment. And although there are still un-indexed peaks in the XRD, it is possible that this crystalline phase may not diffract strongly due to the small size and sparse distribution of these crystallites. EXAFS shows that there are in fact 2 crystalline phases present in 15:85+Te, i.e. an Sb rhombohedral phase, and local structural order in Ge-Te on the 10 Å length scale. Confirmation of the nature of this primitive crystal feature will require a future detailed study of the Te edge, where one may see Te in a similar structure as observed in 225, with a clearly defined peak at 4.26Å. At any rate, the presence of GST-like crystalline features explains why Ge precipitation did not occur in the 15:85+Te films. Atomic force microscopy (AFM) images of partially laser crystallized optical spots in amorphous, as-deposited thin films of GST and 15:85 showed significant differences [25]. In comparison with “nucleation dominated” GST, where many crystallization events were initiated throughout the optical spot, 15:85 is a “growth dominated” PCM showing only a few nucleation events within each optical spot. An AFM experiment of these 15:85+Te

samples may clarify the role of Te as a possible nucleation site, based on the abundance of nucleation spots in the AFM.

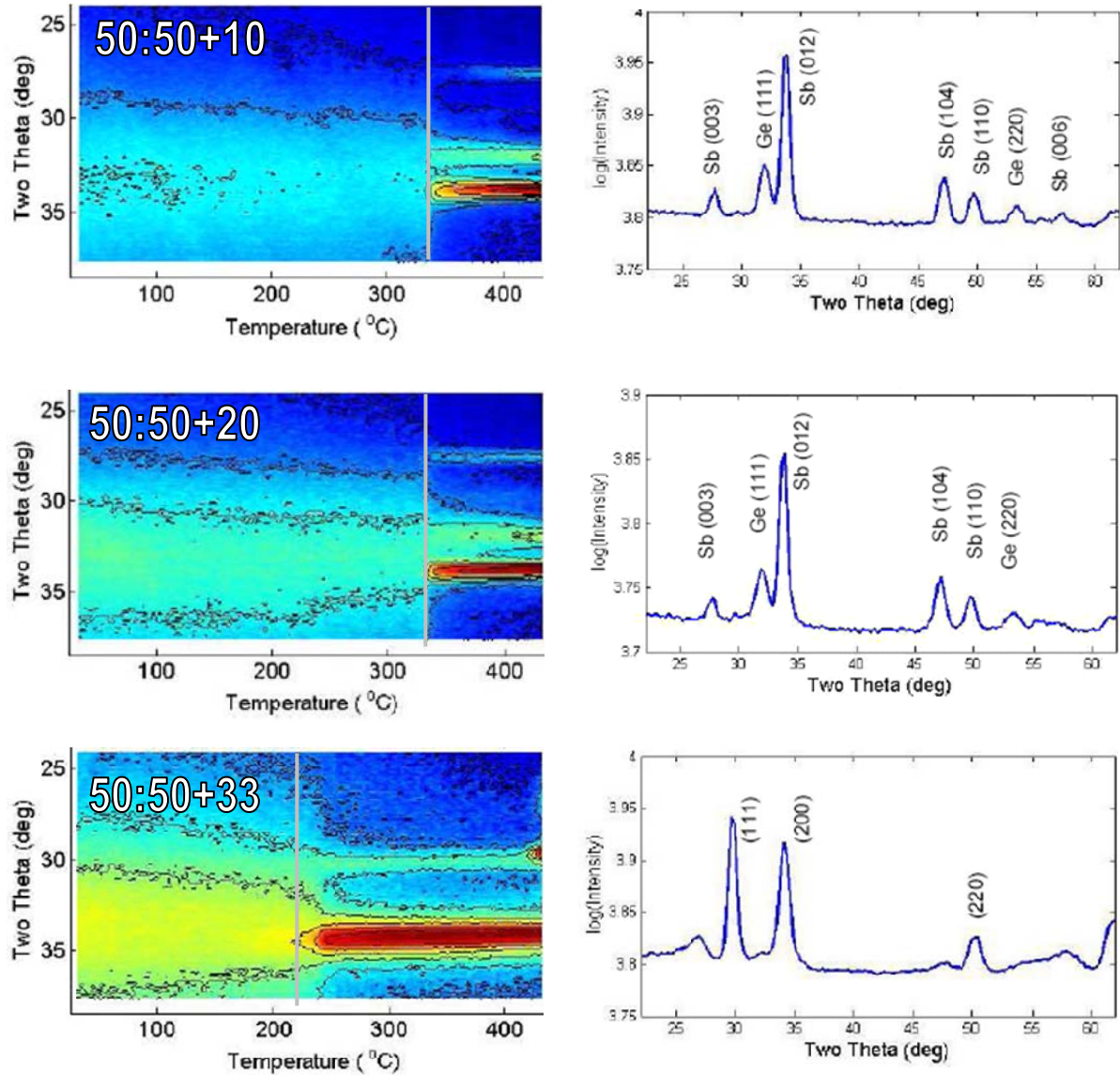


Figure 3-15: Intensity of diffracted x-ray peaks is plotted vs diffraction angle ( $2\theta$ ) over a range of  $15^\circ$  (vertical axis) vs temperature (horizontal axis) for blanket films of 50:50+10, 50:50+20, and 50:50+33, heated at a rate of  $1^\circ\text{C/s}$ . This is shown alongside the intensity vs ( $2\theta$ ) which was taken at room temperature after a ramp to  $450^\circ\text{C}$ . The Sb and Ge crystal peak indices are indicated, as well as the NaCl cubic phase indices in 50:50+33.

### 3.3.2 EXAFS vs XRD of annealed 50:50+Te

Figure 3-15 shows the in-situ XRD measurements for 50:50+10, 50:50+20, and the 50:50+33 films taken during a 1°C /s ramp to 450°C, as well as the measured diffraction peaks acquired at room temperature after the ramp. After the ramp, all peaks in the 50:50+10 and 50:50+20 samples were indexed to either cubic Ge, or rhombohedral Sb. The crystallization of the film was marked by the appearance of the intense Sb (012) peak, which occurred at the same temperature in both cases. On the other hand, this transition from the amorphous phase shifted to much lower temperatures in the 50:50:33 sample, and the observed peaks were indexed to the NaCl cubic phase.

We did not notice a similar large background contribution at low R in the EXAFS Fourier transform of these 450°C ramped samples, therefore no 300°C annealed samples were necessary. The normalized Ge near edge comparison and EXAFS of the 450°C ramped 50:50, 50:50+10 and 50:50+20 is shown in figure 3-16, using the same AUTOBK parameters for the as-deposited samples in section 3.2.1.

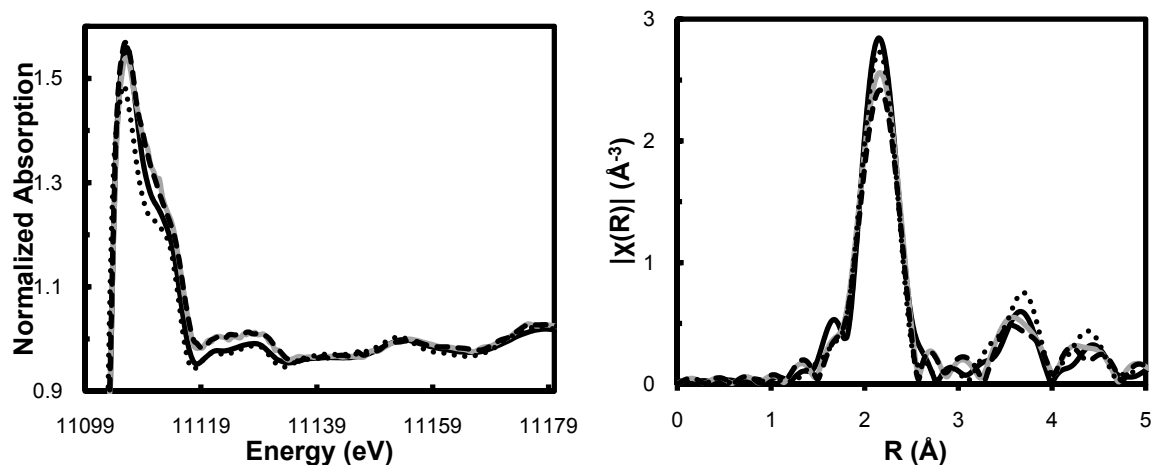


Figure 3-16: Comparison of (A) the normalized Ge near edge and (B) the magnitude of the complex Fourier transform of 450°C annealed 50:50 (solid black line), 50:50+10 (solid gray line), 50:50+20 (black dashed line), and Ge foil (black dotted line).

The near edge of 50:50, 50:50+10, 50:50+20, and Ge metal foil all share a similar, rich spectrum in the near edge region, typical of pure Ge crystal. And while this is an indication that this is the main local structural environment, it was important to see if there were any Te related features in the Te containing samples. In fact, we do see differences in the intensity of the white line and near edge region, corresponding to the addition of Te. However, it was very difficult to define a post-edge line which would accurately compare the quickly changing spectral region just after the edge. Also, these samples were measured under different florescence measurement conditions (solid state detector vs ionization chamber, different angle of incidence, etc.), with differing energy resolution in the near edge region, as well as different energy ranges for the absorption spectrum (which influences the behavior of the post-edge line). So it is unclear if what we see is actually Te related, or simply differences in normalization, or both. Unlike the 15:85+Te samples, there is no similar distinct shift to longer bond distances in the nearest neighbor environment of Ge, up

to the 20% Te limit, and neither do we see long range order, akin to FCC crystalline GST. The only long range order present is the second and third shell distance for crystalline Ge, as seen in XRD, which we were able to fit clearly in EXAFS. In light of NMR studies of the electronic response of the Te nucleus of various Ge-Sb-Te compounds [129], we postulate that Te-Te bonds are unlikely, and Te is likely bonded to Sb, possibly in the Sb rhombohedral lattice, or in a separate Sb-Te crystalline phase.

In the XRD above, we noticed the appearance of the cubic phase in 50:50+33. Consequently, we performed a normalized Ge near edge (figure 3-17) and an EXAFS (figure 3-18) comparison of the 450°C ramped 50:50+33 with undoped, 300°C, 30 minute, furnace annealed GST. We used the same AUTOBK parameters for the as-deposited samples in section 3.2.1.

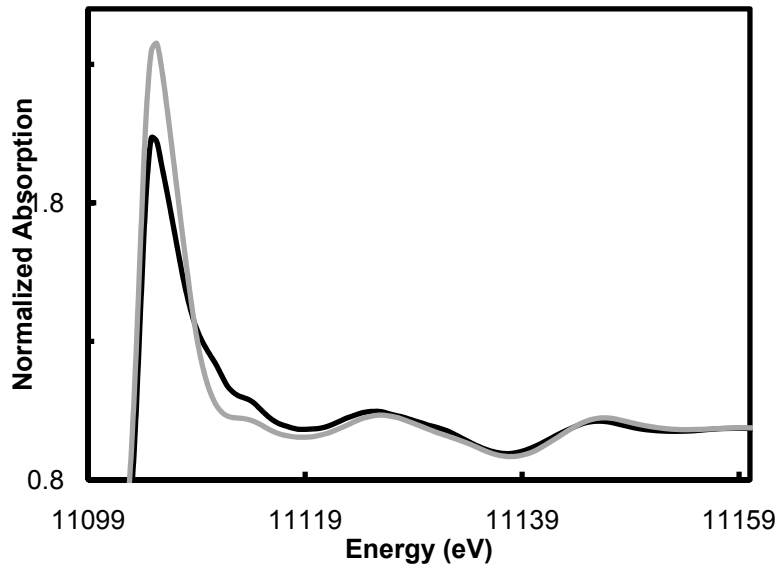


Figure 3-17: Normalized Ge near edge comparison of 450°C annealed 50:50+33 (solid black line) to 300°C annealed GST (solid gray line). Apart from a change in the intensity of the white line, both share similar near edge features

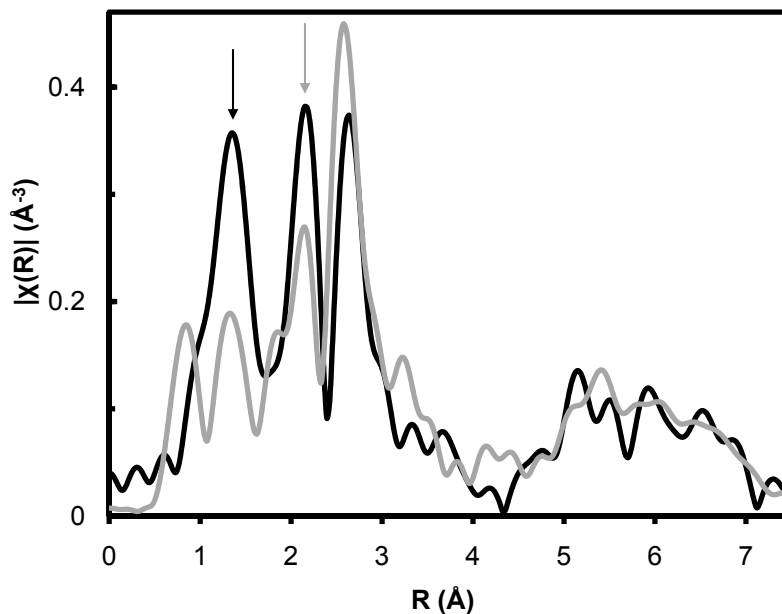


Figure 3-18: Comparison of the magnitude of the complex Fourier transform of the Ge K edge EXAFS for 450°C annealed 50:50+33 (solid black line) to 300°C annealed GST (solid gray line).

The similarities in the near edge region, and the shared long range order in the Ge edge EXAFS confirm that the Ge local structure of 50:50+33 and GST is quite similar. Since these samples were measured under different fluorescence conditions, the intensity of the white line may be attributed to un-normalized detector response effects. However, it is likely that this difference in intensity of the white line is mainly due to the higher concentration of Te states present in GST, which are accessible to the excited Ge photoelectron. The differences in nearest neighbor structure can be due to the presence of surface Ge-O (solid black arrow), as well as a fraction of Ge-Ge bonds (solid gray arrow) in 50:50:33, which likely phase separated post anneal as in all the 50:50+Te sample.

A quantitative analysis of these systems self consistent multi-edge analysis can help to answer questions as to the local structure of Te in 50:50+10 and 50:50+20. In these samples the Ge phase separation is seemingly unhindered by the addition of Te, unlike the 15:85+Te samples. A Te edge analysis would also help to clarify the similarities between FCC annealed GST and 50:50+33, where an important threshold has been passed, whereby the Te at% is sufficient to induce the nucleation of FCC crystallites in the system.

### **3.4 EXAFS of as-deposited $\text{Ge}_2\text{Sb}_2\text{Te}_x$**

Baker et al confirmed that the basic local structural units of as-deposited  $\text{Ge}_2\text{Sb}_2\text{Te}_x$  ( $x=4, 5, 6, 7$ ) observed the 8-N rule [130], however questions were raised as to the occurrence of Ge-Sb bonding. Their final EXAFS models were built on the hypothesis that the lone electron pair of Sb formed an electrostatic bond to a positively charged three-fold coordinated Te atom, leading to Sb-Te bonds at 2.51Å. Another study showed no Ge-Sb or Ge-Ge bonds in the Ge environment of the amorphous phase, where only tetrahedral Ge-Te bonds were present, although those samples were possibly reamorphized [101]. Both of these references highlight two mainstream concerns of an analysis of as-deposited  $\text{Ge}_2\text{Sb}_2\text{Te}_x$ : 1) the switched amorphous and as-deposited phase might be very different and 2) the similarity in effective scattering amplitude of Ge-Te and Ge-Sb bonding. In the first case, the experimental difficulty of reamorphizing a volume of PCM which is of sufficient size for an EXAFS experiment is the long standing experimental conundrum which prevents a trustworthy comparison of the as-deposited amorphous and the switched amorphous phases.

The conditions for rapidly quenched, laser switched GST films has been discussed in great detail elsewhere [131]. Fons et al performed an XAFS study of switched GST by synchronously applying both femtosecond and nanosecond laser pump pulses in conjunction with 100~ps x-ray pulses generated by a synchrotron [132]. Using their experimental apparatus, we later repeated this experiment on GST micro-devices and obtained similar results: significant unfavorable reaction of Ge with the surrounding dielectric layer, poor signal to noise, and primarily a qualitative Ge near edge analysis. As-deposited amorphous samples allow us to perform a detailed, quantitative, structural analysis at all three edges.

In the second case, the effective scattering amplitude  $F_j^{eff}(k)$  is similar between elements with nearly the same number of electrons. Thus, it is very difficult to distinguish between the EXAFS signal from Ge-Te and Ge-Sb (or Sb-Sb and Sb-Te) backscatters. Furthermore, the phase  $\sin(2kr_j + \vartheta_{oj}(k))$  term accounts for the oscillations in the EXAFS signal with a phase given by  $2kr_j + \vartheta_{oj}(k)$ . The path of the photoelectron is multiplied by wavenumber to determine the phase, while  $\vartheta_{oj}(k)$  is a phase shift of the photoelectron caused by the interaction of the photoelectron with both the nuclei of the absorber and the coordinating atoms. Consequently, the EXAFS oscillations of Ge-Te and Ge-Sb will be very similar. For our measurements, we mitigate this by measuring and analyzing all three edges for self consistency.

### 3.4.1 EXAFS analysis of as-deposited $\text{Ge}_2\text{Sb}_2\text{Te}_x$ ( $x=4,5,6,7$ )

Thin films of  $\text{Ge}_2\text{Sb}_2\text{Te}_x$  ( $x=4, 5, 6, 7$ ) were deposited to approximately  $\sim 2$  micron film thickness, at room temperature on Al foil by DC sputtering respective  $\text{Ge}_2\text{Sb}_2\text{Te}_x$  compound targets in an argon feedgas. Transmission EXAFS measurements at the Ge, Sb, and Te edges were done at the APS, MRCAT ID-10 in accordance with experimental details found in Ref [70]. We followed similar data processing methods previously discussed, with the resultant background removal parameters shown in table 3-5. We will use a convention of referring to samples in this section by their ratios of Ge:Sb:Te (e.g. ‘amorphous  $\text{Ge}_2\text{Sb}_2\text{Te}_7$  is ‘227’ or ‘a-227’).

Table 3-5: Background removal quantities used in AUTOBK for Ge, Sb, and Te K edges in  $\text{Ge}_2\text{Sb}_2\text{Te}_x$  samples.

Edge	$\Delta k$ ( $\text{\AA}^{-1}$ )	$R_{\text{bkg}}$ ( $\text{\AA}$ )	Pre-Edge	Post-Edge
Ge	[0.0 : 19.0]	1.5	[-197.1 : -86.5]	[80.1 : 1272.4]
Sb	[0.0 : 19.0]	1.5	[-197.1 : -86.5]	[89.1 : 1003.2]
Te	[0.0 : 19.0]	1.5	[-197.1 : -86.5]	[109.5 : 960.5]

A comparison of the Ge, Sb, and Te K edge EXAFS for 224, 225, 226, and 227 is shown in figure 3-19, where the x-axis was adjusted to show only the major peak from the magnitude of the Fourier transform  $|\chi(R)|$ . In the amorphous phase, we expect that the 8-N rule for covalent bonding is satisfied. Consequently, structural units modeled for these samples were 4-fold tetrahedral Ge, 3-fold pyramidal, trigonal Sb, and 2 fold coordinated Te. At the Ge edge, we fitted a mixture of  $(\text{Ge-Ge})_x + (\text{Ge-Sb})_y + (\text{Ge-Te})_{(1-x-y)}$  bonds, where x and y are fractions to be determined. At the Sb edge, Sb-Ge and Sb-Te bonds were similarly fitted, while the model Te environment consisted of both Te-Ge and Te-Sb bonds. We did not fit

Te-Te nor Sb-Sb bonding since the study of the 50:50+Te samples showed that Te preferentially link to Sb and Ge in the system after 33 at% Te addition. Bond energies for Sb-Te (40.6 kpm) and Sb-Sb (39.6 kpm) [133] support the assertion that at the Sb edge, Sb-Te (not Sb-Sb) bonds accounts for the backscattering signal [109]. The goodness of fit parameters for 225 are shown in table 3-6, the calculated fitting parameters for all samples are shown in table 3-7, and the fits for all edges of 225 are shown in figure 3-20. This 225 data is an accurate representation of the quality of fits obtained for the other samples.

Table 3-6: Final fitting statistical parameters for Ge, Sb and Te K edges for amorphous 225 showing the Fourier transform ranges ( $\Delta k$ ), fitting ranges ( $\Delta R$ ), the R factor for each data set (R), the number of independent parameters used in the fits ( $N_{ind}$ ), the number of variables ( $N_{var}$ ), the chi-squared ( $\chi^2$ ), the reduced chi-squared ( $\chi^2_v$ ), the R factor, and the measurement uncertainty in R ( $\epsilon$ ).

Data Set	$\Delta k$	$\Delta R$	R	$N_{ind}$	$N_{var}$	$\chi^2$	$\chi^2_v$	$\epsilon$
Ge	3.0:15.0	1.8:3.0	0.0076	16.9	13	792.51	397.03	0.0014
Sb	3.0:15.5	1.8:3.0	0.0014	9.24	7	61.78	27.58	0.0003
Te	3.0:12.5	1.7:3.1	0.002	8.31	6	293.51	127.3	0.0002

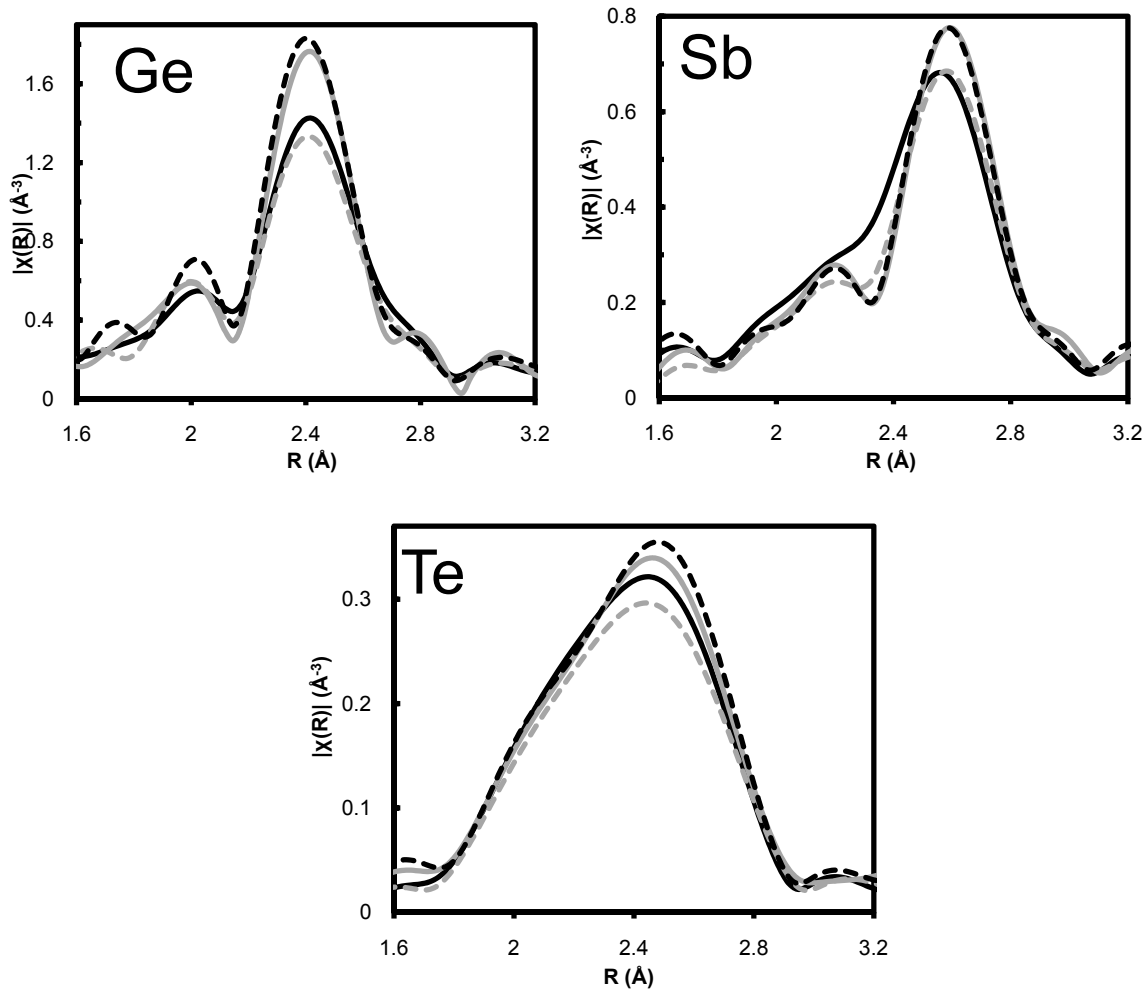


Figure 3-19: Comparison of the magnitude of the complex Fourier transform of the Ge, Sb, and Te K edge EXAFS for the as deposited 224 (solid black line), 225 (gray dashed line), 226 (solid gray line), and 224 (black dashed line). Only the range of interest ( $\sim 2 - 3 \text{\AA}$ ) is shown for clarity.

Table 3-7: A summary of the fitting parameters calculated from the fits to the amorphous  $\text{Ge}_2\text{Sb}_2\text{Te}_x$  samples and their uncertainties.  $S_0^2$  was 0.85 for all Sb and Te edge data, and 0.7 for Ge edges.

Alloy	Bond	N	$\sigma^2(\text{\AA}^2)$	E(eV)	R (\AA)
<b>a-224</b>	<b>Ge—Ge</b>	<b>0.48</b> +/- 0.04	<b>0.001</b> +/- 0.001	<b>3.75</b> +/- 0.8	<b>2.46</b> +/- 0.02
	<b>Ge—Sb</b>	<b>1.00</b> +/- 0.1	<b>0.005</b> +/- 0.0002		<b>2.67</b> +/- 0.03
	<b>Ge—Te</b>	<b>2.52</b> +/- 0.2	<b>0.005</b> +/- 0.001		<b>2.62</b> +/- 0.02
	<b>Sb—Ge</b>	<b>0.66</b> +/- 0.06	<b>0.003</b> +/- 0.001	<b>6.93</b> +/- 0.52	<b>2.68</b> +/- 0.02
	<b>Sb—Te</b>	<b>2.34</b> +/- 0.23	<b>0.007</b> +/- 0.001		<b>2.85</b> +/- 0.02
	<b>Te—Ge</b>	<b>1.14</b> +/- 0.1	<b>0.005</b> +/- 0.001	<b>4.64</b> +/- 0.84	<b>2.62</b> +/- 0.01
<b>Te—Sb</b>	<b>0.86</b> +/- 0.08	<b>0.006</b> +/- 0.001	<b>2.84</b> +/- 0.01		
<b>a-225</b>	<b>Ge—Ge</b>	<b>0.52</b> +/- 0.1	<b>0.001</b> +/- 0.001	<b>4.32</b> +/- 0.7	<b>2.47</b> +/- 0.02
	<b>Ge—Sb</b>	<b>0.32</b> +/- 0.1	<b>0.005</b> +/- 0.001		<b>2.67</b> +/- 0.02
	<b>Ge—Te</b>	<b>3.16</b> +/- 0.3	<b>0.005</b> +/- 0.001		<b>2.61</b> +/- 0.01
	<b>Sb—Ge</b>	<b>0.45</b> +/- 0.05	<b>0.003</b> +/- 0.001	<b>6.56</b> +/- 0.3	<b>2.69</b> +/- 0.01
	<b>Sb—Te</b>	<b>2.55</b> +/- 0.26	<b>0.007</b> +/- 0.001		<b>2.84</b> +/- 0.01
	<b>Te—Ge</b>	<b>1.08</b> +/- 0.15	<b>0.005</b> +/- 0.001	<b>4.63</b> +/- 0.84	<b>2.61</b> +/- 0.01
<b>Te—Sb</b>	<b>0.92</b> +/- 0.09	<b>0.005</b> +/- 0.001	<b>2.84</b> +/- 0.01		
<b>a-226</b>	<b>Ge—Ge</b>	<b>0.32</b> +/- 0.03	<b>0.004</b> +/- 0.001	<b>4.17</b> +/- 0.79	<b>2.48</b> +/- 0.01
	<b>Ge—Te</b>	<b>3.68</b> +/- 0.4	<b>0.005</b> +/- 0.001		<b>2.60</b> +/- 0.01
	<b>Sb—Ge</b>	<b>0.21</b> +/- 0.05	<b>0.002</b> +/- 0.001	<b>6.98</b> +/- 0.4	<b>2.71</b> +/- 0.02
	<b>Sb—Te</b>	<b>2.79</b> +/- 0.28	<b>0.007</b> +/- 0.001		<b>2.83</b> +/- 0.02
	<b>Te—Ge</b>	<b>0.92</b> +/- 0.1	<b>0.005</b> +/- 0.001	<b>4.65</b> +/- 0.74	<b>2.60</b> +/- 0.01
	<b>Te—Sb</b>	<b>1.08</b> +/- 0.1	<b>0.007</b> +/- 0.001		<b>2.82</b> +/- 0.01
<b>a-227</b>	<b>Ge—Ge</b>	<b>0.24</b> +/- 0.2	<b>0.002</b> +/- 0.001	<b>4.79</b> +/- 0.9	<b>2.45</b> +/- 0.01
	<b>Ge—Te</b>	<b>3.76</b> +/- 0.4	<b>0.005</b> +/- 0.001		<b>2.60</b> +/- 0.01
	<b>Sb—Ge</b>	<b>0.21</b> +/- 0.02	<b>0.001</b> +/- 0.0007	<b>6.96</b> +/- 0.46	<b>2.71</b> +/- 0.02
	<b>Sb—Te</b>	<b>2.79</b> +/- 0.3	<b>0.007</b> +/- 0.001		<b>2.83</b> +/- 0.01
	<b>Te—Ge</b>	<b>0.90</b> +/- 0.1	<b>0.006</b> +/- 0.001	<b>4.83</b> +/- 0.89	<b>2.60</b> +/- 0.02
	<b>Te—Sb</b>	<b>1.10</b> +/- 0.11	<b>0.007</b> +/- 0.001		<b>2.81</b> +/- 0.01

In table 3-7, the R and  $\sigma$  are consistent with values expected for covalent bonding, and these values are self consistent from respective edges, i.e.  $R_{\text{Sb-Te}} \approx R_{\text{Te-Sb}}$  despite being allowed to vary independent of each other. The  $R_{\text{Ge-Ge}}$  for 227 was less than expect for a ...-Te-Ge-Ge-Te-... as observed previously, indicating that the nature of homopolar Ge-Ge

bonding has changed in this system. Further analysis is required to confirm this. The values for coordination (N) reflect the bonding fraction percent of each bond type at the respective edges. Uncertainties in coordination reflect both the uncertainty in the fitted bond fraction, and  $S_0^2$ . The best fits to the Sb edge data included Sb-Ge bonds, in addition to Sb-Te bonds. The fraction of Sb-Ge bonds decreased with increasing Te concentration (from 25% in 224 to only 7% in 226 and 227), implying that Sb-Te bonding became more probable. As a result of the small fraction of Sb-Ge bonds, as well as the similarity of the Sb and Te backscatters, our Ge edge fits for 226 and 227 indicated that no Ge-Sb bonds were present. The absence of Ge-Sb bonds from the Ge edge of 226 and 227 is also consistent with the approximately 10-20% error typically reported in N.

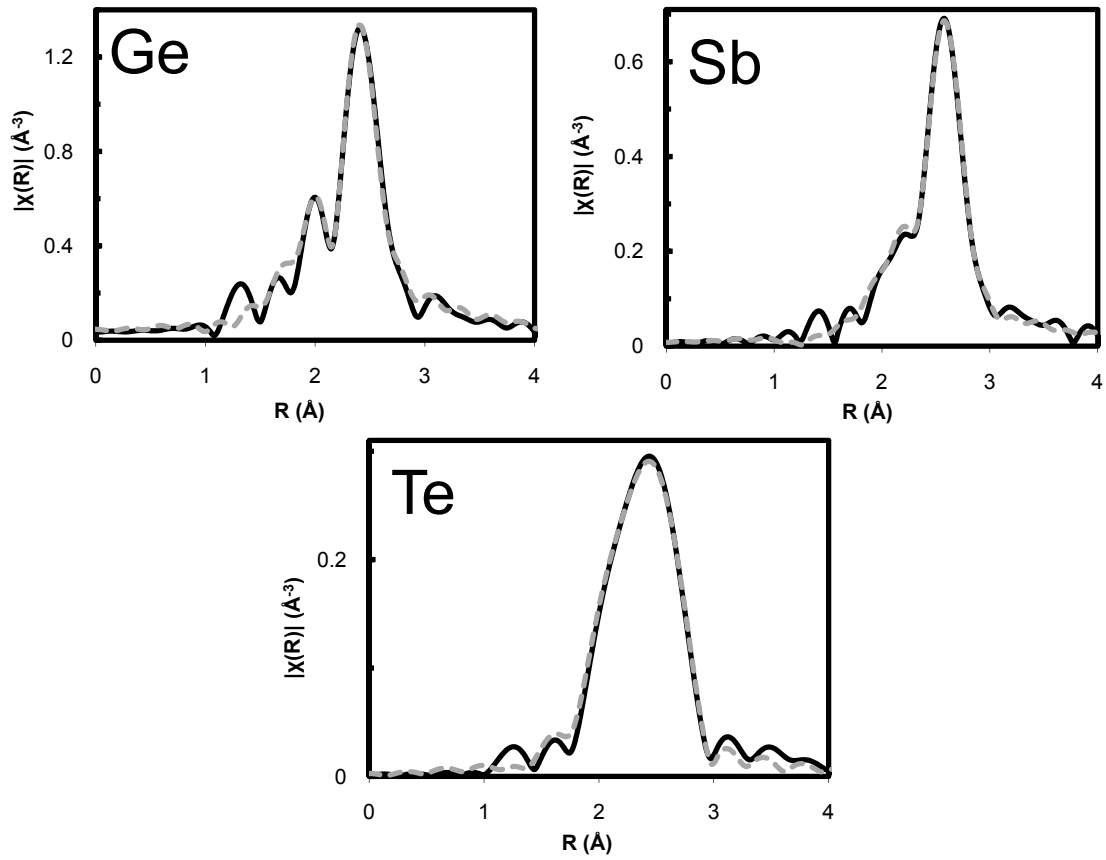


Figure 3-20: Fits to the Ge, Sb, and Te K edge for amorphous 225. Fit quality is representative of those obtained for 224, 226, and 227. Magnitude of the complex Fourier transformed of EXAFS spectra is shown. Solid black line = data, gray dashed line = fit.

Figure 3-21 illustrates the Ge edge bonding behavior of these samples. As Te increases, the fraction of Ge-Te bonds increases, while Ge-Sb bonds become less likely. The observation by Baker et al, of ...-Te-Ge-Ge-Te-...bonding structures, and the prevalence of ~15% of Ge-Ge homopolar bonding in 225 seems justified [134].

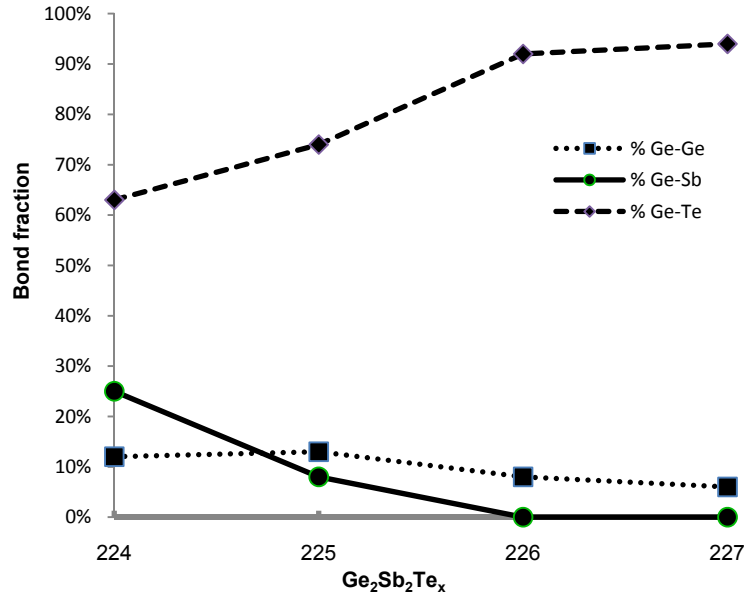


Figure 3-21: The Ge edge bond fractions for  $\text{Ge}_2\text{Sb}_2\text{Te}_x$  samples.

While the similarity of Ge-Te and Ge-Sb backscattering makes a quantitative analysis difficult, there are new methods of distinguishing these based on the electronic structure of Ge-Sb-Te encoded in the near edge. During X-ray absorption, immediately following the promotion of a core electron, there is a strong perturbation of the molecule accompanied by significant electronic effects [135]. First, the valence electrons relax significantly to compensate for the presence of the positive core hole. The departing photoelectron can interact with these relaxing electrons, and lose kinetic energy in the process, thus forcing the system into an excited state (a process called shake-up). In some cases, the excitation may result in the ejection of low energy outer shell electrons from the atom (a process called shake-off) [136]. The energy of the photoelectrons, which emerge from shake-up processes is similar to the energy of photoelectrons released during outer shell ionization [137].

We recently showed that the presence of Ge-Sb bonds in 224 can be isolated in the Ge near edge spectra in light of inelastic losses, i.e. shake-up / shake-off effects based on near edge features at separated by energy spacings corresponding to the photoelectrons released by shake-up processes [138]. This publication is included as an appendix.

Comparing the Ge XANES edge spectra of  $\text{Ge}_2\text{S}_2\text{Te}_x$  alloys to other binary compounds containing Ge-Te and Ge-Sb bonds (e.g. a-GeTe and 15:85) provides a way to discriminate between shake-off XANES features associated with Ge, Sb or Te core levels. This ongoing study demonstrates the spectral differences between GeTe and GeSb features that can provide further insight into bonding arrangement differences in amorphous and crystalline Ge-Sb-Te alloys.

## Chapter 4 Conclusions

The main IR absorption features of N-GST at 770 and 720  $\text{cm}^{-1}$  which scales with N concentration, is the asymmetric stretching mode; it confirmed the preferential bonding of N to three Ge neighbors in a  $\text{Ge}_3\text{N}$  skeletal structure. This preferential Ge-N bonding was also seen in Ge  $2p_{3/2}$  XPS showing a shift in binding energy in 5%N-GST (1218.25) as compared to GST (1217.5) and no similar shifts in the Sb and Te 3d peaks. N-GST near edge spectra vs N at% showed a feature just after the absorption edge which clearly scales as a function of nitrogen atomic concentration, and was correlated to Ge-N bonding in the system.

Subsequent modeling and analysis of the EXAFS data showed that there is both a significant Ge-N first shell, and Ge-N-Ge second shell contribution, to the Ge local structure. The bond fraction of this nitride environment increased as the N at. % increased, accounting for 32%, 44% and 48% of the Ge environment of 2.5, 5, and 6.1%N-GST, respectively. The remaining Ge environment consisted of tetrahedral bonded Ge-Ge, Ge-Te, and Ge-Sb, which obeyed the 8-N rule of covalent bonding. Preferential Ge-N bonding in the N-GST local structure, in the limit where all N is bonded to three Ge neighbors, is characterized by strong repulsions from interactions between the N lone pair  $p\pi$  orbital and the next nearest neighbors. These repulsions, the resulting planar N local structure, and the strong Ge-N covalent bonding, are likely the main driving forces behind the observed grain size reduction and refinement in annealed N-GST films. In-situ, time resolved XRD measurements of 0, 2.5, 5, and 6.1%N-GST samples confirmed that N doping leads to smaller crystallites and a delayed transition from the amorphous phase. XAFS of 5%N-GST after differing anneal conditions allowed us

to see the appearance of rocksalt related features in the near edge, and understand the changes in the amorphous phase during crystallization: the germanium nitride local structure of Ge-N and Ge-N-Ge bonding is not changed by crystallization, while the fraction of tetrahedral Ge-Ge and Ge-Te bonds were replaced by octahedral Ge-Te long bonds associated with a distorted NaCl structure. Finally, an XAFS analysis of 300°C annealed 0, 2.5, 5, and 6.1%N-GST, showed clear long range order associated the next nearest neighbor paths in the distorted Ge-Te rocksalt local structure. These were not changed by doping, except for the drop in amplitude of these contributions, which is consistent with a reduction in grain size and refinement: the N does not enter the crystal lattice but remains in a separate phase on the grain boundary.

EXAFS studies of  $\text{Ge}_x\text{Sb}_{(1-x)}$  ( $x=0.75, 0.50, 0.25, 0.15, 0.07$ ) thin film compounds at the Ge and Sb edges, reveal that a fraction of Ge-Sb bonds were present as-deposited, which scales with the composition 'x'. However, as observed in XRD, the EXAFS local structure of all samples annealed to 400°C consisted of separate Ge and Sb crystalline phases. The crystallization behavior of Sb, characterized by resonant bonding in its local and medium range structure, likely prevents Ge-Sb bonding in the Sb rhombohedral lattice. This was confirmed from fits to the Ge edge of 300°C annealed  $\text{Ge}_{15}\text{Sb}_{85}$ , which conformed well to a model of amorphous, tetrahedral mixture of Ge-Sb and Ge-Ge bonds. Studies of  $\text{Ge}_{15}\text{Sb}_{85}$  and  $\text{Ge}_{50}\text{Sb}_{50}$  plus 10 and 20% Te addition showed distinctly different outcomes. In the as-deposited samples, there were more Ge-Te bonds observed in the 15:85+Te local structure, while Te bonded mainly to Sb in the 50:50+Te system. Consequently, upon annealing, there

was formation of NaCl rocksalt like local structure in the XAFS of the 15:85+Te samples, as well as an absence of the previously observed Ge precipitation in the XRD. On the other hand, the 50:50+Te samples showed Ge precipitation and Ge crystalline phase segregation in the XAFS and the XRD (as seen in the undoped 50:50 sample). We saw that the 50:50 + 33% Te sample was a special case in which there were significantly more Ge-Te bonds in the as-deposited sample, and the subsequent formation of the distorted rocksalt structure upon annealing, as seen in XAFS and in-situ XRD. We saw from a multi-edge refinement of as-deposited thin films of  $\text{Ge}_2\text{Sb}_2\text{Te}_x$  ( $x=4, 5, 6, 7$ ), that there are Ge-Sb bonds still present in  $\text{Ge}_2\text{Sb}_2\text{Te}_4$  and  $\text{Ge}_2\text{Sb}_2\text{Te}_5$ , although we could not model the small Ge-Sb bond fraction in  $\text{Ge}_2\text{Sb}_2\text{Te}_6$  and  $\text{Ge}_2\text{Sb}_2\text{Te}_7$ . EXAFS modeling of these compounds is made difficult due the similar backscattering of Ge-Sb and Ge-Te. The presence of Ge-Sb bonds in 224 can be isolated in the Ge near edge spectra in light of inelastic losses, i.e. shake-up / shake-off effects based on near edge features separated by energy spacings corresponding to the photoelectrons released by shake-up processes.

In our Journal of Applied Physics paper (in preparation) shown in appendix 3, an N-GST etch process consisting of a high bias  $\text{Ar}/\text{CHF}_3/\text{Cl}_2$  etch chemistry was found to result in good vertical profiles with acceptable resist budget and process window. However, detailed analysis of etch exposed material indicates that a resultant etch induced modification layer exists and has significant implications for device performance. In situ XRD data shows that the transition from the FCC to HCP phase is delayed as a result of the etch modification layer, and this is likely due to formation of an oxide which desorbs at the HCP crystallization

temperature. Depth profiled XPS further indicates that this layer consists of mainly germanium oxide and antimony oxide. Laser reflectivity data also reveals that the modification layer hinders nucleation in the optical device by reducing the crystallization speed significantly and is suspected to be a result of the altered interfacial properties with the surrounding dielectric medium. These results were further confirmed by XAFS of partially and fully etch films. XAFS results revealed the nature of the etch modification region resulting from fluorocarbon and chlorine etch chemistries, to consist of significant amorphous  $\text{GeO}_2$  and  $\text{Sb}_2\text{O}_3$ . The volatility of the chlorine etch chemistry is highlighted, since all the Sb was removed from this sample.

## References

- [1] S.R. Ovshinsky. *3271591* U.S Sept. 1966.
- [2] S.R. Ovshinsky Phys. Rev. Lett 1968, Vol. 21, pp. 1450–1453.
- [3] T. Ohta J. Optoelectron.Adv.Mater 2001, Vol. 3, pp. 609–626.
- [4] J. Maserjian. 6, J. Vac. Sci. Technol 1974, Vol. 11, pp. 996–1003.
- [5] S. Hudgens and B. Johnson. 2004, Vol. 29, 11, pp. 829–832.
- [6] S. Raoux, M. Salinga, J. L. Jordan-Sweet, and A. J. Kellock, J. Appl. Phys 2007, Vol. 101, p. 044909.
- [7] E. A. Joseph, T. D. Happ, S.-H. Chen, S. Raoux, et al Symp. VLSI-Technology Systems and Applications, 2008. pp. 142-143.
- [8] C. Cabral, Jr L. Krusin-Elbaum, J. Bruley, S. Raoux, V. Deline, A. Madan, and T. Pinto, Appl. Phys. Lett 2008, Vol. 93, p. 071906.
- [9] B. Streetman. *Solid State Electronic Devices, 3rd Ed* Prentice Hall, 2000.
- [10] A. Pirovano, A. L. Lacaita, A. Benvenuti, F. Pellizzer, and R. Bez., 3, IEEE Trans. Electr. Devices, 2004, Vol. 51, pp. 452–459.
- [11] J.J. Kim, K. Kobayashi, E. Ikenaga, M. Kobata, S. Ueda, T. Matsunaga, K. Kifune, R. Kojima, and N. Yamada, Phys. Rev. B, 2007, Vol. 76, p. 115124.
- [12] T. Kato and K. Tanaka Jpn. J. Appl. Phys 2005, Vol. 44, p. 7340.

- [13] H. Horii, J. H. Yi, J. H. Park, Y. H. Ha, I. G. Baek, S. O. Park, Y. N. Hwang, S. H. Lee, Y. T. Kim, K. H. Lee, U-In Chung, and J. T. Moon,. Kyoto, Japan : Digest of Technical Papers, 2003 Symposium on VLSI, June 2003.
- [14] S. J. Ahn, Y. J. Song, C. W. Jeong, J. M. Shin, Y. Fai, et al. San Francisco, CA : IEEE Int. Electron Devices Meeting, Dec 2004.
- [15] S. L. Cho, H. Horii, J. H. Park, J. H. Yi, B. J. Kuh, Y. H. Ha, S. O. Park, H. S. Kim, U. I. Chung, and J. T. Moon,. Balzers, Liechtenstein : European Symposium on Phase Change and Ovonic Science, Sept 2004.
- [16] Y. C. Chen, H. P. Chen, Y. Y. Liao, H. T. Lin, L. H. Chou, J. S. Kuo, P. H. Chen, S. L. Lung, and R. Liu,. Hsinchu, Taiwan, : Int. Symp. on VLSI Technology, Systems and Applications, Proc. of Techn. Papers Oct. 2003. p. 32.
- [17] B. J. Kuh, Y. H. Ha, J. H. Yi, S. L. Cho, J. H. Park, H. Horii, S. O. Park, H. S. Kim, Y. T. Kim, J.-B. Park, U.-I. Chung, and J. T. Moon,. San Francisco, CA : IEEE Int. Elec. Devices Meeting, Dec. 2004.
- [18] N. Matsuzaki, K. Kurotsuchi, Y. Matsui, O. Tonomura, et al IEDM Tech. Dig 2005.
- [19] H. Seo, T.-H. Jeong, J.-W. Park, C. Yeon, S.-J. Kim, and S.-Y. Kim,. 1, Jpn. J. Appl. Phys 2000, Vol. 39, p. 745.
- [20] T. H. Jeong, M. R. Kim, H. Seo, J. W. Park, and C. Yeon,. 1, Jpn. J. Appl. Phys 2000, Vol. 39, p. 2775.
- [21] I. Friedrich, V. Weidenhof, W. Njoroge, P. Franz, and M. Wuttig, J. Appl. Phys 2000,

Vol. 87, p. 4130.

- [22] T. Wagner, J. Orava, J. Prikryl, T. Kohoutek, M. Bartos, and M. Frumar, *Thin Solid Films*, 2009, Vol. 517, pp. 4694–4697.
- [23] S.-H. Lo, D. A. Buchanan, Y. Taur, and W. Wang, *IEEE Int. Elec. Lett.*, 1997, Vol. 18, pp. 209-211.
- [24] S. Raoux, G. W. Burr, M. J. Breitwisch, C. T. Rettner, Y.-C. Chen, et al *IBM J. Res. & Dev* 2008, Vol. 52, pp. 4-5.
- [25] Y. C. Chen, C. T. Rettner, S. Raoux, G. W. Burr, S. H. Chen, R. M. Shelby, M. Salinga, et al. San Francisco, CA, : International Electron Devices Meeting, Dec. 2006, pp. 777–780.
- [26] L. Krusin-Elbaum, C. Cabral, Jr K. N. Chen, M. Copel, D. W. Abraham, et al *Appl. Phys. Lett* 2007, Vol. 90, p. 141902.
- [27] C. Cabral, Jr K. N. Chen, L. Krusin-Elbaum, and V. Deline, *Appl. Phys. Lett* 2007, Vol. 90, p. 051908.
- [28] D. Krebs, S. Raoux, C. T. Rettner, R. M. Shelby, G. W. Burr and M. Wuttig, 1072-G06-07, *Mar. Res. Soc. Proc* 2008, Vol. 1072.
- [29] S. Raoux, C. Cabral, Jr L. Krusin-Elbaum, J. L. Jordan-Sweet, K. Virwani, M. Hitzbleck, M. Salinga, A. Madan, and T. L. Pinto, *J. Appl. Phys* 2009, Vol. 105, p. 064918.
- [30] T. Nonaka, G. Ohbayashi, Y. Toriumi, Y. Mori, and H. Hashimoto, *Thin Solid Films*, ,

- 2000, Vol. 370, pp. 258–261.
- [31] A.V. Kolobov, P. Fons, A. Frenkel, A. Ankudinov, J. Tominaga, and T. Uruga, *Nature Materials*, 2004, Vol. 3, p. 703.
- [32] F.M. Mirabella. *Internal Reflection Spectroscopy, Theory and Applicaitons*. New York : Marcel Decker, 1993.
- [33] N. J. Harrick. *Internal Reflection Spectroscopy*. New York : Wiley-Interscience, 1967.
- [34] G. Lucovsky, J. Yang, S.S. Chao, et. al *Phys. Rev. B*, 1983, Vol. 28, p. 3234.
- [35] A.R. Zanatta and I. Chambouleyron *Phys. Rev. B*, 1993, Vol. 48, p. 4560.
- [36] I. Chambouleyron and A.R. Zanatta *J. Appl. Phys* 1998, Vol. 84, p. 1.
- [37] J.C. Remy, Y. Pauleau,. 9, *Inorg. Chem* 1976, Vol. 15, pp. 2308-2310.
- [38] L. Chun-rong, S. Zhao-Qi, X. Jing-Zhou, X. Zheng, *J. Phys. D: App Phys* 1998, Vol. 24, p. 2215.
- [39] G. Lucovsky *Solid State Commun* 1979, Vol. 29, p. 571.
- [40] A.L. Smith and N.C. Angelotti *Spectrochem. Acta*, 1959, Vol. 15, p. 412.
- [41] H. Wieder, M. Cardone, and C.R. Guarnieri, *Phys. Status Solidi B*, 1979, Vol. 92, p. 99.
- [42] T.S. Shi, S.N. Sahu, G.S. Oehrlein, et al *Phys. Status Solidi A*, 1982, Vol. 74, p. 329.
- [43] J.A. Taylor, G.M. Lancaster, J.W. Rabalais, *J. Electron Spectrosc. Relat. Phenom* 1978, Vol. 13, p. 435.

- [44] S. Evans Surf. Interface Anal 1985, Vol. 7, p. 299.
- [45] M.C. Jung, Y.M. Lee, H.-D. Kim, et al. 083514, Appl. Phys. Lett 2007, Vol. 91.
- [46] B.K. Agarwal. *X-ray Spectroscopy*. Heidelberg : Springer-Verlag, 1979. p. 215.
- [47] D.E. Sayers, E.A. Stern, F.W. Lytle, Phys. Rev. Lett 1971, Vol. 27, p. 1204.
- [48] D.E. Sayers and B.A. Bunker. [ed.] D. Koningsberger and R. Prins. *Chemical Analysis*. New York : John Wiley and Sons, 1988, Vol. 92, 6, pp. 443–571.
- [49] E.A. Stern. 8, Phys. Rev. B, 1974, Vol. 10, p. 3027.
- [50] C.A. Ashley and S. Doniach Phys. Rev. B , 1975, Vol. 11, p. 1279.
- [51] P.A. Lee and J.B. Pendry Phys. Rev. B, 1975, Vol. 11, p. 2795.
- [52] G.G. Li, F. Bridges, and C.H. Booth, Phys. Rev. B, 1995, Vol. 52, pp. 6332-6348.
- [53] J.J. Rehr and R.C. Albers Phys. Rev. B, 1990, Vol. 41, pp. 8139–8149.
- [54] J.J. Rehr, J. Mustre de Leon, S.I. Zabinsky, and T.C. Albers, J. Am. Chem. Soc 1991, Vol. 113, p. 5135.
- [55] D. Ehle. MRCAT Home Page. *MRCAT*. [Online] 10 19, 2005 . [Cited: 10 10, 2009.] <http://mrcat.iit.edu/>.
- [56] B. Ravel. Community/X23A2-xafs.org. *xafs.org*. [Online] 11 12, 2009. [Cited: 11 17, 2009.] <http://xafs.org/Community/X23A2>.
- [57] M. Newville, P. Livins, Y. Yacoby, J. J. Rehr, and E. A. Stern, Phys. Rev. B, 1993, Vol. 47, p. 14126.

- [58] B. Ravel and M. Newville J. Synchrotron Radiat 2005, Vol. 12, pp. 537-541.
- [59] M. Newville J. Synchrotron Rad 2001, Vol. 8, p. 322.
- [60] S. I. Zabinsky, J. J. Rehr, A. Ankudinov, R. C. Albers, and M. J. Eller, Phys. Rev. B, 1995, Vol. 52, p. 2995.
- [61] C. Bull, P. F. McMillan, J. Itié, and A. Polian, Phys. Stat. Sol. (A), 2004, Vol. 201, pp. 909–916.
- [62] F. Boscherini, A. Filipponi, S. Pascarelli, F. Evangelisti, S. Mobilio, F. C. Marques, I. Chambouleyron, Phys. Rev. B , 1989, Vol. 39, p. 8364.
- [63] S. N. Ruddlesden and P. Popper Acta Cryst. , 1958, Vol. 11, pp. 465-468.
- [64] J. Stohr. *X-Ray Absorption: Principles, Applications, Techniques of EXAFS, SEXAFS, and XANES*. New York : John Wiley and Sons, 1988, Vol. 92, 10, pp. 443-571.
- [65] E.A. Stern and S.M. Heald. Basic Principles and Applications of EXAFS. [ed.] E.E. Koch. *Handbook of Synchrotron Radiation*. New York : North-Holland, 1983, pp. 995-1014.
- [66] J.J. Rehr, C.H. Booth, F. Bridges, and S.I. Zabinsky, Phys. Rev. B, 1994, Vol. 49, p. 12347.
- [67] C. deBoor. *A Practical Guide to Splines*. New York : Springer-Verlag, 1978.
- [68] J.W. Cook Jr. and D.E. Sayers J. Appl. Phys. , 1981, Vol. 52, p. 5924.
- [69] S. Kelly, D. Hesterberg, B. Ravel. *Methods of Soil Analysis. Part 5*. Madison, WI : Soil Science Society of America, 2008, Vol. 5, p. 387.

- [70] D.A. Baker, M.A. Paesler, G. Lucovsky, S.C. Agarval, and P.C. Taylor, Phys. Rev. Lett 2006, Vol. 96, p. 255501.
- [71] F.A. Cotton, G. Wilkinson, and P.L. Gaus., *Basic Inorganic Chemistry*. 2nd. New York : J. Wiley, 1987.
- [72] S. Makler, G. M. Rocha, and E. V. Anda, Phys. Rev. B, 1990, Vol. 41, p. 5857.
- [73] R.W.G. Wyckoff. *Crystal Structures*. New York : Wiley, 1964. Vol. 2.
- [74] R. Marchland, Y. Laurent, J. Lang, and M. Bihan,. 1969 : Acta Crystallogr. B, Vol. 35, p. 2157.
- [75] J. Robertson. 2, Philos. Mag. B, 1981, Vol. 44, pp. 215-237.
- [76] A.R. Zanatta and I. Chambouleyron Phys. Status Solidi B, 1996, Vol. 193, p. 399.
- [77] J. Robertson Philos. Mag. B, 1991, Vol. 63, p. 47.
- [78] A. Frenkel, E.A. Stern, A. Voronel, et al. 17, Phys. Rev. B, 1994, Vol. 49, p. 11662.
- [79] E.A. Stern, M. Newville, B. Ravel, Y. Yacoby, D. Haskel, Physica B, 1995, Vol. 208 & 209, pp. 117–120.
- [80] Y. Maeda and M Wakagi. 1, Jpn. J. Apply. Phys 1991, Vol. 30, p. 101.
- [81] A. Filipponi, P. Fiorini, F. Evangelisti, and S. Mobilio, Mat. Res. Soc. Symp. Proc 1987, Vol. 95, p. 305.
- [82] Spaepen, G.S. Cargill III and F J. Non-Crystalline Solids, 1981, Vol. 43, pp. 91-97.
- [83] T. Maeda, T. Yasuda, M. Nishizawa et al Appl. Phys. Lett 2004, Vol. 85, p. 3181.

- [84] G.B. Stephenson Nucl. Instr. Meth. Phys. Res. A , 1988, Vol. 266, p. 447.
- [85] G.B. Stephenson, K.F. Ludwig, Jr J.L. Jordan-Sweet, S. Brauer, et al Rev. Sci. Instrum 1989, Vol. 60, p. 1537.
- [86] L.A. Clevenger, R.A. Roy, C. Cabral, Jr K.L. Saenger, et al J. Mater. Res 1995, Vol. 10, p. 2355.
- [87] C. Lavoie, C. Cabral, Jr L.A. Clevenger, J.M.E. Harper, et al Mater. Res. Soc. Symp. Proc 1996, Vol. 406, p. 163.
- [88] R.M. Shelby, S. Raoux, J. Appl. Phys 2009, Vol. 105, p. 104902.
- [89] I. Friedrich, V. Weidenhof, W. Njoroge, P. Franz, M. Wuttig. 9, J. Appl. Phys Vol. 87, p. 4130.
- [90] C. Kittel. *Introduction to Solid State Physics*. 7th. New York, Chichester : John Wiley & Sons, 1996. p. 17.
- [91] T. Nonaka, G. Ohbayashia, Y. Toriumib, Y. Morib, H. Hashimotob, Thin Sol. Films, 2000, Vol. 370, pp. 258-261.
- [92] J.S. Washington et al Mater. Res. Soc. Symp 2009, Vol. 1160, pp. H13-08.
- [93] Y.J. Park, J.Y. Jong, Y.T. Kim, Appl. Surf. Sci 2005, Vol. 252, pp. 8102-8106.
- [94] D. Turnbull, J.C. Fisher, J. Chem. Phys 1949, Vol. 17, p. 71.
- [95] R. Becker, W. Doring, Ann. Phys. (Leipzig!), 1935, Vol. 24, p. 719.
- [96] H.B. Singh, A. Holz, Solid State Commun 1983, Vol. 45, p. 985.

- [97] K.F. Kelton *J. Non-Cryst. Solids*, 1993, Vol. 163, p. 283.
- [98] S. Senkader and C.D. Wright. 2, *J. Appl. Phys* 2004, Vol. 95, p. 504.
- [99] N. Yamada and T. Matsunaga *J. Appl. Phys* 2000, Vol. 88, pp. 7020–7028.
- [100] A. Bianconi. [ed.] D.C. Koningsberger and R. Prins. *X- Ray Absorption* John Wiley and Sons, 1988, 11, p. 573ff.
- [101] A.V. Kolobov, P. Fons, J. Tominaga, A.I. Frenkel, A.L. Ankudinov, T. Uruga. 1, *J. Ovonic Res* 2005, Vol. 1, pp. 21-24.
- [102] S. Calvin, M.M. Miller, R. Goswami, et al. 1, *J. Appl. Phys* 2003, Vol. 94, p. 778.
- [103] A. Frenkel, C.W. Hills, and R.G. Nuzzo. 51, *J. Phys. Chem. B*, 2001, Vol. 105, p. 12689.
- [104] Y.G. Yoo et al *Materials Science and Engineering A*, 2007, Vol. 449, pp. 627–630.
- [105] S.M. Sze. *Semiconductor Devices: Physics and Technology*. New York : John Wiley and Sons, 1985. pp. 7-8.
- [106] A.C. Scheinost, A. Rossberg, D. Vantelon, I. Xifra, et al *Geochimica et Cosmochimica Acta*, 2006, Vol. 70, pp. 3299–3312.
- [107] J. M. Durand, P. E. Lippens, J. Olivier-Fourcade, J. C. Jumas and M. Womes, *J. Non-Cryst. Solids*, 1996, Vol. 194, pp. 109–121.
- [108] K. Terashima, T. Hashimoto, T. Uchino, S. Kim and T. Yoko, *J. Ceram. Soc. Jpn* 1996, Vol. 104, pp. 1011–1017.

- [109] D.A. Baker. *EXAFS Studies of Ge-Sb-Te Alloys for Phase-Change Applications*.  
Raleigh : North Carolina State University, 2007. pp. 1-103. Doctoral Dissertation.
- [110] N. Mott Adv. Phys 1967, Vol. 16, pp. 49-144.
- [111] P. Jovari et al Phys. Rev. B , 2008, Vol. 77, p. 035202.
- [112] D.C. Bobela and P.C. Taylor Mater. Res. Soc. Symp 2008, Vol. 1072, pp. G02-06.
- [113] C. Cabral, Jr et al. 071906, Appl. Phys. Lett 2008, Vol. 93.
- [114] Z. Tan, S.M. Heald, M. Rapposch, C.E. Bouldin, and J.C. Woicik, Phys. Rev. B, 1992,  
Vol. 46, p. 9505.
- [115] R.W. Olesinski and G.J. Abbaschian Bull. Alloy Phase Diagrams, 1986, Vol. 7, p. 219.
- [116] B.C. Giessen, and C. Borromee-Gautier, J. Solid State Chem 1972, Vol. 4, pp. 447-  
452.
- [117] K.A. Agaev and A.G. Talybov Sov. Phys. Crystallogr 1966, Vol. 11, p. 400.
- [118] I.I. Petrov, R.M. Imamov, and Z.G. Pinsker, Sov. Phys. Crystallogr 1968, Vol. 13, p.  
339.
- [119] J. Goldak, C.S. Barrett, D. Innes, W. Youdelis, J. Chem. Phys 1966, Vol. 44, p. 3323.
- [120] T. Anderson and H. Krause Acta Crystallogr Sect. B, 1974, Vol. 30, p. 1307.
- [121] T. Matsunaga, N. Yamada, and Y. Kubota, Acta Crystallogr. B, 2004, Vol. 60, p. 685.
- [122] T. Matsunaga and N. Yamada. 10, Phys. Rev. B, 2004, Vol. 69, p. 104111.
- [123] I. Friedrich, V. Weidenhof, W. Njoroge, P. Franz, and M. Wuttig,. 9, J. Appl. Phys

2000, Vol. 87, p. 4130.

- [124] C.S. Barrett, P. Cucka, and K. Haefner, *Acta Cryst* 1963, Vol. 16, p. 451.
- [125] L. Pauling. *Nature of Chemical Bond*. New York : Cornell Univ. Press, 1939.
- [126] K. Shportko, S. Kremers, M. Woda, D. Lencer, J. Robertson and M. Wuttig, *Nature Mater* 2008, Vol. 7, pp. 653-658.
- [127] F.A. Cotton and G. Wilkinson. *Advanced Inorganic Chemistry*. 3rd. New York : Interscience Publishers, 1972. p. 117 (Table 3.4). Chap. 3.
- [128] S. Raoux, R. M. Shelby, J. Jordan-Sweet, B. Munoz, M. Salinga, Y.-C. Chen, Y.-H. Shih, E.-K. Lai, and M.-H. Lee, *Microelectronic Engin* 2008, Vol. 85, p. 2330.
- [129] D.C. Bobela and P.C. Taylor *Jpn. J. Appl. Phys* 2008, Vol. 47, p. 10.
- [130] D.A. Baker, M.A. Paesler, G. Lucovsky, P.C. Taylor, *J. Non. Cryst. Sol* 2007, Vol. 353, p. 1713.
- [131] N. Yamada, E. Ohno, K. Nishiuchi, N. Akahira, and M. Takao. 5, *J. Appl. Phys* 1991, Vol. 69, p. 2849.
- [132] P. Fons, D. Brewes, E. Stern, A.V. Kolobov and J. Tominaga, *Mater. Res. Soc. Symp. Proc* 2006, Vol. 918, pp. 0918-H04-01.
- [133] R.T. Sanderson. *Chemical Bonds and Bond Energy*,. 3rd. New York : Academic Press, 1976. pp. 60-63. Chap. 3.
- [134] D.A. Baker, M.A. Paesler, G. Lucovsky, S.C. Agarval, and P.C. Taylor, *J. Non-Cryst. Solids*, 2006, Vol. 352, p. 1621.

- [135] K. Siegbahn, C. Nordling, G. Johansson, et al. *ESCA applied to free molecules*. . North Holland, Amsterdam : s.n 1969.
- [136] P. Persson, S. Lunell, A. Szöke, B. Ziaja, and J. Hajdu, *Protein Science*, 2001, Vol. 10, pp. 2480–2484.
- [137] Y. Nakayama, P. Persson, S. Lunell et. al, *J. Vac. Sci. Technol. A*, 1999, Vol. 17, pp. 2791–2799.
- [138] G. Lucovsky, J.S. Washington, L. Miotti, and M.A. Paesler, *Jour. Non Crys. solids*. (submitted), 2009.
- [139] S-M. Yoon et al. 27, *Jpn. J. Appl. Phys* 2005, Vol. 44, pp. L 869–L 872.
- [140] *X-ray Absorption Fine Structure—XAFS13*. S. Kelly and B. Ravel. [ed.] B. Hedman and P. Pianetta Amer. Inst. of Phys. CP882.
- [141] L. Pauling *J. Am. Chem. Soc* 1932, Vol. 54, p. 3570.
- [142] M. Avrami *J. Chem. Phys* 1941, Vol. 9, p. 177.
- [143] V. Weidenhof, I. Friedrich, S. Ziegler, and M. Wuttig,. 6, *J. Appl. Phys* , 2001, Vol. 89, pp. 3168-3176.
- [144] N. Ohshima *J. Appl. Phys* 1996, Vol. 79, p. 8357.
- [145] K. Prabhakaran, T. Ogino, F. Maeda, and Y. Watanabe,. 16, *Appl. Phys. Lett* 2000, Vol. 76, p. 2244.
- [146] D. Schmeisser, R.D. Schnell, A. Bogen, F.J. Himpsel, D. Rieger, G. Landgren, and J.F. Morar, *Surf. Sci* 1986, Vol. 172, p. 455.

- [147] O. Majerus, L. Cormier, D.R. Neuville, L. Galois, G. Calas, *J. of Non-Crys. Sol* 2008,  
Vol. 354, pp. 2004-2009.
- [148] R. B. Gregor, F.W. Lytle, J. Kortright, A. Fischer-Colbrie, *J. Non. Crys. Solids*, 1987,  
Vol. 89, pp. 311-325.

## Appendices

# Appendix 1 - An Introduction to EXAFS Theory

J.S. Washington

Department of Physics, North Carolina State University  
(In partial fulfillment of Quantum Mechanics second semester course)

X-ray absorption fine spectroscopy (XAFS) is one of few atomic probing techniques available for use in non-crystalline and highly disordered materials. In addition, it has also achieved wide spread recognition due to its ease of measurement, sample versatility, and “tunability” (its ability to probe specific elements in a sample by selecting the appropriate incident photon energy) [1]. In practical terms, XAFS is divided into X-ray Absorption Near-Edge Spectroscopy (XANES) and Extended X-ray Absorption Fine Structure (EXAFS), depending on our measurement with respect to the absorption edge. This paper will provide an introduction to the foundations and practicality of EXAFS, as well as show a simple quantum mechanical description of EXAFS Theory. Although we will highlight the experimentally determined variables of the derived EXAFS equation, we will not discuss EXAFS data analysis here.

## Introduction

There are currently very few structural probes available allowing scientists to probe the local structure of non-crystalline or highly disordered materials. X-ray Absorption Spectroscopy (XAFS) is one such technique whose quantum mechanical explanation in terms of interference effects has been known since the 1930's [1]. It was over the past three decades however, that XAFS has emerged as a very useful discerning probe of the local structure around selected atomic species in solids, liquids, and molecular gases [2]. The technique's popularity has been fueled by two major occurrences, the first being the refinement by Stern, Sayers, and Lytle of the essential physics of the XAFS process into the standard XAFS equation and their proposal of a simple method of data analysis [3]. The second major event, whose own development directly parallels that of XAFS, has been the availability of high energy-resolution synchrotron radiation sources; these provide scientists with a ready source of high energy, tunable, high flux x-ray photons.

In the x-ray energy regime, light is absorbed by matter through the photoelectric effect; an x-ray photon is absorbed by an electron in a tightly bound core level (1s or 2p). If the x-ray energy is less than the electron's binding energy, the electron is not perturbed from its defined quantum state and the x-ray is not absorbed. If the x-ray energy is equal to or greater than the binding energy of the electron, the probability that

the electron is moved from its quantum level is very high; the x-ray is destroyed (absorbed) and any excess energy is given to a photo-electron ejected into a continuum state. XAFS is the structure we observe in the absorption (as a function of energy) spectra, when an x-ray is absorbed by an atom at its core-electron's binding energy. As we see in Figure 1, XAFS is the modulation of the atom's x-ray absorption probability due to the chemical and physical state of the atom.

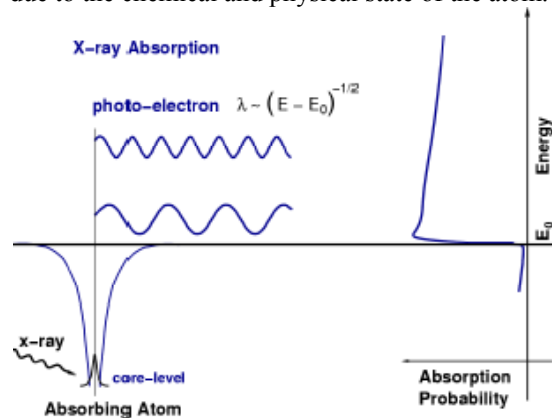


FIG 1: Diagram of x-ray absorption through the photoelectric process. When an x-ray has the energy of a tightly bound core electron level,  $E_0$ , the probability of absorption has a sharp rise.

XAFS spectra are especially sensitive to the formal oxidation state, coordination chemistry, and the bond distances, coordination number and species of

the atoms immediately surrounding the selected element [4]. There is very little constraint on samples that can be measured with XAFS – all atoms have core-level electrons, plus crystallinity is not a prerequisite. In fact, XAFS has found widespread use in various fields including biology [5], environmental science [6], catalysts research, and material science [7]. It should be noted, there are some practical constraints when XAFS is done in practice; these depend on conditions of the synchrotron source and the experimental station or beamline, such as energy range, beam size, and available intensity.

### Typical Experimental Setup and Measurement

Typical XAFS experiments can be performed in either transmission or fluorescence mode, though transmission is more common. Figure 2 shows the typical setup of a beamline [1].

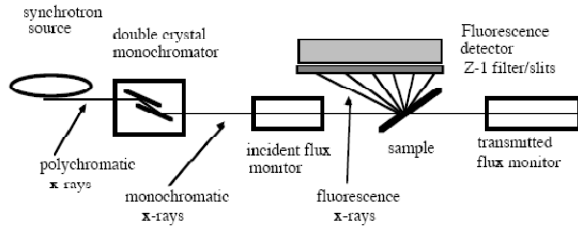


FIG 2: Schematic of a typical XAFS experimental setup.

Polychromatic x-rays from the synchrotron radiation source or bremsstrahlung in a conventional laboratory source, tuned to a selected core-electron energy band of approximately 1 eV bandwidth, is selected by diffraction from a silicon double crystal monochromator. Only those x-ray photons that are of the correct wavelength  $\lambda$  ( $\lambda = \hbar c / E$ , where  $\hbar$  is Planck's constant and  $c$  is the speed of light) to satisfy the Bragg condition  $n\lambda = 2d \sin \theta$  at the selected angle  $\theta$  will be reflected from the first crystal; the others are absorbed [1]. A parallel second crystal restores the incident beam to its original direction. The sample in question is exposed to these monochromatic x-rays, and the incident and transmitted x-rays are monitored using gas ionization chambers. For a uniform sample of thickness  $x$ , we can measure the absorption coefficient  $\mu(E)$ , which obeys

$$I_t = I_o e^{-\mu(E)x} \quad (1)$$

where  $I_t$  is the intensity of the radiation field after transmission and  $E$  is the x-ray energy.  $\mu(E)$  is also related to the density of the sample  $\rho$

( $g/cm^3$ ) and the total attenuation cross section  $\sigma_T$  ( $cm^2/g$ ) by

$$\mu(E) = \rho \sigma_T \approx \frac{\rho Z^4}{AE^3} \quad (2)$$

$$\rho \sigma_T \approx \sum_i \rho_i \sigma_i = \rho \sum_i \left( \frac{m_i}{M} \right) \sigma_i$$

where the sum is over the elements  $i$  in the sample of mass fraction  $\left( \frac{m_i}{M} \right)$ . The strong dependence of

$\mu(E)$  on  $Z$  (the atomic number) and  $E$  is a fundamental property of x-rays.  $\mu(E)$  decreases as energy increases  $\left( \frac{1}{E^3} \right)$  except at the absorption

edge, where it peaks rapidly. Figure 3 shows the XAFS spectra for FeO showing the absorption edge, and some rapidly oscillating structure above the absorption edge.

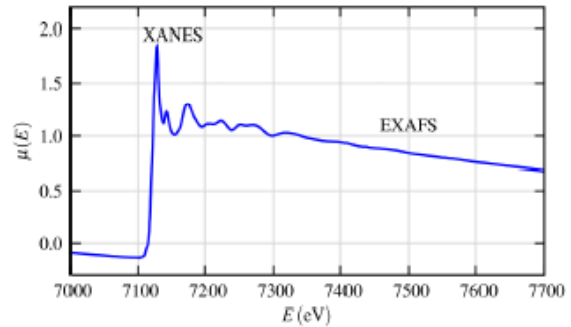


FIG 3: XAFS spectra for FeO showing XANES and

EXAFS. It is best to think of this absorption edge as a transition of an electron from a bound state (1s) to some higher state (or continuum). In the near edge region, sometimes called the X-ray Absorption Near-Edge Structure (XANES), transitions may occur to unfilled bound states, nearly-bound states (resonances), or continuum states of the appropriate symmetry. Well above the absorption edge ( $\geq 30$  eV), is the Extended X-ray Absorption Fine Structure (EXAFS) region,

transitions are to continuum states. Although the physics for both regions is the same, we see that XANES is strongly sensitive to the formal oxidation state and coordination chemistry (e.g. octahedral, tetrahedral coordination) of the absorbing atom, while EXAFS is more sensitive to bond distances, coordination number, and species of the neighbors of the absorbing atom.

As the name suggests, in EXAFS we are interested in the fine, rapid oscillations in the energy range far above the absorption edge. We define the EXAFS fine structure function as  $\chi(k)$  where

$$\chi(k) = \frac{\mu(E) - \mu_o(E)}{\Delta\mu_o(E)} \quad (3)$$

As we see in figure 4 below,  $\mu_o(E)$  represents the smoothly varying portion of  $\mu(E)$  past the absorption edge, corresponding to the absorption coefficient of a free atom while  $\Delta\mu_o(E)$  represents the jump in the absorption at the threshold energy,  $E_o$ .

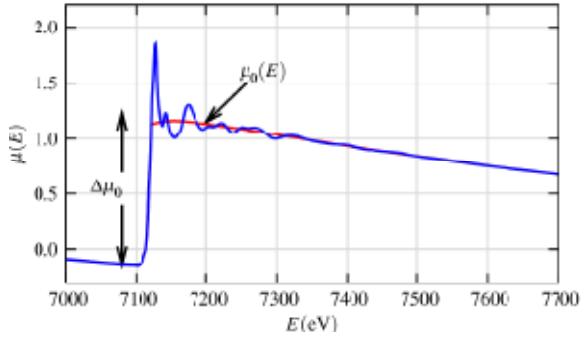


FIG 4: XAFS spectra for FeO showing smooth background

### Simple Theoretical Description of EXAFS

EXAFS is best described in terms of the wave behavior of the photo-electron created in the absorption process [13]. Thus, the x-ray energy is conveniently described by the photoelectric wave vector:

$$k = \sqrt{\left(\frac{2m_e}{\hbar^2}\right)(E_{\text{photon}} - E_o)} \quad (4)$$

where  $E_o$  is the threshold energy of the absorption edge and  $m_e$  is the electron mass. As mentioned

before, x-ray absorption is a transition from an initial state  $|i\rangle$  (core-electron, incoming x-ray, no photo-electron) to a final state  $|f\rangle$  (core-hole, photo-electron, no x-ray). Consequently, we can represent the absorption probability  $\mu(E)$  using Fermi's Golden's Rule [8], with the square of the transition matrix element ,

$$\mu(E) = |\langle f|H|i\rangle|^2 \quad (5)$$

where  $H$  is the interaction term to be determined. Since the core-level electron is very tightly bound to the absorbing atom; the initial state will not be altered by the presence of a neighboring atom. The final state, on the other hand, will be affected by the neighboring atom because the photo-electron will be able to see it (recall we assume the photo-electron is an expanding wave). If we expand  $|f\rangle$  into two pieces, one that is the "bare atom" (idealized single atom) portion  $|f_o\rangle$ , and one that is the effect of the neighboring atom  $|\Delta f\rangle$ , we obtain

$$|f\rangle = |f_o\rangle + |\Delta f\rangle \quad (6)$$

Expanding the absorption coefficient in terms of the new wave function for  $|f\rangle$ , we obtain:

$$\mu(E) \propto |\langle i|H|f_o\rangle|^2 \times \left[ 1 + \langle i|H|\Delta f\rangle \frac{\langle f_o|H|i\rangle}{|\langle i|H|f_o\rangle|^2} + C.C \right] \quad (7)$$

where  $C.C$  means complex conjugate. Notice that this expression resembles our expression in (3):

$$\mu(E) = \mu_o(E)[1 + \chi(E)] \quad (8)$$

Comparing (7) and (8), we see that

$$\mu_o(E) = |\langle i|H|f_o\rangle|^2 \quad (9)$$

is the "bare atom absorption" – it is the ideal case of a single atom without neighboring atoms. We see also that the fine structure  $\chi(E)$  (oscillating term) corresponds to

$$\chi(E) \propto \langle i|H|\Delta f\rangle \quad (10)$$

We are now ready to classify the interaction term. With a semi-classical approach to EXAFS, we represent the incoming photon as an electromagnetic

field, and the scattered electron quantum mechanically. Taking the Hamiltonian for the classical radiation field,

$$H = \frac{\vec{P}^2}{2m_e} + e\phi(\vec{x}) - \frac{e}{m_e c} \vec{A} \cdot \vec{p} \quad (11)$$

we can treat the  $-\frac{e}{m_e c} \vec{A} \cdot \vec{p}$  term as the time

dependent perturbation term, where  $A$  is the quantized vector potential (we omitted the  $[\vec{A}]^2$  term, since this does not contribute to absorption) [9]. This reduces to a term that is proportional to  $e^{ikr}$  [10]. The initial state in (10) is a tightly bound core-level, which we can approximate by delta function (a 1s level for atomic

number  $Z$  extends to approximately  $\frac{a_o}{Z}$ , where  $a_o$

is the Bohr radius of  $\approx 0.529 \text{ \AA}$ ). The change in final state,  $|\Delta f\rangle$  is just the wave-function of the scattered

photo-electron,  $\psi_{scatt}(r)$ . Putting all these terms together, we get a simple expression for the EXAFS:

$$\chi(E)\alpha \int dr \delta(r) e^{ikr} \psi_{scatt}(r) = \psi_{scatt}(0) \quad (12)$$

This is a fundamental result; it tells us that EXAFS is proportional to the amplitude of the scattered photo-electron at the absorbing atom. If we take the outgoing scattered photoelectron to be a spherical wave, we can write:

$$\psi_{scatt}(k, r) = \frac{e^{ikr}}{kr} \quad (13)$$

If the photo-electron wave travels a distance  $R$  to a neighboring atom, scatters from it, and travels back to the original absorbing atom via a spherical wave, we get (by simply multiply all these factors together):

$$\chi(k)\alpha \psi_{scatt}(k, r=0) = \frac{e^{ikr}}{kR} \times [2kf(k)e^{i\delta(k)}] \frac{e^{ikr}}{kR} + C.C. \quad (14)$$

where  $f(k)$  and  $\delta(k)$  are scattering factors that depend on the atomic number of the neighboring atom. We combine these and include the complex conjugate to ensure we end up with a real function to obtain:

$$\chi(k) = \frac{f(k)}{kR^2} \sin[2kR + \delta(k)] \quad (15)$$

We have only considered scattering from a single nearest neighbor to this point. In actuality, there will be multiple scattering effects as we average over the millions of neighboring atom pairs in the sample. Even assuming that the sample is homogenous, we will have some thermal and static disorder in the bond distances will give a range of distances that will affect the XAFS. Taking this into consideration, we get:

$$\chi(k) = \frac{Ne^{-2k^2\sigma^2} f(k)}{kR^2} \sin[2kR + \delta(k)] \quad (16)$$

where  $N$  is the coordination number and  $\sigma$  is the mean-square-displacement in the bond distance  $R$ . This treatment (as well as others) is explained in more detail by Sayers, Stern, and Lytle [11]. In real systems, we usually have more than one type of neighboring atom around a particular absorbing atom. We account for this very easily in our formalism by summing over the contributions from each scattering atom type (or *coordination shell*),

$$\chi(k) = \sum_j \frac{N_j e^{-2k^2\sigma_j^2} f_j(k)}{kR_j^2} \times \sin[2kR_j + \delta_j(k)] \quad (17)$$

where  $j$  is the sum over the individual coordination shell of identical atoms at approximately the same distance from the central atom. As a final correction to equation (17), recall that in our expression for the outgoing photo-electron spherical wave, we neglected to account for the fact that the wave can scatter inelastically. Also, the wave must scatter elastically and return before the end of the core-hole is filled. The following expression is a dampened wave function, which takes these considerations into account by introducing a mean free path  $\lambda(k)$ :

$$\psi_{scatt}(k, r) = \frac{e^{ikr} e^{-2r/\lambda(k)}}{kr} \quad (18)$$

Now the final EXAFS equation looks like:

$$\chi(k) = \sum_j \frac{N_j e^{-2k^2\sigma_j^2} e^{-2R_j/\lambda(k)} f_j(k)}{kR_j^2} \times \sin[2kR_j + \delta_j(k)] \quad (19)$$

Thus, we have obtained the well known EXAFS equation. Though it appears somewhat intractable, the EXAFS equation allows us to determine  $N$ ,  $R$ , and  $\sigma^2$  knowing the scattering amplitude  $f(k)$  and phase shift  $\delta(k)$ .

### Conclusion

X-ray absorption fine spectroscopy (XAFS) is an fundamental atomic probing technique in widespread usage due to its ease of measurement, sample versatility, and its ability to probe specific elements in a sample by selecting the appropriate incident photon energy. We described a typical experimental setup and differentiated between the two flavors of XAFS – XANES and EXAFS – who both share the same physical origin, but have separate interpretation. Finally, we were able to show that the EXAFS spectra were derived from the oscillatory part of the expression for the absorption coefficient and to use some basic assumptions to derive the famous EXAFS equation.

### References

- 1) *Elements of XAFS*, Grant Bunker, Physics Department, Illinois Institute of Technology Chicago, Illinois
- 2) For a broad review of XAFS, see the book *X-ray Absorption*, D.C. Koningsberger and R. Prins, eds, John Wiley and sons, NY, (1989)
- 3) D.E. Sayers, E.A. Stern, and F.W. Lytle, Phys. Rev. Lett. 27, 1204 (1971)
- 4) *Fundamentals of XAFS*, Matt Newville, Consortium for Advanced Radiation Sources
- 5) E. C. Theil, M. A. Brown, and D. E. Sayers, *J. Biol. Chem.* 254, 8132 (1979).
- 6) Z. Wang, D. Hesterberg, W. Zhou, D. E. Sayers, and W. P. Robarge. “Extended X-ray Absorption Fine Structure Study of Mercury Speciation in a Flood Plain Soil” in *Contaminated Soils: Third International Conference on the Biogeochemistry of Trace Elements - 1995*, edited by R. Prost, colloque 85, INRA Editions, Paris, France, 1998.
- 7) D. A. Baker, M. A. Paesler, G. Lucovsky, S. C. Agarwal, and P.C. Taylor, 2006, Phys. Rev. Lett. 96, 255501
- 8) P.A.M. Dirac, *The Principles of Quantum Mechanics*, fourth edition, Oxford at the Clarendon Press, 1981
- 9) J. Sakurai, *Modern Quantum Mechanics*, Addison-Wesley, 1994
- 10) J.W. Cooper, *Photoionization from Outer Atomic Subshells. A Model Study*, Phys. Rev. 128; 2:681-693, (1962).
- 11) D.E. Sayers, F.W. Lytle, and E.A. Sterns, in *Advances in X-Ray Analysis*, edited by B.L. Henke, J.B. Newkirk, and G.R. Mallett (Plenum, New York, 1970) Vol. 13, p. 248
- 12) C.A. Ashley and S. Doniach, 1975, Phys. Rev. B 11, 1279

## Appendix 2 - Experimental Details

XAS measurements were performed at MRCAT beamline ID-10 at the Advanced Photon Source (APS) at Argonne National Laboratory, in Argonne, IL as well as NIST beamline X23A2 at the National Synchrotron Light Source (NSLS), Brookhaven National Laboratory, in Upton, NY. The primary difference between MRCAT and X23A2 is the insertion device utilized to generate the synchrotron radiation. X23A2 employs a wiggler, which is a series of bending magnets concatenated together with radiation intensity proportional to  $N$ , the number of magnetic poles. Since the period and the strength of the magnetic field are not tunable to the frequency of radiation produced by the electrons, every electron in the electron bunch radiates independently, resulting in broad spectrum. On the other hand, MRCAT uses an undulator, where magnetic poles can be tuned so that the radiation produced by the oscillating electrons interferes constructively with the motion of other electrons, causing the radiation spectrum to have a relatively narrow bandwidth. The intensity of radiation is proportional to  $N^2$ , and thus we typically obtain much higher incident flux and brilliance at MRCAT. More details on the physical differences between undulators and wigglers can be found at D. T. Attwood's webpage at Berkeley: Soft X-Rays and Extreme Ultraviolet Radiation (<http://ast.coe.berkeley.edu/sxreuv/>, accessed and verified May 10, 2010).

We will now compare the monochromator, harmonic X-ray elimination method, and detector specifications (ionization chambers, solid-state detectors, filters, fill gases) for MRCAT@APS and X23A2@NSLS.

### Monochromator

The monochromator selects the Bragg angle  $\theta$  for the desired photon energy. This is the angle between the face of the first crystal and the propagation vectors of the incident X-rays. An XAFS energy scan is thus achieved by rotating the monochromator through the appropriate angle. The second crystal follows the first, remaining essentially parallel, to re-diffract the single energy beam in a direction parallel to the broad energy spectrum.

According to the MRCAT website [[http://mrcat.iit.edu/mrcat\\_instrumentation.html](http://mrcat.iit.edu/mrcat_instrumentation.html)], the ID-10 line uses:

“a Si (111) monochromator consisting of a cryo-cooled first crystal designed by the [Illinois Institute of Technology] Center for Synchrotron Radiation Research and Instrumentation (CSRRI) and a 250mm long second crystal which provides an energy range of 4.8keV to 30keV from the fundamental reflection. Both crystals have been chemically polished and have been measured to deliver the theoretical photon flux to the

experimental station. The second crystal has a piezoelectric tuning actuator with a.c. feedback and a Bragg-normal motion which permits some degree of fixed offset operation.”

In practice, this beamline routinely achieves energies of up to 35keV. The resolution of the monochromator is  $\Delta E/E = 1 \times 10^{-4}$  [MRCAT website]. From the X23A2 website [<http://www.nsls.bnl.gov/beamlines/beamline.asp?blid=X23A2>], X23A2 uses:

“...upwards reflecting, fixed exit Golovchenko-Cowan design; piezo-feedback stabilized, Si(311) monochromator” with energy range 4.9– 30 keV, energy resolution  $2 \times 10^{-4}$ , and beam profile 25mm x 1.0mm. The typical flux is  $10^{10}$  ph/sec (@ monochromator bandpass @ 10 keV, 100mA, 2.5 GeV).

## Harmonic Rejection

The Ge K edge (11103 eV) will diffract, according to Bragg's Law, both the fundamental harmonic ( $k=1$ ) as well as the third harmonic ( $k=3$ ). The 3<sup>rd</sup> harmonic, with energies  $\sim 33309$  in this case, increases the probability that Sb or Te photoelectrons will be excited, to the detriment of Ge absorption spectrum.

Both the X23A2 and MRCAT beamlines use a 60cm long flat harmonic rejection mirror with Pt or Rh coatings. This mirror resides in the experimental station and may be moved vertically in or out of the beam as the experiment requires. Alternatively, we can slightly rotate the second crystal of the monochromator from the optimal  $\theta$  where detuning enough to reduce the fundamental harmonic by half can all but eliminate the 3<sup>rd</sup> harmonic.

## Detectors

We used ion chambers at X23A2 and MRCAT. Figure 1 shows the typical setup of a beamline [from *Elements of XAFS*, Grant Bunker, Physics Department, Illinois Institute of Technology Chicago, Illinois ], illustrating the ion chambers.

An ion chamber measures beam intensity indirectly. For fluorescence measurements, we used a 3 grid or 5 grid, Stern-Heald, ion chamber fluorescence detector. X-rays passing through the detector interact with the gas(es) contained therein to produce fast photoelectrons, Auger electrons, and/or fluorescence photoelectrons. These interactions cause gas ionization, so when a voltage is applied to the chamber, the ions and electrons are drawn apart prior to recombination. The resulting voltage is proportional to the number of photons absorbed. This proportionality is not always linear, but given the proper gases and applied voltage, linearity can be achieved over the energy range of the EXAFS scan, typically between 800 eV and 1300 eV above the absorption edge.

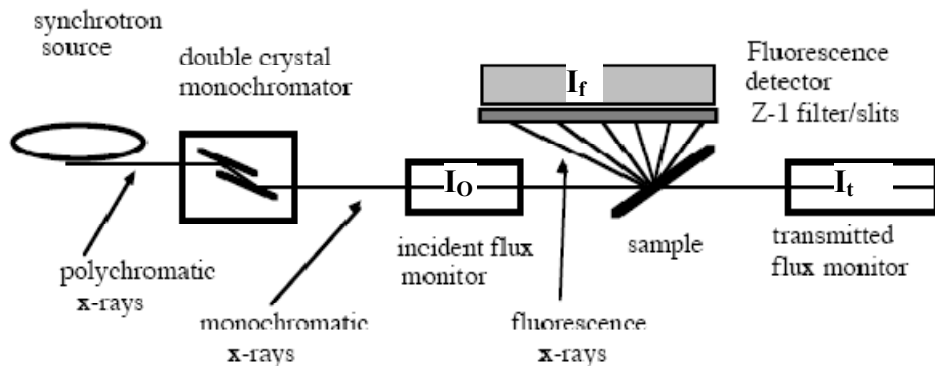


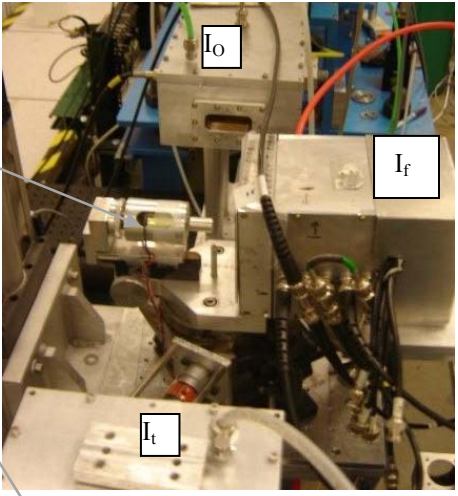
FIG 1: Schematic of a typical XAFS experimental setup. Reference ionization chamber not shown.

Around the absorption energy of germanium's K edge, 11103 eV, an ion chamber 30 cm long containing only nitrogen will absorb about 8% of the photons passing through it. This is ideal for an  $I_0$  chamber, where enough photons are absorbed to give a signal, yet the bulk of the beam impinges on the sample. Sixty percent argon and 40% nitrogen fills the  $I_t$  (or  $I_f$ ) and  $I_{ref}$  chambers, resulting in about 75% absorption. The higher absorption energies of antimony and tellurium require a mixture of 15% krypton to 85% nitrogen for the  $I_0$  chamber and 100% krypton for the  $I_t$  (or  $I_f$ ) chamber. The signals from these chambers are collected and saved in a text file on the control computer for later analysis.

### Sample Geometry

Thin film samples deposited on bare Si wafers were measured in grazing incidence on a rotating stage, in fluorescence measurements. The rotating stages, as seen below, distribute the sharp diffraction peaks which may be excited in the bare Si wafer, evenly throughout the entire absorption spectrum as background noise. Both stages rely on inexpensive motors which tend to vibrate while they spin; these slight vibrations actually improve the process of disrupting / smearing bragg reflections coming from the Si substrate.

Rotating Sample Holder



# Appendix 3 – (JAP in preparation) Characterizing the Effects of Etch-Induced Material Modification on the Crystallization Properties of Nitrogen Doped $\text{Ge}_2\text{Sb}_2\text{Te}_5$

J. S. Washington<sup>2</sup>, E. A. Joseph<sup>1</sup>, S. Raoux<sup>1</sup>, J. L. Jordan-Sweet<sup>1</sup>, D. Miller<sup>3</sup>, H-Y. Cheng<sup>4</sup>, A. G. Schrott<sup>1</sup>, C-F. Chen<sup>4</sup>, R. Dasaka<sup>1</sup>, B. Shelby<sup>3</sup>, G. Lucovsky<sup>2</sup>, M. A. Paesler<sup>2</sup>, L. Miotti, H-L. Lung<sup>4</sup>, Y. Zhang<sup>1</sup> and C. H. Lam<sup>1</sup>

<sup>1</sup>IBM T.J. Watson Research Center, <sup>2</sup>Physics Department, North Carolina State University, <sup>3</sup>IBM Almaden Research Center, <sup>4</sup>Macronix International Co Ltd.

The chemical and structural effects of processing on the crystallization of nitrogen doped  $\text{Ge}_2\text{Sb}_2\text{Te}_5$  is examined via X-ray photoelectron spectroscopy (XPS), X-ray absorption spectroscopy (XAS), time resolved laser reflectivity and time resolved X-ray diffraction (XRD). Time resolved laser reflectivity and XRD show that exposure to various etch and ash chemistries significantly reduces the crystallization speed, while the transition temperature from the rocksalt to the hexagonal phase is increased. XPS and XAS attribute this to the selective removal and oxidization of N, Ge, Sb, and Te, thus altering the local bonding environment to the detriment of device performance.

## INTRODUCTION

Current metal oxide semiconductor field effect transistors (MOSFETs) and floating gate transistors, which are the fundamental building blocks of existing flash and DRAM memory technology, begin to suffer from reduced device performance when scaling beyond the 22nm node. As an example, quantum mechanical modeling has projected a gate oxide scaling limit of 20 Å before which chip standby power will become excessive due to electron tunneling currents [1]. The scalability of Phase Change Memory (PCM) however, seemingly suffers no physical limitations into the next 3-4 lithography generations making it a very attractive alternative to current memory technology [2]. For example, 3nm doped eutectic Ge-Sb PCM bridge prototype memory cells have been recently reported [3]. Accomplishing such scaling using standard CMOS processing however, requires high fidelity sublithographic patterning in order to maintain tight process control. Previous work has demonstrated the ability to pattern  $\text{Ge}_2\text{Sb}_2\text{Te}_5$  (GST) films using both chlorine and fluorine based etch chemistries in a reactive ion plasma, but profile flaws such as undercutting and tapering resulted [4]. Nitrogen doped GST (N-GST) device structures similarly resulted in significant tapering and undercutting in reactive chemistries due to the high volatility of N-GST in halogen etch chemistries, as shown in figure 1. However, vertical profiles with acceptable resist budget and process window were

obtainable. Despite this fact, the optimized Ar/CHF<sub>3</sub>/Cl<sub>2</sub> etch chemistry was found to have a chemically driven, 10nm thick, N-GST etch modification layer, characterized by selectively volatilized antimony and nitrogen along with an increased amount of oxidized germanium, antimony, and tellurium [5].

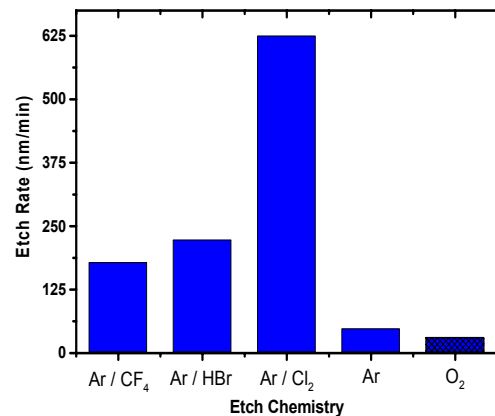


FIG. 1: Etch rate of N-GST in various halogen based etch chemistries.

In this work, we examine the chemical and structural effects of this etch modification layer and its implications for device performance and crystallization, using XPS, X-ray absorption fine spectroscopy (XAFS), time resolved laser reflectivity and time resolved X-ray diffraction (XRD).

## EXPERIMENT

100 nm N-GST and GST films were deposited by DC reactive sputtering a GST compound target in a mixture of argon and nitrogen feedgas chemistries. The bulk N atomic percent (at%) was either 0 at% (GST) or 5 at% (N-GST), as confirmed by Rutherford Backscattering Spectrometry (RBS) and Particle Induced X-ray Emission (PIXE). Figure 2 shows the structure of experimental samples. The single layer samples comprised 100nm of GST or N-GST sputter deposited on Si wafers and subsequently etched. Here, there were two categories: films that were “fully-etched” (FE) back to a thickness of 15-25nm or, those “partially-etched” (PE) to 80-90nm. The 100nm N-GST film in the tri-layer was deposited over 30nm films of Al<sub>2</sub>O<sub>3</sub> on Si, and etched back to a thickness of ~30nm, briefly exposed to air, and capped with a low temperature oxide (LTO).

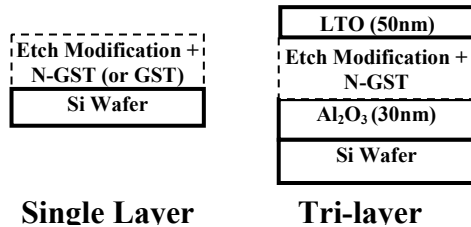


FIG. 2: Structures of samples for a) single layer films and b) tri-layer films for laser characterization and recrystallization.

Reactive Ion Etch (RIE) utilized an inductively coupled LAM 9400 plasma system operated at a frequency of 13.56MHz. The FE single layer films were separately etched in plasma of Ar/CHF<sub>3</sub>/Cl<sub>2</sub>, Ar/Cl<sub>2</sub>, and Ar/CF<sub>4</sub> etch chemistries in order to compare the etch modification created by each. The PE single layer films and N-GST in the tri-layer films were etched using Ar/CHF<sub>3</sub>/Cl<sub>2</sub>. Wafers were electrostatically clamped to the bottom electrode and maintained at a temperature of 60°C during processing, with source power and pressure fixed at 300W and 4mTorr, respectively. Optical Emission Spectroscopy (OES) was used to verify the etch process, to ensure that films were not over-etched.

XPS measurements were performed using a Physical Electronics Quantum 2000 ESCA Microprobe using a monochromatic Al K<sub>a</sub> source with a 200 μm spot size. Charge neutralization (or compensation) is performed as necessary, since a positive charge can accumulate upon electron ejection from low resistance

films (such as as-deposited GST). Depth profiling was done using 1.0 keV Ar<sup>+</sup> ions, 3 x 3 mm raster. High resolution scans (46 eV pass energy; 0.2 eV/step) were taken at a 45° take-off angle between the sample and the analyzer axis.

In-situ, time-resolved, XRD was done at beamline X-20C of the National Synchrotron Light Source using a photon energy of 6.9keV on the partially-etched GST and N-GST single layer films. The setup consisted of a high-throughput synthetic multilayer monochromator and fast linear-diode-array detector [6; 7]. A special chamber for controlling the sample ambient (purified He gas) was outfitted with a BN heater for rapid annealing up to 1200°C at a rate ≤ 35°C/sec [8; 9]. In this work, films were heated at a rate of 1 °C/s, and the intensity of the XRD peaks was recorded over a 2θ range of 15°. The range was selected to cover strong XRD peaks of these materials. From the appearance of the XRD peaks the crystallization temperature was determined.

XAFS measurements were performed at NIST beamline X23A2 [10] at the National Synchrotron Light Source (NSLS), Brookhaven National Laboratory, in Upton, NY. We simultaneously collected fluorescence measurements at the Ge K edge of the sample as well as transmission measurements on a Ge metal reference foil; this allowed us to calibrate and monitor monochromator energy [11] and determine structurally significant shifts in absorption energy. Extended XAFS (EXAFS) spectra were normalized using ATHENA and modeled with ARTEMIS [12]. Both are available as part of IFEFFIT [13], an interactive engine containing the algorithms for fitting theoretical FEFF calculations [14].

Crystallization studies of N-GST [15] utilized two optical testers to study our tri-layer samples. Previously described in ref [15], the “green tester” heats the sample with a pulsed 514 nm laser, produced by gating a continuous wave argon ion laser with an acousto-optic modulator. The pulsed beam is focused to a 1/e<sup>2</sup> diameter of either 1.1 or 2.0 μm depending on optics used, while reflectivity is monitored with a continuous 633 nm laser beam of 1/e<sup>2</sup> diameter of 1.0 μm. The time resolution of the green tester is limited by the pulse rise time of 10 ns. The “red tester” heats with a pulsed diode laser powered by a National Semiconductor LMH6525 laser diode driver. The pulsed heating laser has a wavelength of 658 nm. Reflectivity is monitored with a 630 nm continuous beam, and the time resolution of the tester is around 1 ns. The 1/e<sup>2</sup> diameter of both beams is 0.95 μm. The

laser pulse intensity and reflected probe beam intensity were determined by photodetectors, recorded by a digital oscilloscope, and stored by a computer. The initial and final reflectivities,  $R_i$  and  $R_f$ , were determined by averaging a portion of the data at the beginning before the heating laser pulse and at the end of the trace after the heating laser pulse. The relative change in reflectivity (equation 1),

$$\text{Eq. (1)}$$

was calculated for each pulse. This change in reflectivity was recorded as a function of pulse duration and laser power. To determine the crystallization behavior for melt-quenched amorphous material, samples were initially annealed, prior to etching, at a temperature appropriate to crystallize the film to the rocksalt phase. Laser pulse conditions which melt the film under the most intense part of the laser beam, were then determined by varying laser pulse duration and power. This produced a melt-quenched amorphous region, accompanied by a drop in optical reflectivity, when the film quickly cools after the laser pulse ends. By applying a second pulse of sufficient duration and power at the same location, we verified that the drop in reflectivity characteristic of melting and quenching to the amorphous state is fully recovered by crystallization, giving confidence that the film is not damaged by the melting pulse.

## RESULTS AND DISCUSSION

Depth profiled XPS in figure 3 show atomic fraction comparisons for N-GST films which were unetched, etched in Ar/CHF<sub>3</sub>/Cl<sub>2</sub>, as well as subjected to a dry strip post etch. Atomic fraction was estimated from fitting the area under the XPS peaks for O (and N) 1s, Ge 2p<sub>3/2</sub>, and Sb (and Te) 3d<sub>5/2</sub> and 3d<sub>3/2</sub> peaks to calculate the metal / oxide percentages. This XPS data, shown in figure 3, shows a dramatically different bonding environment is as-deposited versus etched samples. For instance, at a depth of 4nm into the unetched as-deposited film, the Sb metal approximate atomic fraction (at%) is 20%, versus 5% following an etch, and complete Sb removal after an etch & strip. The Sb oxide follows an inverse trend; at 4nm there is no Sb oxide in the as-deposited sample, ~3% in the etched, and ~9% in etch & stripped sample. It is clear from the fraction of Sb-metal removal versus Sb oxide increase, that there is a significant net loss of atomic

Sb. This is also apparent from a comparison of Te bonds at 4nm. An initial fraction of 40% Te as-deposited, decreases to 20% post etch, and 10% post etch & strip, with no corresponding increase in TeO<sub>x</sub>. The nitrogen dopant also suffers a similar behavior, with almost all nitrogen lost from the sample at a 4nm depth.

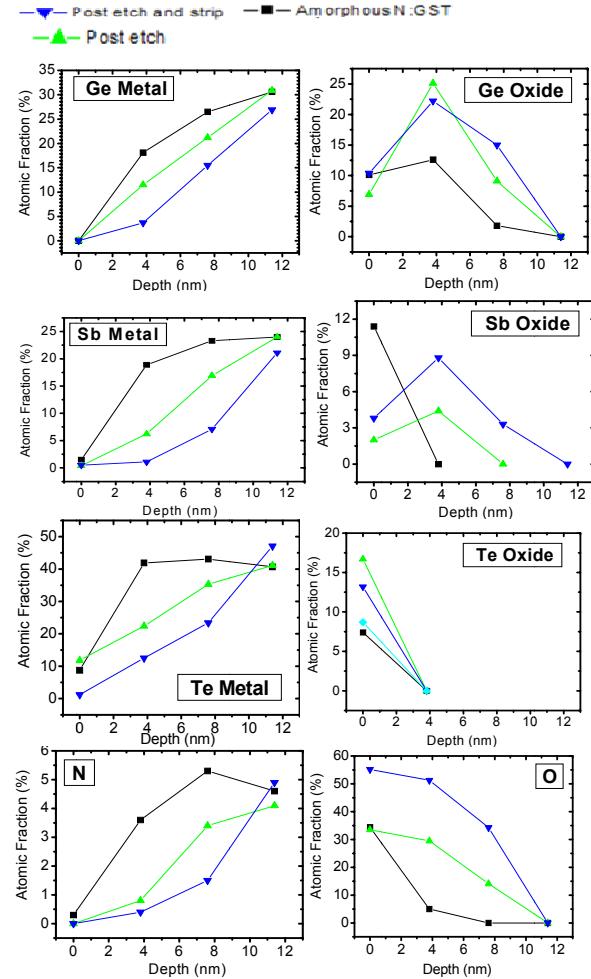


FIG. 3: Depth profiled XPS measurements for various elements of N-GST films. Post etch data follows etching in an Ar/CHF<sub>3</sub>/Cl<sub>2</sub> chemistry. Post etch and strip follows the same etch with an additional dry strip [5].

Unlike Sb, Te, and N, selective volatilization is not as significant in the Ge environment, but rather the presence of oxidation persists. The fraction of Ge metal bonds at 4nm for amorphous, etched, and etch/strip samples decreased as 17% → 10% → 3%, while Ge oxide increased as 12% → 25% → 22%. Ge

has a higher oxygen affinity than Sb [16], and the selective removal of Sb, Te, and N may lead to Ge dangling bonds, leading to more Ge-O bonds and oxygenation after air exposure. This is apparent in the O fraction in the amorphous, etched, and etch & stripped films, which increased as 5% → 30% → 50%.

For a 30nm N-GST tri-layer optical device, the presence of this ~12nm thick etch modification region will have significant effects on the device operation. Figure 4 shows a measure of the corresponding crystallization speed and subsequent fraction of material crystallized for the unetched, etched, etched + wet cleaned, and etch + dry stripped trilayer samples.

Previous laser recrystallization measurements show that the maximum change in reflectivity is associated with full crystallization,

$$\text{Eq. (2)}$$

Normalization according to equation 2 results in a plot of fractional crystallization versus time [15]. Solid lines in fig. 4 are fits to the Johnson–Mehl–Avrami–Kolmogorov (JMAK) function [17], described in equation 3; it can be useful for empirical characterization of crystallization data.

$$\text{Eq. (3)}$$

JMAK is seen regularly in the analysis of crystallization in GST and other phase-change materials [18]. However, it has since been pointed out [19] that JMAK theory insufficiently describes GST laser crystallization experiments, which are far from isothermal conditions and in which non-Arrhenius and inhomogeneous nucleation processes are important.

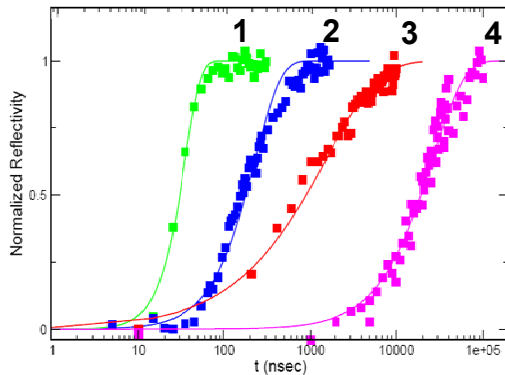


FIG. 4: Fractional crystallization vs laser pulse heating time for N-GST samples etched in Ar/CHF<sub>3</sub>/Cl<sub>2</sub> : 1) unetched 2) etched 3) etched + wet cleaned 4) etched + dry stripped. The solid curves are fits to . The x axis in ln(t).

In figure 4, the unetched sample reached a normalized reflectivity value of 0.5 in 20ns. This crystallization time increased to 175ns, 900ns, and 20,000ns, for the etched, etch + wet cleaned, and etch + dry stripped samples, respectively. Also, compared to the unetched sample, the etched samples did not saturate to a well defined, constant value, indicative of full crystallization, even with prolonged laser heating. From XPS, the significant increase in crystallization time (i.e. decreased nucleation rate), corresponds to an increase in selectively volatilized Sb, Te, and N, as well as, O incorporation. In particular, GeO<sub>x</sub>, SbO<sub>x</sub>, and O concentration increased as unetched → etch → etch + dry strip. It is likely that this oxide layer is acting, in conjunction with the adjacent LTO dielectric to change the crystal growth rate of the N-GST. A high correlation between nucleation rate and the interfacial properties of the adjacent dielectric material in tri-layer GST samples was previously shown [20]. In that work, chemical properties of the surrounding dielectric, such as affinity, rather than physical ones (e.g morphology), lead to inhibited nucleation and more gradual crystallization plots with less defined maximum reflectivity.

Figure 5 shows the XRD intensity vs 2(θ) collected at room temperature, before and after a 450°C ramp for initially amorphous, as-deposited (etched and unetched) samples. In the partially etched films, the appearance of XRD features indexed to the hexagonal phase (HCP) did not appear while the transition from the rocksalt to the hexagonal phase was previously recorded at 400°C [15]. This behavior is independent of the initial phase (amorphous or crystalline), as similar results were observed after a 450°C ramp, in unetched and etched samples initially in the rocksalt metastable phase. The crystallization behavior between 400°C - 500°C depends only on the creation of the etch modified layer, characterized by significant GeO<sub>x</sub> and SbO<sub>x</sub>. It was shown that GeO<sub>x</sub> films created on Ge (100) and (111) wafers via air exposure become unstable at 420°C while at 430°C, complete desorption takes place [21; 22]. Thus, we hypothesize that the thermal instability of the oxide is preventing the formation of the hcp phase.

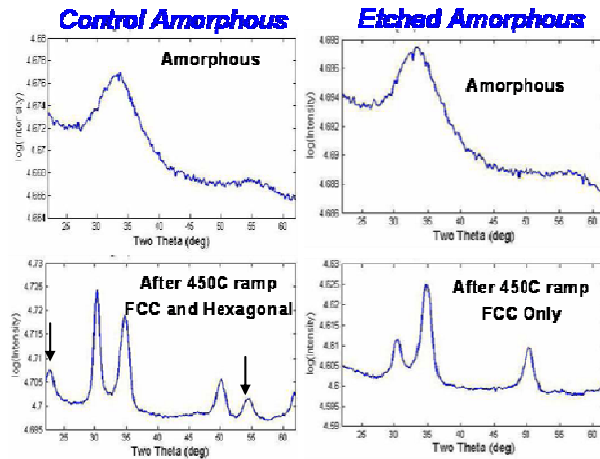


FIG. 5: XRD peak intensity vs ( $2\theta$ ) taken at room temperature before (top row) and after (bottom row) a 450°C ramp for an amorphous, as-deposited, unetched sample (Control Amorphous) and an as-deposited etched sample (Etched Amorphous). The unetched sample showed peaks indexed to both the hexagonal and the FCC phase, while the etch sample showed only rocksalt index peaks. HCP related features indicated with solid black arrows.

In order to understand the structural nature of the etch modification region and interpret the results above, we measured the Ge K edge XAFS spectra of etched and unetched GST and N-GST. The background removal values used in AUTOBK for these samples were:  $\Delta k = [0.0 : 15.05]$ ,  $R_{\text{bkg}} = 1.0$ , pre-edge =  $[-197.1 : -86.5]$ , and post-edge =  $[100 : 862.11]$ . A normalized near edge comparison of the FCC annealed partially etched GST and N-GST, as well as unetched N-GST is shown in figure 6A and the related EXAFS data is shown in figure 6B. The etch related feature in the near edge of the annealed and partially etched GST coincides with a significant low R contribution in the EXAFS. The etch related near edge feature also occurs in a region just after the peak absorption energy, and it overlaps the previously reported germanium nitride related feature [23], as indicated by the black arrow. A direct comparison of the normalized near edge for XANES analysis is appropriate here since the XAFS data for all the partially etched samples were collected under similar fluorescence measurement parameters.

Comparing the near edge data in Figure 6A, the N-GST partially etched sample (black line) could be interpreted as a superposition of the etch related feature in partially etched, undoped GST (gray line) and un-etched N-GST (dashed line). This implies that the observed EXAFS  $|\chi(R)|$  plots of the partially etched, 5%N-GST films in figure 6B contain structural

contributions from both etch induced changes as well as doping in the R space region between 1 and 2Å. From our XPS experiments, we expect that this etch related feature corresponds to germanium oxide. Subsequently, the near edge feature is reminiscent of XANES taken on quartz like and amorphous  $\text{GeO}_2$  films [24], and implies significant  $\text{GeO}_2$  contribution. In order to verify this, we modeled the partially etched, as-deposited amorphous, undoped GST film. We used the unit cell parameters for quartz-like  $\text{GeO}_2$  in ATOMS to generate the high scattering amplitude theoretical paths for 1<sup>st</sup> shell Ge-O, together with the bond contributions for amorphous GST (tetrahedral Ge-Te, and Ge-Ge bonds).

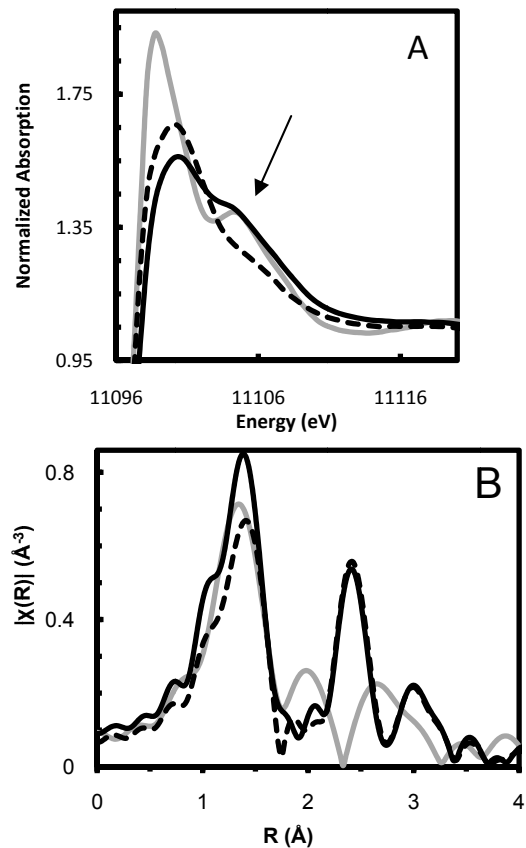


FIG. 6: A) Normalized Ge near edge comparison of FCC annealed, partially etched 0%N-GST (solid gray line), partially etched 5%N-GST (solid black line) and un-etched 5%N-GST (black dashed line) and (B) the associated magnitude of the complex Fourier transformed EXAFS spectra.

The data and the fit are shown in figure 7 (goodness of fit statistics shown in caption), while table 1 shows the fitting results. We were unable to fit

Ge-Sb bonds, possibly due to some Sb depletion, but mainly due to insufficient structural data; this is best accomplished by measuring additional Sb edge data. We also noticed that fits were improved by modeling the multiple scattering paths for next nearest neighbor Ge-Ge path contribution as observed in other GeO<sub>2</sub> EXAFS studies [24]. The low reduced chi square and measurement uncertainty confirms the accuracy of this model. The fit indicates that ~37% of Ge environment of the partially etched 80nm thick film is GeO<sub>2</sub>, which corresponds to significant O observed in the XPS, and may act as a dielectric layer with interfacial properties which inhibits nucleation, and whose thermal properties leading to desorption at HCP crystallization temperatures.

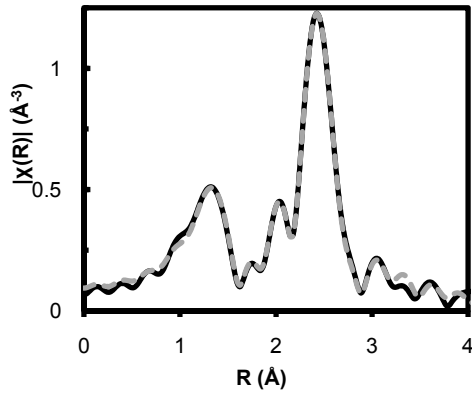


FIG. 7: Fits to the Ge K edge for partially etched, as dep. GST. The magnitude of the complex Fourier transformed of EXAFS spectra is shown. Solid black line = data, gray dashed line = fit. The goodness of fit stats are - N<sub>independent</sub> points: 17.3, N<sub>variables</sub>: 12, Chi-square: 419.97, Reduced chi-square: 79.67, R-factor: 0.006, Measurement uncertainty (R): 0.0009.

TAB. 8: Fitting results for partially etched amorphous GST.

	Bond	% Bond	N	$\sigma^2(\text{Å}^2)$	$\Delta$ Energy (eV)	R (Å)
Oxide	Ge-O	37 +/- 5	2.00 +/- 0.25	0.002 +/- 0.001	3.83 +/- 0.5	1.76 +/- 0.01
	Ge-O		2.00 +/- 0.25	0.002 +/- 0.001		1.76 +/- 0.01
	Ge-Ge		4.0 +/- 0.25	0.015 +/- 0.004		3.20 +/- 0.03
GST	Ge-Ge	63 +/- 5	0.3 +/- 0.2	0.001 +/- 0.001	9.07 +/- 2.0	2.47 +/- 0.02
	Ge-Te		3.7 +/- 0.5	0.006 +/- 0.001		2.61 +/- 0.005

We also studied the structure of the etch modification region by XAFS for fully etched samples in subsidiary etch chemistries. Figure 8 shows the first derivative of the Ge K edge spectra of N-GST for unetched, fluorocarbon etched and chlorine etched samples. The maxima in the derivative of near edge data can be used to identify the absorption edge energy ( $E_0$ ). From the  $E_0$ , the fluorocarbon etched sample is

possibly a structural intermediary between the unetched and chlorine etched N-GST, due to its distinct corresponding near edge features. There is a 5.06eV and 5.53eV shift in the  $E_0$  of fluorine and chlorine etched sample, respectively, as compared to the  $E_0$  of N-GST. Furthermore, the slowly oscillating near edge features of the etched samples are consistent with each other, but distinctly different from the unetched sample. This > 5eV increase in  $E_0$  of the Ge absorbers, and the observed near edge features are identical with previously reported shifts and observed XANES features in amorphous GeO<sub>2</sub>/SiO<sub>2</sub> glasses (a 5.7 eV shift with respect to Ge metal reference was observed) [25].

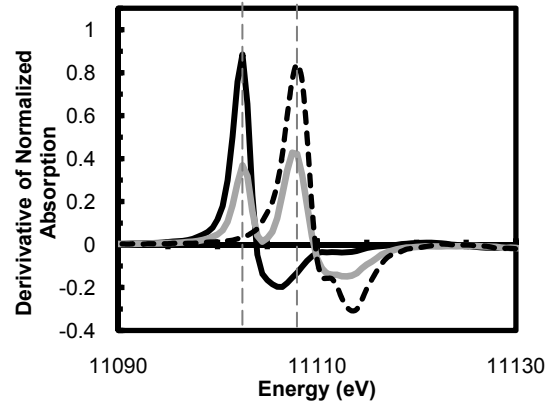


FIG. 8: Derivative of the normalized Ge  $\mu(E)$  near edge of N-GST etch in fluorine (solid gray line), chlorine (dashed black line), and unetched (solid black line). The position of the first maxima of N-GST fluorine etch (1<sup>st</sup> vertical dashed line) corresponds to the shoulder in the  $\mu(E)$  spectrum of N-GST.

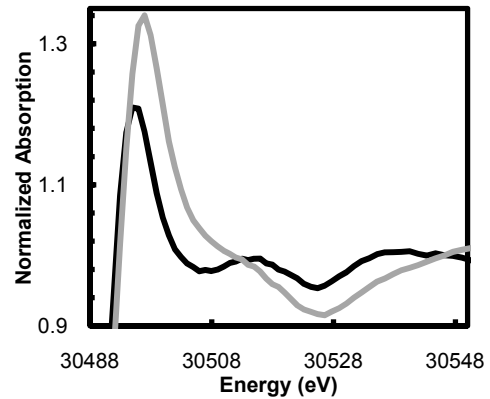


FIG. 9: Normalized Sb near edge comparison of fluorocarbon etched N-GST (solid gray line) and N-GST (solid black line). The slowly varying near edge spectra after the white line is consistent with an Sb-O environment. Absolute  $E_0$  was determined with respect to Sb metal foil, and defined at the maximum of the derivative of  $\mu(E)$ .

The fact that we cannot observe any N-GST related peaks in the chlorine etch sample implies that all the GST related bonds were volatilized by this chemistry. This is seen at the Sb K edge of these samples in figure 9, where no absorption edge was observed in the chlorine etched sample i.e. all the Sb was selectively removed.

The Sb  $E_O$  of fluorocarbon etched N-GST was 30492.01 corresponding to a 1.01eV shift with respect to Sb metal foil, and a 1.08eV shift with respect to N-GST. This  $E_O$  value, coupled with the slowly varying near edge feature after the white line is consistent with a detailed XAFS study by Scheinost *et al.* on various Sb(III), Sb(III,V) and Sb(V) oxides [26]. Their observation that the  $E_O$  of the trivalent oxide was 30493 eV compared to 30497 eV for the pentavalent oxide, shows that the Sb local structure in fluorocarbon etched N-GST is likely an amorphous, trivalent  $Sb_2O_3$ . The presence of unoxidized, unmodified Sb bonds explains why our observed  $E_O$  is  $\sim 1$ eV less than expected. These Ge and Sb EXAFS results demonstrate the high volatility of the chlorine etch chemistry clarifies the local structure of the significant oxide formation that persists post etch.

## CONCLUSIONS

A nitrogen doped GST etch process consisting of a high bias  $Ar/CHF_3/Cl_2$  etch chemistry was found to result in good vertical profiles with acceptable resist budget and process window. However, detailed analysis of etch exposed material indicates that a resultant etch induced modification layer exists and has significant implications for device performance. In situ XRD data shows that the transition from the FCC to HCP phase is delayed as a result of the etch modification layer, and this is likely due to formation of an oxide which desorbs at the HCP crystallization temperature. Depth profiled XPS further indicates that this layer consists of mainly germanium oxide and antimony oxide. Laser reflectivity data also reveals that the modification layer hinders nucleation in the optical device by reducing the crystallization speed significantly and is suspected to be a result of the altered interfacial properties with the surrounding dielectric medium. These results were further confirmed by XAFS of partially and fully etch films. XAFS results revealed the nature of the etch modification region resulting from fluorocarbon and chlorine etch chemistries, to consist of significant

amorphous  $GeO_2$  and  $Sb_2O_3$ . The volatility of the chlorine etch chemistry is highlighted, since all the Sb was removed from this sample.

## WORKS CITED

- [1] **S.-H. Lo, D. A. Buchanan, Y. Taur, and W. Wang.**, 5, IEEE Int. Elec. Lett, 1997, Vol. 18, pp. 209-211.
- [2] **S. Raoux, G. W. Burr, M. J. Breitwisch, C. T. Rettner, Y.-C. Chen, et al** IBM J. Res. & Dev 2008, Vol. 52, pp. 4-5.
- [3] **Y. C. Chen, C. T. Rettner, S. Raoux, G. W. Burr, S. H. Chen, R. M. Shelby, M. Salinga, et al.** San Francisco, CA, : International Electron Devices Meeting, Dec. 2006, pp. 777-780.
- [4] **S-M. Yoon et al.** 27, Jpn. J. Appl. Phys 2005, Vol. 44, pp. L 869-L 872.
- [5] **E. A. Joseph, T. D. Happ, S.-H. Chen, S. Raoux, et al** Symp. VLSI-Technology Systems and Applications, 2008. pp. 142-143.
- [6] **G.B. Stephenson** Nucl. Instr. Meth. Phys. Res. A , 1988, Vol. 266, p. 447.
- [7] **G.B. Stephenson, K.F. Ludwig, Jr J.L. Jordan-Sweet, S. Brauer, et al** Rev. Sci. Instrum 1989, Vol. 60, p. 1537.
- [8] **L.A. Clevenger, R.A. Roy, C. Cabral, Jr K.L. Saenger, et al** J. Mater. Res 1995, Vol. 10, p. 2355.
- [9] **C. Lavoie, C. Cabral, Jr L.A. Clevenger, J.M.E. Harper, et al** Mater. Res. Soc. Symp. Proc 1996, Vol. 406, p. 163.
- [10] **B. Ravel.** Community/X23A2-xafs.org. *xafs.org*. [Online] 11 12, 2009. [Cited: 11 17, 2009.] <http://xafs.org/Community/X23A2>.
- [11] *X-ray Absorption Fine Structure—XAFS13.* **S. Kelly and B. Ravel.** [ed.] B. Hedman and P. Pianetta Amer. Inst. of Phys. CP882.
- [12] **B. Ravel and M. Newville** J. Synchrotron Radiat 2005, Vol. 12, pp. 537-541.
- [13] **M. Newville** J. Synchrotron Rad 2001, Vol. 8, p. 322.
- [14] **S. I. Zabinsky, J. J. Rehr, A. Ankudinov, R. C. Albers, and M. J. Eller,** Phys. Rev. B, 1995, Vol. 52, p. 2995.
- [15] **R.M. Shelby, S. Raoux,** J. Appl. Phys 2009, Vol. 105, p. 104902.

- [16] **L. Pauling** J. Am. Chem. Soc 1932, Vol. 54, p. 3570.
- [17] **M. Avrami** J. Chem. Phys 1941, Vol. 9, p. 177.
- [18] **V. Weidenhof, I. Friedrich, S. Ziegler, and M. Wuttig,** 6, J. Appl. Phys , 2001, Vol. 89, pp. 3168-3176.
- [19] **S. Senkader and C.D. Wright.** 2, J. Appl. Phys 2004, Vol. 95, p. 504.
- [20] **N. Ohshima** J. Appl. Phys 1996, Vol. 79, p. 8357.
- [21] **K. Prabhakaran, T. Ogino, F. Maeda, and Y. Watanabe,** 16, Appl. Phys. Lett 2000, Vol. 76, p. 2244.
- [22] **D. Schmeisser, R.D. Schnell, A. Bogen, F.J. Himpsel, D. Rieger, G. Landgren, and J.F. Morar,** Surf. Sci 1986, Vol. 172, p. 455.
- [23] **J.S. Washington et al** Mater. Res. Soc. Symp 2009, Vol. 1160, pp. H13-08.
- [24] **O. Majerus, L. Cormier, D.R. Neuville, L. Galois, G. Calas,** J. of Non-Crys. Sol 2008, Vol. 354, pp. 2004-2009.
- [25] **R. B. Gregor, F.W. Lytle, J. Kortright, A. Fischer-Colbrrie,** J. Non. Crys. Solids, 1987, Vol. 89, pp. 311-325.
- [26] **A.C. Scheinost, A. Rossberg, D. Vantelon, I. Xifra, et al** Geochimica et Cosmochimica Acta, 2006, Vol. 70, pp. 3299–3312.

## **Appendix 4: (JNCS Submitted) Analysis of the forgotten parts of the Ge K edge spectra: life beyond the EXAFS oscillations!**

**Gerald Lucovsky<sup>1\*</sup>, J. S. Washington<sup>1</sup>, L. Miotti<sup>1</sup>, M.A. Paesler<sup>1</sup>**

<sup>1</sup> Department of Physics, NC State University, Campus Box 8202, 27695-8202 Raleigh, NC, USA

\* Corresponding author: e-mail [lucovsky@ncsu.edu](mailto:lucovsky@ncsu.edu), Phone: +01 919 515 3938, Fax: +01 919 515 653

Received ZZZ, revised ZZZ, accepted ZZZ

Published online ZZZ (Dates will be provided by the publisher.)

PACS 61.05.CM, 61.05.jp, 61.43.Dq, 64.75.Lm

### **Abstract**

The white line and X-ray absorption near edge spectroscopy (XANES) spectral regions of the Ge K edge, ~11100 to 11112 eV, and between 11112 and 11180 eV, respectively, contain electronic structure information that complements near-neighbor bonding information in the single-scattering EXAFS regime. The multiple-scattering XANES features are not generally addressed in EXAFS studies that are targeted to obtain bonding information. There are systematic changes in the X-ray photon energy of the spectral peak of the white line for Ge-Sb-Te (GST) alloys, GeSb and GeTe model compounds, and other Ge alloys that scale directly with average bond ionicity. The spectral widths of these features correspond to electronic transitions important in optical memory devices. There are other features in the XANES region associated with shake-off effects for shallow atomic core states that reveal bonding information important in analysis of the oscillatory features in the EXAFS regime. These include bonding pairs that are addressed in the fit procedures; e.g. Ge-Te and Ge-Sb in GST 225.

### **1 Introduction**

The research presented in the article was motivated by studies of O K edge X-ray absorption spectra for transition metal oxides [1]. These studies have been extended to the pre-edge shake-up, and post-edge shake-off continuum regimes of XAS spectra of HfO<sub>2</sub> and TiO<sub>2</sub>, yielding important information for local bonding arrangements at O-atom vacancies [1]. The pre-edge region for the Ge K edge for GST alloys is less than ~11110 eV, and the post-edge XANES region extends from within the continuum edge above of the Ge-atomic ionization potential (IP) of 11103 eV to approximately 11200 eV, overlapping the EXAFS spectral regime that starts at ~ 11150 eV [2,3,4]. The GST 225 alloy XANES regime contains

two broad features at about 11130 eV and 11160 eV. This article will utilize the entire spectral XANES regime as defined above, but will emphasize differences in the 11130 eV and 11160 eV regime that are different for Ge-Te and Ge-Sb nearest neighbor (N-N) pairs. The observation of the 11130 and 11160 eV broad features, and their dependence in GST alloy compositions, 224, 225, 226 and 227, has raised issues relative to their atomic origin, and in particular motivated one of the authors (JPW) to re-examine assumptions made in analyzing the EXAFS data, as discussed in previous papers [5,6]. These papers considered Ge-Te and Sb-Te bonds, but did not consider Ge-Sb bonds, and therefore were not consistent with the composition dependence of XANES features.

## 2 EXAFS Results for GST 225 Revisited

The EXAFS results of our NC State group reported in Ref. 5 for non-crystalline GST-225 excluded the possibility of Ge-Sb bonds. This exclusion was based on the seminal EXAFS studies of Kolobov and co-workers which made no mention of Ge-Sb bonding in the GST 225 composition, either in the non-crystalline phase, or the metastable face-centered-cubic (FCC) phase [6]. Preliminary results by one of the authors of this paper (JWP), as yet unpublished [7], have indicated additional features in the Ge EXAFS spectrum corresponding to Ge-Sb bonds as well as a complimentary Ge-Sb feature in the Sb spectrum. The Ge-Sb features in the Ge and Sb EXAFS of GST 225 are found in GST 224, but not in GST 226 or GST 227. Comparisons between GST 225 and 227, and GST 224 and 226 will be included in this paper.

Prior to a paper published by the NC State group (here-after D. Baker, J.P. Washington, G. Lucovsky, and M.A. Paesler) [8], it had been assumed that the GST 225, and other GST compositions resided on tie-lines between the edges of a ternary diagram with corners defining a base between Te and Ge, and an apex at Sb [9]. All of the GST composition studied by the NC State group, were on a pseudo-binary tie-line from Te to GeSb, whilst there were two possible tie lines for GST 225: (i) GeTe to Sb<sub>2</sub>Te<sub>3</sub>, as suggested by Kolobov et al, and Yamada et al. in Refs. 7 and 9, respectively and (ii) from GeTe<sub>2</sub> to Sb<sub>2</sub>Te as indicated in Ref. 8, and consistent with Ge-Sb bonds.

The remainder of this article address features in core level shake-off XANES region of the Ge K edge spectrum between 11115 eV and 11170 eV, partially overlapping the EXAFS regime as indicated in Fig. 1.

## 3. The White Line Spectral Peak

The spectra in Fig. 1 are for non-crystalline 225 GST and the fcc phase of 225 GST. The spectral peaks in white line regime are at the same X-ray photon energies, ~11105 eV, while there are small, but systematic and significant differences in the spectral peaks of the two broad features in the XANES regime that are addressed in Sections 4 and 5. The white line regime spectral peaks for the GST films of this paper, GST 224, 225, 226 and 227, are at approximately the same X-ray energies to within  $\pm 0.3$  eV. However, in films

that have a higher average Pauling electro-negativity as for example  $\text{GeO}_2$  and  $\text{GeSe}_2$  this feature is shifted to higher energy, with linear eV shift proportional to the bond ionicity. Since the electronegativity differences between Ge, Se and Te are small, 0.1, the shifts of this peak for GST 225, and the closely related alloys Ge-Te and Ge-Sb are too small to discriminate between different nearest neighbors bonding arrangements such as Ge-Sb and Ge-Te.

#### 4 The XANES Regime I: Model Systems

The XANES regime associated with an atomic K edge begins at the ionization potential (IP) and typically extends at least 50 eV further into continuum regime [2,3]. The IP is approximately equal to the 1s core level of the atom, and but can be different in molecule or solid. X-ray excitations are typically multi-electron processes, and as such require a many-electron approach for calculation of excitation energy products [2,3,4]. When the X-ray energy is below the IP, these multi-electron processes are called a “shake-up” effect; when the X-ray energy exceeds the IP, “shake-off” effects are possible when the excess kinetic of the photo-emitted electron exceeds the binding energy of shallow core states. For example if the atom in question is Ge, as in GST alloys, the X-ray excitation is the Ge K edge process and these shallow core states are associated with the Ge atom, or one its nearest neighbors, in this case either Sb or Te [7]. As noted above, an understanding the process, and a study of the XANES spectral features would have indicated a problem in the limited EXAFS analysis of Ref. 6, and would have alerted our group at NC State to a possible issue in these previously reported studies. It is demonstrated that combining the Ge XANES edge spectra of 225 GST, with other GST alloys and model compounds with Ge-Te and Ge-Sb bonds has provided a way to discriminate between shake-off XANES features associated with Ge, Sb or Te core levels. The relevant core levels states considered in this analysis extend to about 50 eV and presented in Table. 1. Figures 2, 3 and 4 address the model compounds, and demonstrate spectral differences between Ge-Te and Ge-Sb features that will be applied to bonding arrangement differences in GST alloys, and between crystalline and non-crystalline GST 225.

**TAB 1** Shallow atomic core levels for Ge, Sb and Te\*

Ge state	eV	Sb state	eV	Te state	eV
$3d_{5/2}$	29.2	5s	16.0	5s	19.1
$3d_{3/2}$	29.8	$4d_{5/2}$	32.1	$4d_{5/2}$	40.4
--	--	$4d_{3/2}$	33.3	$4d_{3/2}$	41.9

\*these states are responsible for shake-off effects in the Ge K edge Xanes spectral regime

Figure 2 compares the XANES features for non-crystalline Ge and nano-crystalline GeTe between 20 and 70 eV above the Ge IP. The Ge film displays one feature assigned to the two Ge 3d spin-orbit split components. The GeTe displays two features, one assigned to the Te 5s core state, and the second to the two Te 4d spin-orbit split components. The Ge 3d state feature is not evident in the GeTe spectra and assumed to be *mixed with* with the broad low energy edge of the Te 4d feature.

Figure 3 compares Ge K edge XAS spectra for two Ge-Sb alloy samples, Ge<sub>50</sub>Te<sub>50</sub> and Ge<sub>15</sub>Sb<sub>85</sub>. Two features associated respectively with the Sb 5s core level at ~27 eV, and Sb 4d spin-orbit doublet at ~60 eV are evident. Their relative intensities scale with the Sb content in these two alloys, and there is a small energy difference between the spectral peaks of the Sb 4d features. This feature is about 0.5 eV higher in energy in the Ge<sub>15</sub>Sb<sub>85</sub> alloy film.

Figure 4 is a plot of the atomic core level energy in eV as a function of a normalized X-ray photon energy,  $(E-E_{IP}(Ge))$  in eV. The data for Ge and GeTe thin films, and the Ge-Sb alloys are linear, but different. Two parameters are extracted from each of these linear fits. The slope of these plots is the ratio of the kinetic energy of the photo-electron that is responsible for the shake-off process to the core state binding energy. This ratio is about 1.5-2.5 times the atomic core level binding energy for semiconductors [10], and is expected to be in the same range for the shake-off processes that give rise to features in the XANES energy regime [2,3,4]. This is indeed the case for the two plots in Fig. 4, where the slopes are ~1.5 and 1.8 eV, respectively for Te and Ge, and Sb core states. Equally important is the energy of the Ge 1s core level state; i.e the IP. This is given by the y-axis intercept. These extrapolations that yield values approximately equal to the Ge IP value of 11103 eV. This analysis validates the interpretation of the spectral peaks within the IP regime. This is supported by the results, not shown in this article, that include multi-core level excitations for 2 Ge and Ge+Te states, as well as the single core level excitations of Fig. 2 for Ge, and Te. When these data are displayed in a plot similar to that in Fig. 4, the slope is 1.4 and the intercept 11100 eV. Each of these is within experimental error for the corresponding plot analysis for the single core state shake-off XANES features in Fig. 4

## 5 The XANES Regime II: GST Alloys

The spectral signatures identified in Figs. 2, 3 and 4, for Sb and Te bonding to Ge are used as a basis for comparisons between a pair of GST alloys in Fig. 5, GST 225 and GST 227, and Fig. 6, GST 224 and GST 226. As yet unpublished EXAFS results in Ref. 5 have established that GST 224 and GST 225 alloys have Ge-Te, Ge-Sb and Sb-Te bonds, where as GST 226 and GST 227 alloys have Ge-Te and Sb-Te bonds, but no detectable Ge-Sb bonding.

The spectra in Figs. 5 and 6, each indicate features in two spectral regimes: ~27 for Sb and Te 5s shake-off, and ~60-63 eV for Sb and Te 4d shake-off. As demonstrated in Figs. 2 and 3, the 5s shake-off features for Sb and Te occur at approximately the same X-ray photon energies, and as such do not discriminate between Ge-Sb and Ge-Te bonding, while the peaks associated with Ge-Sb and Ge-Te 4d shake-off occur at different energies. Based

on this observation and Figs. 5 and 6, there are Ge-Sb bonds in the GST 224 and GST 225 compositions, but not in the GST 226 and GST 227. This has been addressed in more detail in Ref. 7 for EXAFS. The GST 224 and 225 compositions are deficient in Te; i.e there is insufficient Te to satisfy the bonding requirements of covalent Ge and Sb without Ge-Sb bonds. In contrast, the GST 224 and 225 compositions have sufficient Te to satisfy covalent bonding. The respective compositions are on the  $\text{Ge}_2\text{Te}_3$ - $\text{Sb}_2\text{Te}_3$ , and  $\text{GeTe}_2$ - $\text{Ge}_2\text{Te}_3$  tie-lines. This bonding model is further supported by the plots in Fig. 7

Figure 7 compares Ge K edge spectra in the XANES spectral regime between 52 and 67 eV. The model system Ge-Te and Ge-Sb alloys display features at 61 eV and 57.5 eV respectively. The GST 227 feature is at 60.5 eV, and very close to the Ge-Te model system. In contrast, the GST 225 feature is at 59 eV, and is indicative of contributions from both Ge-Sb and Ge-Te bonds. Similar behaviors prevail for the respective GST 226 and GST 224 alloys. Finally a comparison of the 60 eV features for GST 225 as-deposited non-crystalline films, and annealed crystalline films indicate mixed Ge-Te/Ge-Sb bonding in the as-deposited film, but is consistent with the bonding in meta-stable FCC phase with only Ge-Te bonding indicated in the annealed crystallized film.

## 6. Summary

The white line and X-ray absorption near edge spectroscopy (XANES) spectral regions of the Ge K edge, ~11100 to 11150 eV, and between 11115 and ~11200 eV, respectively contain electronic structure information that complements the near-neighbor bonding information in the EXAFS regime. The position of the spectral peak of the Ge K edge scales with the average electronegativity, and shows no detectable differences for the GST alloys and model Ge-Te and Ge-Sb materials since the electronegativity differences are small, < 0.1. The features in the XANES regime, on the other hand distinguish between Ge-Te and Ge-Sb bonding, and can be used to identify the bonding arrangements relevant to the analysis of the features within the EXAFS spectral regime.

## References

- [1] G. Lucovsky et al *Microelectronic Eng.* 86, 1654 (2009).
- [2] A. Bianconi, XANES Spectroscopy, in *X-ray Absorption*, ed. by D.C. Koningsberger and R. Prins (Wiley Interscience, New York, 1988) Chapter 5.
- [3] B.K. Teo, *EXAFS: Basic Principles and Data Analysis* (Springer-Verlag, Berlin, 1986), Chapter 5.
- [4] J. Stöhr, *NEXAS Spectroscopy* (Springer, Berlin, 1992), Chapters 2 and 4.
- [5] M.A. Paesler, et al, *J. Non-Cryst. Solids* 354, 2706 (2008).
- [6] A.V. Kolobov, et al *Nature Materials* 3, 703 (2004).
- [7] J.P Washington, et al unpublished.
- [8] G. Lucovsky, et al *Phys. Stat. Solidi A* 206, 1610 (2009).
- [9] N. Yamada, et al *J. Appl. Phys.* 69, 2849 (1991).
- [10] E.O. Kane, *Phys. Rev.* 139, 159 (1967).

## Figure Captions

Figure 1. Ge K edge XAS spectra for crystallized fcc GST 225 and non-crystalline as-deposited GST 225. The white line and XANES spectral regimes are indicated, as is the onset of the EXAFS regime.

Figure 2. Ge K edge XAS spectra for Ge and GeTe.

Figure 3. Ge K edge XAS spectra for two Ge-Sb alloy compositions.

Figure 4. Atomic X-ray photon energy as a function of the atomic core state energy.

Figure 5. Ge K edge XAS spectra for as-deposited GST 225 and 227 alloys.

Figure 6. Ge K edge XAS spectra for as-deposited GST 224 and 226 alloys.

Figure 7. Comparison of XANES features at ~60 eV for Ge-Te and Ge-Sb model systems, and GST 225 and GST 227.

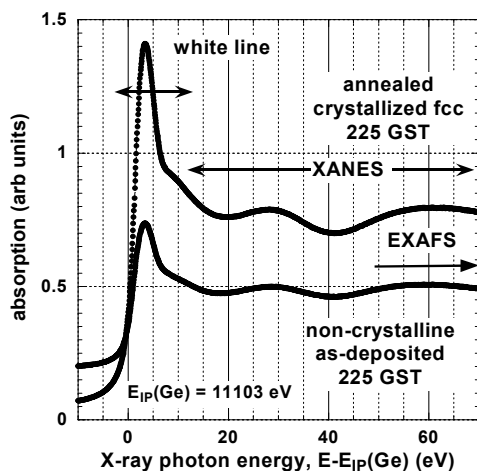


Figure 1

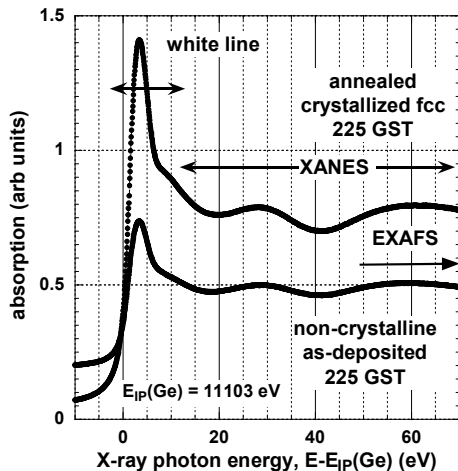


Figure 2

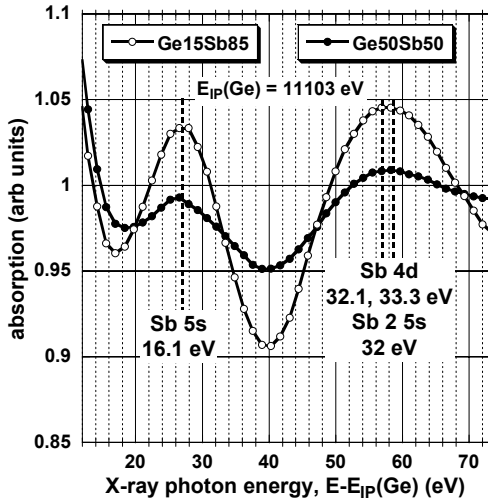


Figure 3

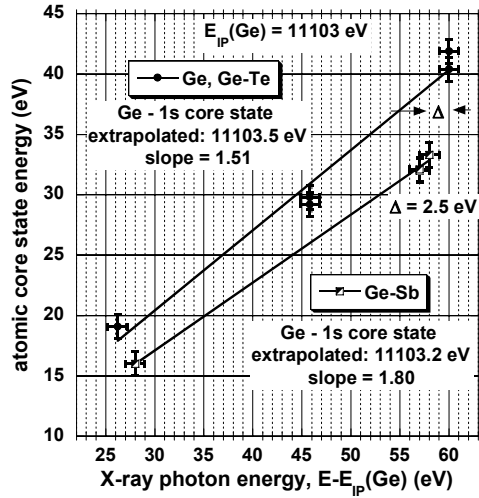


Figure 4

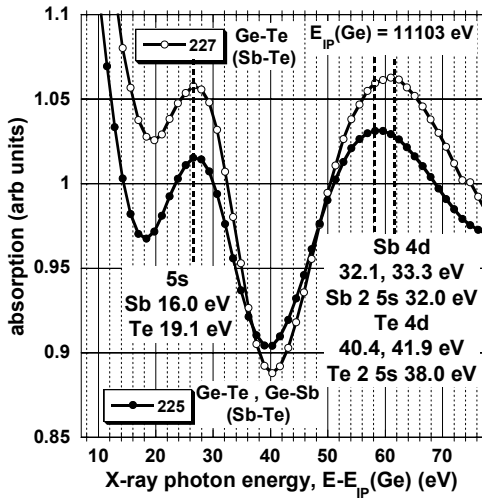


Figure 5

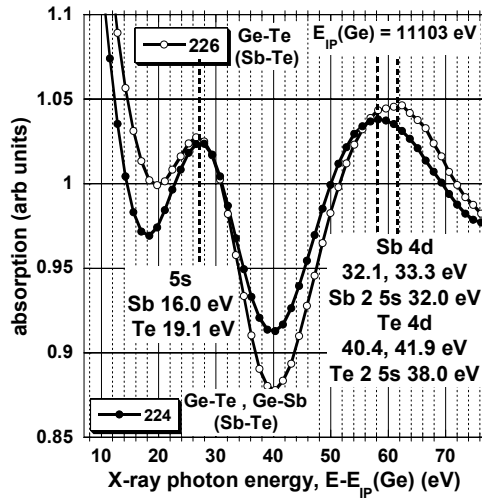


Figure 6

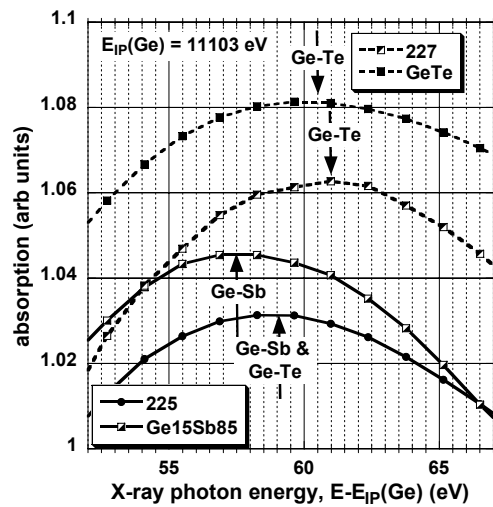


Figure 7

## Appendix 5: Ge and Sb K edge EXAFS Fit Results calculated for the 400°C annealed $\text{Ge}_x\text{Sb}_{(1-x)}$ samples.

TABLE1: A summary of the fitting parameters calculated from the fits to the 400°C annealed  $\text{Ge}_x\text{Sb}_{(1-x)}$  samples and their percent errors (note  $\text{Ge}_{15}\text{Sb}_{85} = '15:85'$ ). Each alloy shows both the parameters from the Ge edge as well as the Sb edge.  $S_0^2$  was 0.9 for all Ge edge data and 0.9 for all Sb edge data. Sb edge data was not shown for x-75:25 since the poor data quality prevented analysis.

Alloy	Bond	N	$\sigma^2(\text{\AA}^2)$	E(eV)	R (Å)
x-75:25	Ge-Ge paths	3.80 +/- 0.57	0.004 +/- 0.0003	6.02 +/- 0.6	2.47 +/- 0.02
		12.00 +/- 1.8	0.014 +/- 0.001		4.04 +/- 0.04
		24.00 +/- 3.6	0.004 +/- 0.002		4.51 +/- 0.04
		12.00 +/- 1.8	0.030 +/- 0.004		4.72 +/- 0.04
	Ge-Sb	0.20 +/- 0.03	0.003 +/- 0.003		2.69 +/- 0.02
x- 50:50	Ge-Ge paths	3.84 +/- 0.57	0.004 +/- 0.0003	6.57 +/- 0.6	2.47 +/- 0.02
		12.00 +/- 1.8	0.011 +/- 0.001		4.03 +/- 0.04
		24.00 +/- 3.6	0.004 +/- 0.002		4.48 +/- 0.04
		12.00 +/- 1.8	0.020 +/- 0.004		4.74 +/- 0.05
	Ge-Sb	0.16 +/- 0.03	0.003 +/- 0.003		2.69 +/- 0.02
	Sb	3.00 +/- 0.5	0.003 +/- 0.001	4.43 +/- 1.08	2.91 +/- 0.02
		3.00 +/- 0.5	0.010 +/- 0.003		3.39 +/- 0.03
		6.00 +/- 1	0.010 +/- 0.002		4.29 +/- 0.04
		6.00 +/- 1	0.020 +/- 0.01		4.51 +/- 0.05
	x-25:75	Ge-Ge paths	3.72 +/- 0.57	0.004 +/- 0.0003	5.40 +/- 0.53
12.00 +/- 1.8			0.011 +/- 0.001	4.01 +/- 0.04	
24.00 +/- 3.6			0.004 +/- 0.002	4.45 +/- 0.04	
12.00 +/- 1.8			0.020 +/- 0.004	4.72 +/- 0.05	
Ge-Sb		0.28 +/- 0.03	0.001 +/- 0.002	2.74 +/- 0.02	
Sb		3.00 +/- 0.5	0.005 +/- 0.001	7.10 +/- 1.6	2.92 +/- 0.02
		3.00 +/- 0.5	0.030 +/- 0.01		3.35 +/- 0.03
		6.00 +/- 1	0.010 +/- 0.004		4.32 +/- 0.04
		6.00 +/- 1	0.008 +/- 0.002		4.54 +/- 0.05
x-15:85		Ge-Ge paths	3.60 +/- 0.5	0.004 +/- 0.0003	5.12 +/- 0.5
	12.00 +/- 1.8		0.010 +/- 0.002	4.03 +/- 0.04	
	24.00 +/- 3.6		0.005 +/- 0.002	4.53 +/- 0.04	
	12.00 +/- 1.8		0.020 +/- 0.004	4.70 +/- 0.05	
	Ge-Sb	0.40 +/- 0.04	0.005 +/- 0.003	2.74 +/- 0.02	
	Sb	3.00 +/- 0.5	0.007 +/- 0.001	4.18 +/- 1.5	2.91 +/- 0.02
		3.00 +/- 0.5	0.020 +/- 0.008		3.35 +/- 0.03
		6.00 +/- 1	0.020 +/- 0.005		4.28 +/- 0.04
		6.00 +/- 1	0.030 +/- 0.02		4.52 +/- 0.05
	x-7:93	Ge-Ge paths	2.56 +/- 0.3	0.004 +/- 0.0003	6.62 +/- 0.6
12.00 +/- 1.8			0.010 +/- 0.002	4.04 +/- 0.04	
24.00 +/- 3.6			0.010 +/- 0.002	4.55 +/- 0.04	
12.00 +/- 1.8			0.020 +/- 0.004	4.69 +/- 0.05	
Ge-Sb		1.34 +/- 0.13	0.004 +/- 0.003	2.76 +/- 0.03	
Sb		3.00 +/- 0.5	0.006 +/- 0.001	5.32 +/- 1.2	2.92 +/- 0.02
		3.00 +/- 0.5	0.020 +/- 0.004		3.35 +/- 0.03
		6.00 +/- 1	0.010 +/- 0.003		4.27 +/- 0.04
		6.00 +/- 1	0.020 +/- 0.005		4.48 +/- 0.05

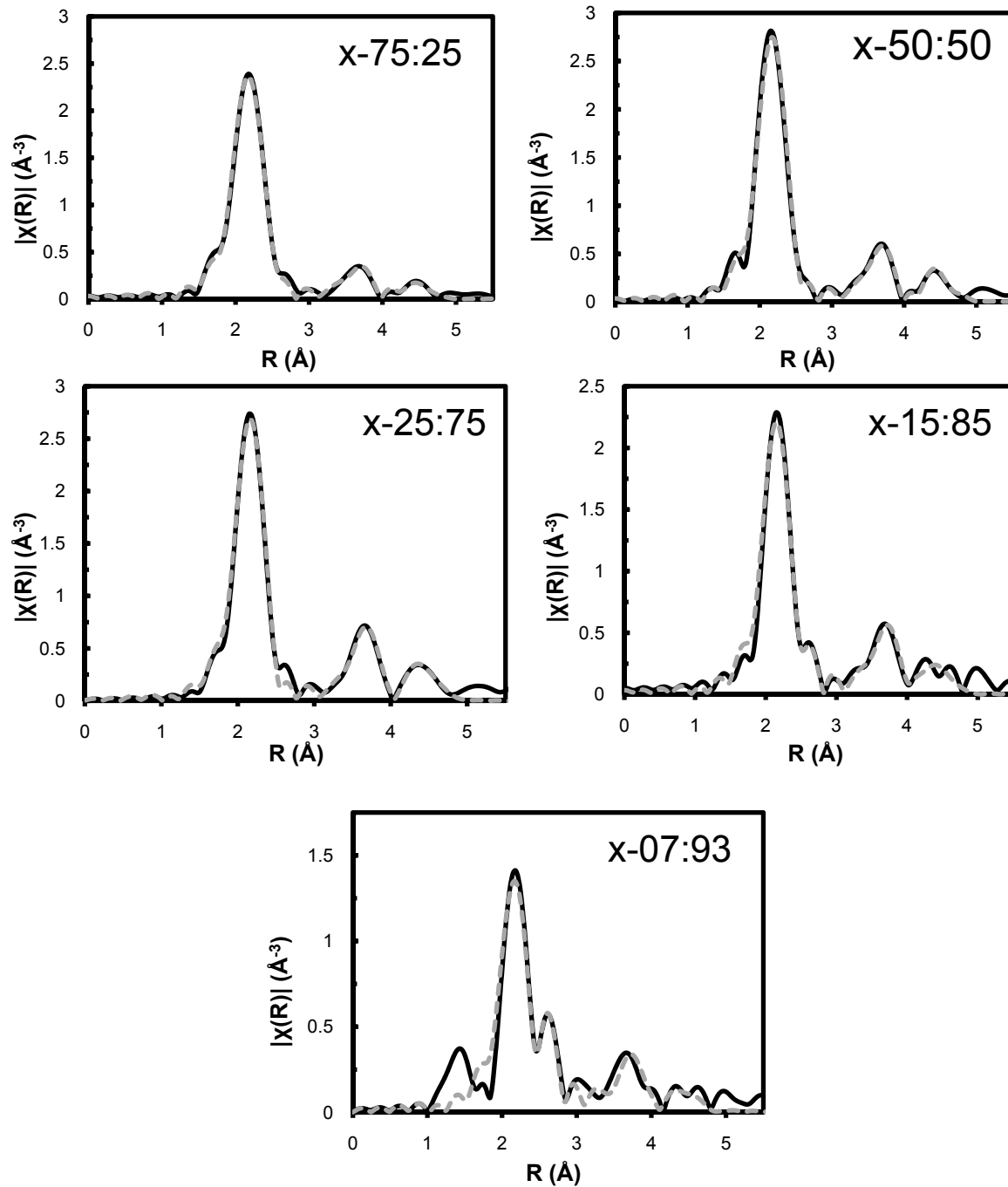


FIG1: Fits to the Ge K edge for 400C annealed  $\text{Ge}_x\text{Sb}_{(1-x)}$  films. Magnitude of the complex Fourier transformed of EXAFS spectra is shown. Solid black line = data, gray dashed line = fit. These fits are representative of the typically good fit to data obtained in all annealed  $\text{Ge}_x\text{Sb}_{(1-x)}$  Sb edge data. Fitting range,  $\Delta R = 1.6 - 5 \text{ \AA}$  excludes the surface oxide / background feature in 07:93

In figure 1, the fitting range for all samples at the Ge edge was  $\Delta R=1.6 - 5\text{\AA}$ . This encompassed the 1<sup>st</sup>, 2<sup>nd</sup>, and 3<sup>rd</sup> shell scattering paths for crystalline Ge, while excluding the low R feature in 07:93. We expect this is low R feature to be surface Ge-O, however no effort was made to characterize this. In all samples, we were able to fit a fraction of amorphous, 4 fold, tetrahedral, Ge-Sb bonds. The 1<sup>st</sup> shell therefore consisted of Ge-Ge bonds from crystalline Ge, and some amount of Ge-Sb, whose fraction increased with composition as approximately 5%, 6%, 7%, 10%, and 33% of the nearest neighbor Ge bonds for 75:25, 50:50, 25:75, 15:85, and 07:93. The bond distance of these Ge-Sb bonds, seemed to increase (from the expected value of  $\sim 2.70\text{\AA}$ ) as the size and volume fraction of the Ge crystallites decreased with respect to the crystalline Sb bulk: R was 2.74 and 2.76 $\text{\AA}$  for 15:85 and 07:93 respectively. It is therefore likely that these bonds are strained, interfacial Ge-Sb bonds on the grain boundary between Ge and Sb crystal in the system. At the Sb edge, we were not able to fit these Ge-Sb bonds, due to comparably high signal to noise in the Sb edge data.

## Appendix 6: The Optical Dielectric Function for as-deposited N-GST alloys

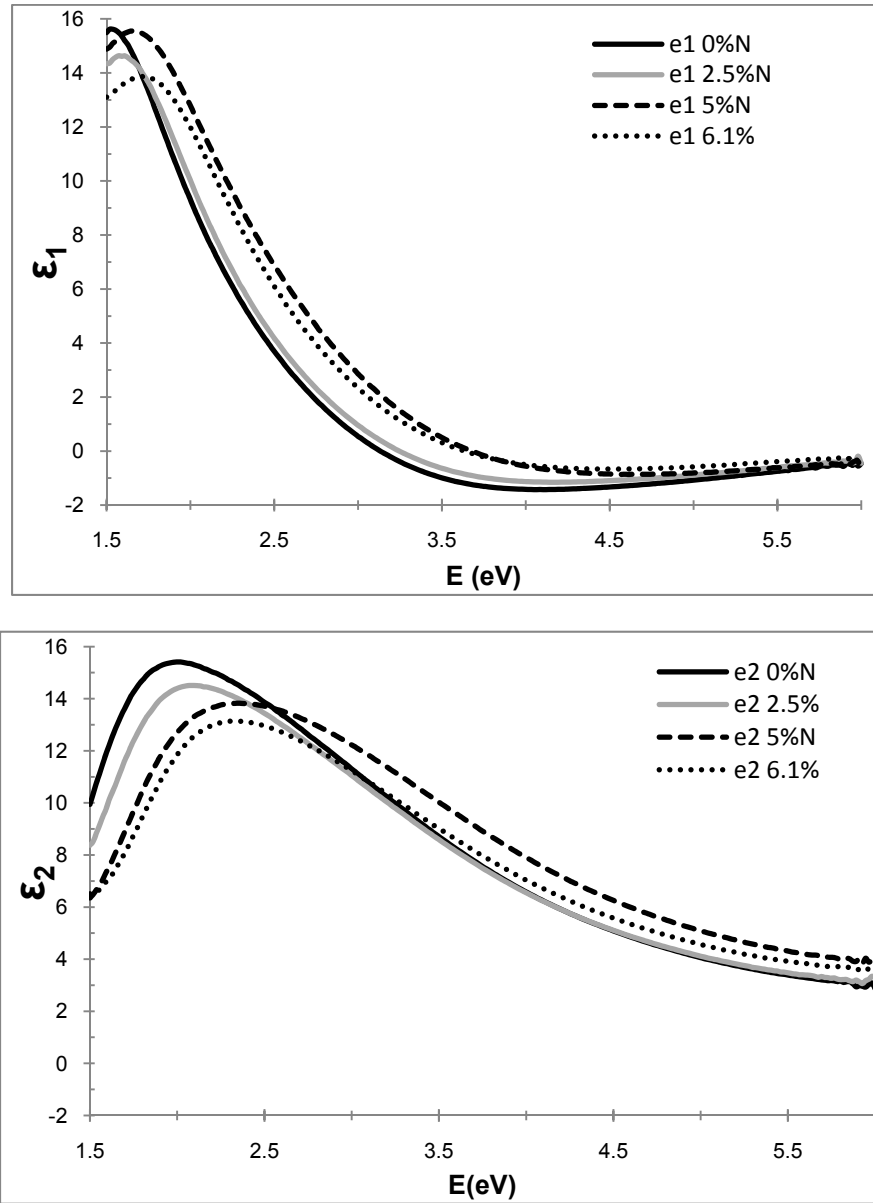


FIG 1: The real part  $\epsilon_1$  and imaginary part  $\epsilon_2$  of the dielectric function versus energy  $E$  for as-deposited N-GST samples obtained using the effective medium approximation.

We measured spectroscopic ellipsometry (SE) data for ~100nm thick samples of 0.0%, 2.5%, 5%, and 6%N-GST, dc sputter deposited on bare Si wafers (similar to samples measured by EXAFS in section 2.5). All samples were dipped in HF for 10-20 seconds and subsequently measured in a N ambient. SE measurements were taken from 1.5 to 6 eV in 0.01 eV increments using a variable angle automatic spectroscopic rotating analyzer [1] ellipsometer. The angle of incidence was set to 67.08° and polarizer angle was 30°.

The dependence of the optical dielectric function in figure 1, on N concentration, is consistent with a tetrahedron model in which the Ge tetrahedral are considered to be the fundamental structural units. This approach was first introduced by Phillips [2] and later developed by Aspnes and Theeten [3], who combined it with the Bruggemann effective-medium approximation [4]. A very similar optical response was observed in the  $\epsilon$  of hydrogenated amorphous silicon nitride alloys, a-Si<sub>x</sub>N<sub>(1-x)</sub> [5]. This confirms our EXAFS, FTIR, and XPS findings which indicate that nitrogen preferentially bonds to Ge in N-GST forming a local, chemically ordered germanium nitride.

### References for Appendix 6

- 1) D. E. Aspnes, “Fourier transform detection system for rotating-analyzer ellipsometers,” *Opt. Commun.* **8**, 222–225 (1973).
- 2) H. R. Phillips, *J. Electrochem. Soc.* **120**, 295 (1973).
- 3) D.E. Aspnes and J.B. Theeten, *J. Appl. Phys.* **50**, 4928 (1979).
- 4) D.A.G. Bruggemann, *Ann. Phys. (Leipzig) [Folge 5]* **24**, 636 (1935).
- 5) Z. Yin and F.W. Smith, *Phys. Rev. B* **42**, 6, 3658-3665 (1990).